QUANTIFICATION OF UNCERTAINTY IN THE MODELING OF CREEP IN

RF MEMS DEVICES

A Dissertation

Submitted to the Faculty

of

Purdue University

by

Peter A. Kolis

In Partial Fulfillment of the

Requirements for the Degree

of

Doctor of Philosophy

Aug 2020

Purdue University

West Lafayette, Indiana

# THE PURDUE UNIVERSITY GRADUATE SCHOOL
# STATEMENT OF DISSERTATION APPROVAL

Dr. Marisol Koslowski, Co-Chair

     School of Mechanical Engineering

Dr. Anil Bajaj, Co-Chair

     School of Mechanical Engineering

Dr. Ilias Bilionis

     School of Mechanical Engineering

Dr. Dimitrios Peroulis

     School of Electrical and Computer Engineering

**Approved by:**

     Dr. Nicole Key

          Head of the School Graduate Program

# ACKNOWLEDGMENTS

TABLE OF CONTENTS

## LIST OF TABLES

LIST OF FIGURES

## ABSTRACT

Kolis, Peter A. PhD, Purdue University, Aug 2020. Quantification of Uncertainty in the Modeling of Creep in RF MEMS Devices. Major Professors: Marisol Koslowski and Anil Bajaj, School of Mechanical Engineering.

Permanent deformation in the form of creep is added to a one-dimensional model of a radio-frequency micro-electro-mechanical system (RF-MEMS). Due to uncertainty in the material property values, calibration under uncertainty is carried out through comparison to experiments in order to determine appropriate boundary conditions and material property values. Further uncertainty in the input parameters, in the form of probability distribution functions of geometric device properties, is included in simulations and propagated to the device performance as a function of time. The effect of realistic power-law grain size distributions on the creep response of thin RF-MEMS films is examined through the use of a finite volume software suite designed for the computational modelling of MEMS. It is seen that the use of a realistic height-dependent power-law distribution of grain sizes in the film in place of a uniform grain size has the effect of increasing the simulated creep rate and the uncertainty in its value. The effect is seen to be the result of the difference between the model with a homogeneous grain size and the model with a non-homogeneous grain size. Realistic variations in the grain size distribution for a given film are seen to have a smaller effect. Finally, in order to incorporate variations in thickness in manufactured devices, variation in the thickness of the membrane across the length and width is considered in a 3D finite element model, and variation of thickness along the length is added to the earlier one-dimensional RF-MEMS model. Estimated uncertainty in the film profile is propagated to selected device performance metrics. The effect of film thickness variation along the length of the film is seen to be greater than the effect of variation across the width.

# 1. INTRODUCTION

In this chapter the question of material modeling of thin films used for MEMS devices is introduced, with a focus first on thin films themselves, and then on RF-MEMS structures that are fabricated utilizing the thin films. Thin films can be modeled through classical continuum models, but modern fabrication techniques necessarily introduce various issues that make the assumption of a uniform elastic continuum invalid. Various models of thin films introduce microstructural issues that are related to nonuniformity in thin films, including models which represent nonuniformity in the material's microstructure; models considering uniform or nonuniform crystalline grain structures; and the models of various microstructure properties that result in creep and energy loss in the material during the course of deformation. In addition to properties of thin films, modeling issues arise that result from actual physical structural configurations of the MEMS devices in the form of beams with various support mechanisms, plates with various geometries and supports, and actuation and sensing mechanisms.

## 1.1 Thin Films in RF-MEMS Switches

Thin films with dimensions on the order of 1 $\mu$m in the smallest direction which contain nanocrystalline grains are used in a variety of microelectromechanical systems (MEMS). These thin films exhibit a higher yield stress than coarse-grained bulk material due to Hall-Petch strengthening, which predicts an inverse relationship between the grain size and yield stress [1]. Below a critical submicron grain size, however, yield stresses have been seen to deviate from the Hall-Petch relationship and remain constant or decline with decreasing grain size. This has been termed the 'inverse

Hall-Petch relation' and has been noted in, for example, [2], [3], [4], [5], [6], [7], with various underlying mechanisms proposed.

The small grain size of thin films has the additional effect of increasing diffusional creep, a deformation mechanism in which point defects move through grain interiors (Nabarro-Herring creep) or around grain boundaries (Coble creep) [8]. Plastic strain rates in Nabarro-Herring and Coble creep are proportional to $\frac{1}{d^2}$ and $\frac{1}{d^3}$ respectively, where $d$ is the average grain size. Coble creep, in particular, is driven by the diffusion of vacancies. At lower stresses and temperatures, Coble creep is the dominant deformation mechanism.

Creep is defined as deformation under a constant applied load; stress relaxation is the identical phenomenon for a constant applied deformation. Creep is time-dependent and results in permanent deformation, which may degrade expected performance and/or cause device failure. Creep generally occurs in three stages. In the first and third stages, deformation is large and rapid. In the second stage, which occurs over the greatest period of time and which is the only stage considered here, the strain caused by creep is nearly a linear function of time. An example of this behavior seen in [9] is reprinted with permission in Figure 1.1, in which permanent deformation attributed to creep causes a loaded thin film to permanently deform over the course of more than 100 hours. Similar behavior is seen in [10], and device profiles are recorded before and after the creep behavior, with some apparent recovery after further relaxation while unloaded.

The mechanical properties of thin films as used in MEMS are being extensively studied. Reviews of various experimental methods for the determination of mechanical properties are presented in [11], [12]. New characterization methods are being defined, as in [13], which utilizes digital image correlation to determine strain fields which result from tensile tests of dogbone specimens. Much literature involves the study of individual materials. To present a few examples, thin polysilicon films are examined in [13], aluminum films in [6], [14], copper films in [15], gold films in [16], and nickel films in [4], [17].
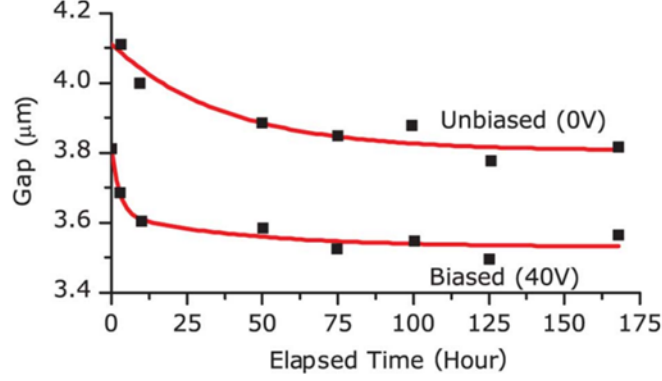
Figure 1.1. Measured gaps (black) in an RF-MEMS switch at biased and unbiased states, obtained using a confocal microscope. Trend-lines were fitted using a series of decaying exponentials. © 2011 IEEE. Reprinted, with permission, from Hao-Han Hsu, Marisol Koslowski, and Dimitrios Peroulis, An experimental and theoretical investigation of creep in ultrafine crystalline nickel RF-MEMS devices, IEEE Transactions on Microwave Theory and Techniques, August 2011.

The mechanical properties of nanocrystalline thin films are significantly affected by their microstructures. Nanocrystalline nickel samples with identical average grain sizes were noted in [18] to have varying hardness, yield stress, and ductility, with these differences attributed to microstructural differences apart from the average grain size. Bimodal grain size distributions in nickel were studied in [19] with the unsuccessful aim to increase the ductility of nanocrystalline nickel by the development of a bi-modal grain size distribution. Relationships between microstructural properties and mechanical properties are outlined in [20], and strain gradients seen in [14] after de-formation and unloading are attributed in part to the grain size distribution. It is clear from these examples that the microstructures of nanocrystalline thin films are defined by an array of characteristics beyond the mean grain size.

The distribution of grain sizes within thin films plays an important role in their mechanical properties. In-plane grain sizes are generally assumed to have a lognormal distribution. This lognormal distribution is utilized in [21], with large grains following a Hall-Petch relationship and small grains deforming under Coble creep in a combined

model of the yield stress. Lognormal grain size distributions are incorporated into the models in [22], [23] due to the high sensitivity of deformation mechanisms to grain size. An increase in the grain size distribution standard deviation was seen to broaden the transition from grain boundary strengthening to weakening in [24]. A bimodal grain size distribution was studied in [25], and a plastic strain recovery was seen which increased with the volume fraction of larger grains. A broader distribution of grain sizes in nanocrystalline nickel was seen to yield higher strength and ductility in [26], while a broader distribution of grain sizes in a combined model of Coble creep, grain boundary sliding, and grain interior dislocation motion gave a lower yield stress in [27]. The yield stress was also seen to decline with broader grain size distributions in [1].

Microstructural effects, including grain size distribution, have been suggested as causes for plastic strain recovery. Multiple studies of MEMS devices with nanocrystalline grains have shown a time-dependent recovery of what appeared to be plastic deformation. In [15] plastic strain recovery is modeled and explained by the presence of residual stresses and voids. In [28] it is suggested that residual stresses caused by inhomogeneous grain distributions drive recovery in aluminum and gold films. The explanation is that under moderate stress, small grains are imagined to remain elastic while the stresses in large grains relax by plastic deformation. Upon unloading, the stressed small grains exert tractions upon the large grains, resulting in an inhomogeneous stress distribution and consequent relaxation, in a manner similar overall to a Kelvin-Voigt model. Simulations of phase field dislocation dynamics with bimodal grain sizes also see plastic strain recovery [25], and similar simulations which include the effects of grain boundary sliding show plastic strain recovery as well [29], [30].

In deposited films, grain growth during film deposition leads to columnar grains and a gradient of grain size across the thickness of the film, meaning that smaller grains are seen on one side of the film and larger grains are seen on the reverse side [31], [32], [33], [34]. Small grains are seen at the bottom of the film when deposition begins. As deposition continues, grains whose orientations allow rapid vertical

growth outgrow those which do not. As the thickness increases, this competitive process leads to a decrease in the number of grains and an increase in the grain size as the thickness increases, as well as a columnar microstructure and a preferred crystal orientation. The effect of this microstructural characteristic on the mechanical properties of nanocrystalline films may be extrapolated from the literature on bimodal grain distributions, but in general it is not well studied.

## 1.2   RF-MEMS Switches

Radio-frequency microelectromechanical systems (RF-MEMS) are devices with characteristic lengths ranging from hundreds of nanometers to millimeters which, during their operation at radio frequencies, make use of coupling between electric fields and mechanical motion [35]. These systems serve a variety of purposes; among these purposes is their use as variable capacitors, where they may serve as variable-frequency bandpass filters [36]. RF-MEMS are a subject of research as a result of their functionality as well as their ability to replace larger components, allowing compact design of the devices in which they are applied.

RF-MEMS capacitive switches have the potential to replace alternative RF switches in applications which require low insertion loss and high linearity as well as to drive innovations in mobile handsets, satellites, base stations, and other military and civilian telecommunications systems which benefit from the re-configurability, high performance, and low cost of RF-MEMS [37], [35]. However, they suffer from a variety of failure mechanisms [37], [35], [38], [39], [40], [41], [42], with dielectric charging [43], [44], [45] and creep [46], [47], [48], [49] being prominent among them. Creep is a time-dependent and thermally activated permanent deformation that occurs at a constant load below the yield stress. This behavior is very well characterized in bulk materials [8], [50], [51], but the mechanisms of creep in nano-crystalline materials are still not as well understood [4], [17], [52], [53], [54], [55], [56].

The reliability of RF-MEMS devices has historically been a hurdle in their adoption [38], [39], [41]. Challenges introduced by the small scale of the devices and the manufacturing precision required for their reliable use have led to improvements in thin film manufacturing and testing [57], [12].

The RF-MEMS switch studied here consists of a metal membrane of nano-crystalline nickel suspended over an electrode. A simplified sketch of the system is shown in Fig. 1.2. The application of a bias voltage to the electrode results in an electrostatic force on the membrane, pulling the membrane toward the electrode and reducing the gap. For a constant applied voltage, the gap gradually but permanently decreases due to creep deformation [9]. A permanently smaller gap will result in a reduced voltage at which the membrane is pulled down toward the electrode (pull-in voltage) [9] as well as a reduction in the voltage at which the membrane releases from the electrode (pull-out voltage) because the electrostatic force on the membrane is larger and the elastic force resulting from deformation is smaller. Over time the device may become permanently pulled-in at operating voltages due to creep, resulting in 'complete failure' of the switch [37], [55], [9].
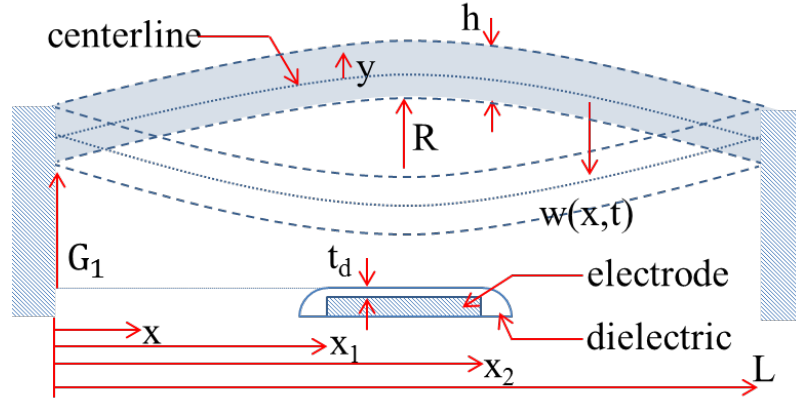


Figure 1.2. Schematic of the RF-MEMS switch with the membrane deflected in the form of an arch due to residual stresses.

The static and dynamic pull-in voltages, the pull-out voltage, and the impact velocity are measures used to estimate the reliability of the devices. These measures

are known to be sensitive to variability in the device geometry and material properties, both of which result from manufacturing processes [35], [58], [59], [60].

The effect of variations in membrane thickness also remains to be studied. Studies have been conducted into the effects of inclined supports, flexible boundary conditions, uncertain moduli, and initially curved beams [61] [62] [63]. These parameters, however, may be overshadowed by uncertainty in the beam thickness within individual devices. Variability in the thickness of one device affects both the thickness of the membrane and the air gap between the membrane and the electrode. As the membrane response is very sensitive to both of these parameters, it follows that the membrane response will also be sensitive to variability in the thickness across the length of one membrane.

## 1.3   Organization

The first chapter of this work has briefly introduced radio-frequency microelectromechanical systems (RF-MEMS).

The second chapter presents the incorporation of a Coble creep model into a one-dimensional model of the dynamic and static response of a RF-MEMS switch to electrostatic actuation. The uncertainty in the quanties of interest due to the uncertainties in the material and geometric uncertainties as creep occurs is determined.

The third chapter is an investigation into the effects of grain size distributions on the creep response of RF-MEMS switches. Membranes with multiple layers of grain sizes are compared to membranes with uniform grain sizes.

The fourth chapter introduces the variation of the membrane thickness as a source of uncertainty in the response of the RF-MEMS switch. A three-dimensional model of the membrane non-uniformity is introduced, and the one-dimensional beam model is modified to incorporate variation in thickness.

The fifth chapter summarizes the results developed in this work, and the final chapter discusses suggestions for further investigations.

## 2. UNCERTAINTY IN CREEP FAILURE WITH 1D MODEL

The goal of this chapter is to introduce creep into the material properties of the MEMS switch and to predict the effect of creep on four quantities of interest for the switch: the static pull-in voltage, the dynamic pull-in voltage, the impact velocity, and the pull-out-voltage, with uncertainties in the geometric and material constants.

Creep deformation simulations of radio-frequency micro-electro-mechanical systems (RF-MEMS) switches are presented. The analysis of these simulations includes quantification of uncertainty in the geometry, material parameters, and boundary conditions.

The switch is modeled as an Euler-Bernoulli beam that is actuated electrostatically in a fluid medium. The fluid damping is approximated with a squeeze-film model, and the beam model incorporates stretching nonlinearity in addition to Coble creep. The resulting nonlinear dynamic model is solved using a Ritz-Galerkin-based modal expansion and explicit time integration. The focus of the study is on the effect of creep as a failure mechanism and the implications of uncertainty in the device geometry, material parameters, and boundary conditions.

The degradation of the device performance due to creep is seen in decreases in the static and dynamic pull-in voltages, the pull-out voltage, and the impact velocity. We find that the variability in the experimental pull-in voltage is accounted for by the inclusion of uncertainty in the material and geometric properties. We find that the four quantities of interest decrease with time due to creep. This degradation is seen to occur more rapidly under higher loads, as expected. We note that the uncertainty in the predicted degradation increases with time as well as with increasing load.

A torsion-spring boundary condition is presented as an alternative to the assumption of a fixed-fixed boundary condition. It is found, however, that the known pull-in voltages and measured profile data are insufficient to allow for the calibration of both

the unknown residual stress and the unknown torsion spring boundary condition. For this reason the fixed-fixed boundary condition is restored. It is understood that this boundary condition assumption affects the calibrated residual stress, so the calibrated residual stress may be a poor approximation of the actual value.

## 2.1 Literature Review

In order to be able to model the dynamics of the switch and then predict the quantities of interest (QOI) that can shed light on the reliability of a MEMS device, a dynamic model of the switch in Fig. 1.2 is presented. The model used to predict the deflection of the membrane due to electrostatic actuation utilizes, as a simplification, an Euler-Bernoulli dynamic beam model. A correction to the elastic modulus is made to account for the plate-like stiffness of the membrane. The deflection is obtained through the Ritz-Galerkin method, wherein it is assumed that the beam deflection can be expressed as a linear superposition of the modeshapes of an undamped straight beam. Within the context of the Euler-Bernoulli theory, the model also accounts for beam stretching, initial curvature, residual stress, squeeze-film damping, and creep. The model takes into account non-ideal clamped (fixed-fixed) boundary conditions by modeling the boundaries as torsional springs. This allows for a range of boundary conditions to be modelled, with low spring stiffness approximating pinned-pinned boundary conditions and high spring stiffness approximating fixed-fixed boundary conditions.

Uncertainty quantification (UQ) is becoming a very useful tool in assessing the accuracy and range of applicability of the behavior predicted with simulation tools [64]. More specifically, uncertainty propagation can be used in simulations to estimate variability in the device response due to uncertainties in the geometry and material properties. Various methods exist to perform uncertainty propagation. These methods include the Monte Carlo method [65], in which samples are stochastically drawn from probability density functions (PDFs) of input parameters, Latin hyper-

cube sampling [66] and Orthogonal sampling [67], in which the samples are drawn selectively, and generalized polynomial chaos [68], [69], which involves representing the governing model equations in a stochastic framework using Galerkin projections in the parameter space of distribution functions.

This section is an extension of previous work in the literature, including especially [61] and [63], which contain experimental results upon which the calibration in this paper is based and the model which underlies the current extension, respectively. It is analogous to [46] and [48], in which models of RF-MEMS devices are extended to include creep. The underlying model is simpler in this work, and the computational requirements are fewer, which yields a much more rapid though more coarse result. It is, further, similar to [47] in its inclusion of creep in a simplified MEMS model, but the creep model in this section is theoretically rather than empirically derived, and the uncertainty due to beam geometries is included and discussed.

## 2.2 Euler-Bernoulli Beam Model

### 2.2.1 Equations of Motion

The equations of motion for a switch that accounts for both elastic behavior and creep behavior are developed in this section. The basic steps involve first a summary of the model for an elastic switch followed by the modifications that are needed to make the model applicable to a beam undergoing creep. The equation of motion for the elastic regime of the system shown in Fig. 1.2, with transverse deflection w(x,t) and including stretching, squeeze-film damping, initial curvature, and electrostatic forcing, is given by [63], [70] as

$$E_{eff} I w^{''''} + \rho b H \ddot{w} + F_{damp} = \left( \frac{E_{eff} b H}{2L} \int_0^L [(w^{'})^2 - 2 w^{'} v^{'}] dx \right) (w^{''} - v^{''}) + N b H w^{''} + F_{elec},$$

(2.1)

where $I$ is the second area moment of inertia of the beam cross-section, $\rho$ is the mass density, $b$ is the beam width, $H$ is the beam thickness, $F_{damp}$ is a damping

force per unit length due to dissipation in the medium around the beam, $L$ is the beam length, $v(x)$ is a stress-free initial deflection, $N$ is an axial stress which approximates the residual stress, and $F_{elec}$ is the electrostatic force per unit length. The parameter $E_{eff} = \frac{E}{1-\nu^2}$ is the effective modulus of elasticity, meant to account for the membrane width through the elastic moduli $E$ and $\nu$. In Equation 2.1, a prime indicates differentiation with respect to $x$, and a dot represents differentiation with respect to time. The first two terms on the left-hand side of Equation 2.1 account for the bending stiffness and the inertia while the first two terms on the right hand side represent contributions from stretching and axial stress. For the damping term $F_{damp}$, a squeeze-film gas damping model following [71] and [63] is used and takes the form:

$$F_{damp} = \frac{10.39(\frac{b}{G_1+v+\gamma-w})^{3.1}}{1 + 1.374(\frac{b}{G_1+v+\gamma-w})^{1.825}(\frac{\lambda}{b})^{0.966}} \dot{w}, \qquad (2.2)$$

where $G_1$ is the distance from the top of the dielectric to the bottom of the beam at the anchor (see Fig. 1.2), $\gamma = 10nm$ is the assumed height of any asperities on the dielectric surface, and $\lambda$ is the gas mean free path of the fluid surrounding the beam, assumed here to be ambient air with a mean free path of $\lambda = 68nm$ [72].

The effective electrostatic gap at the anchor of the beam is considered to be $g_o = G_1 + \frac{t_d}{\epsilon_r}$, where $t_d$ is the dielectric thickness, and $\epsilon_r$ is the relative permittivity of the dielectric [63]. The electrostatic force on the beam is determined by differentiating the stored energy due to capacitance, $E_s = \frac{CV^2}{2}$, with respect to $g_o$ and setting the force $F_{elec}$ to zero outside the range of the electrodes, i.e. outside the range $x_1$ to $x_2$. $V$ is the applied bias voltage and $C$ is the capacitance. A compact model of the capacitance $C$ which takes into account the electrostatic force on the sides of the beam, the fringing-field model, is used here [73]. The specific model takes the form [70]:

$$C = \frac{\epsilon_0 bL}{g_o}(1 - 0.36\frac{g_o + v - w}{b} + (\frac{0.85}{b^{0.76}} + 2.5\frac{H^{0.24}}{b})(g_o + v - w)^{0.76}). \qquad (2.3)$$

Upon differentiation and removal of the terms outside the electrode region, this capacitance gives an electrostatic force of

$$F_{elec} = \frac{\epsilon_o b V^2}{2g_o^2(1+v-w)^2}(1 + 0.204(\frac{g_0}{b})^{0.76} - 0.76(0.204(\frac{g_0}{b})^{0.76}))$$

$$(x_1 < x < x_2)$$

$$(2.4)$$

where $\epsilon_o = 8.85 * 10^{-12} F/m$ is the permittivity of free space, $x_1$ is the location of the near side of the dielectric along the axial coordinate, and $x_2$ is the location of the far side of the dielectric (see Fig. 1.2).

To incorporate plastic deformation due to creep, the total strain $\epsilon^T$ is considered as the sum of the elastic strain $\epsilon^E$ and creep strain $\epsilon^C$. The elastic strain in the beam is the result of the elastic deflection, $w^E$, and the creep strain is the result of the creep component of deflection, $w^C$. The creep strain $\epsilon^C$ can be calculated from the constitutive equations for secondary, or steady-state, creep strain rates with no hardening [8], [9],

$$\dot{\epsilon}_{ij}^C = A_c \frac{\sigma_{ij}^d}{\sigma^{vm}}(\frac{\sigma^{vm}}{\sigma_y})^n \tag{2.5}$$

where $\dot{\epsilon}_{ij}^C$ is the creep strain rate, the stress exponent is $n = 1$ for Coble creep, $\sigma_y$ is the yield stress, $\sigma_{ij}^d = \sigma_{ij} - \frac{1}{3}\sigma_{kk}\delta_{ij}$ is the deviatoric stress tensor, $\sigma^{vm}$ is the von Mises stress given by

$$\sigma^{vm} = \sqrt{\frac{1}{2}[(\sigma_{11} - \sigma_{22})^2 + (\sigma_{22} - \sigma_{33})^2 + (\sigma_{33} - \sigma_{11})^2 + 6(\sigma_{23}^2 + \sigma_{31}^2 + \sigma_{12}^2)]} \tag{2.6}$$

and $A_c$ is the creep constant defined as

$$A_c = A\frac{\delta_b D_{b0}e^{-Q_b/RT}}{kT}(\frac{b_b}{d})^3. \tag{2.7}$$

The material constant A has a range of estimated values for nickel, varying from nearly 40 [8], [17] up to 1000 [9]. In the above equation $\delta_b$ is the grain boundary thickness, $D_{b0}$ is the grain boundary diffusion coefficient, $Q_b$ is the activation energy, $R$ is the ideal gas constant, $T$ is the absolute temperature, $k$ is the Boltzmann constant,

$b_b$ is the Burgers vector, and $d$ is the average grain size. The value of $A_c$ in Table 2.1 is taken from the work of Mahadevan et al. [74], which also draws data from [9].

In the context of the Euler-Bernoulli beam theory, only the axial component of the deviatoric stress is relevant here, and it may be found as

$$\sigma_{11}^d = \frac{2}{3}\sigma_{11}. \tag{2.8}$$

Utilizing the relations from elementary beam theory under the kinematic assumptions of Euler-Bernoulli beam theory [75], and splitting the deflection into $w^E$ resulting from the elastic strain and $w^C$ resulting from the creep part of the strain,

$$\sigma_{11} = -\frac{My}{I},$$
$$M = EI(w^E)'', \tag{2.9}$$

where $M$ is the bending moment in the beam and $y$ is the distance above the neutral axis of the beam. Now combining Equation 2.7 and Equation 2.8 to relate the deviatoric stress to the elastic deflection we obtain

$$\sigma_{11}^d = -\frac{2}{3}Ey(w^E)''. \tag{2.10}$$

For $n = 1$ in the equation for the creep rate, Equation 2.5, the creep strain rate $\dot{\epsilon}_{ij}^C$ is related to the creep deflection in the same manner as the elastic strain and deflection are related in elastic beam theory, with

$$\epsilon_{11}^C = -y(w^C)''. \tag{2.11}$$

where $w^c$ is that portion of the deflection under no load which results from the creep strain. Differentiating both sides with respect to time gives a second equation for the creep strain rate,

$$\dot{\epsilon}_{11}^C = -y(\dot{w}^C)''. \tag{2.12}$$

Substituting Equation 2.12 into Equation 2.5 gives the relation

$$(\dot{w}^C)'' = \frac{2A_cE}{3\sigma_{y0}}(w^E)''. \tag{2.13}$$

Equation 2.1, which was written in terms of the elastic deflection $w^E$, is now rewritten to include the deflection $w^C$ where it is appropriate. The electrostatic force, the inertial terms, and the damping terms depend on the total deflection, but the time derivatives of the deflection due to creep are neglected in the inertial and damping terms due to their small magnitude. As plastic strain causes no stress, the bending stiffness term depends only on the elastic deflection. The stretching force and the residual stress term will depend on the elastic deflection alone. Therefore, Equation 2.1 can be rewritten as

$$EI(w^E)'''' + \rho b H \ddot{w}^E + F_{damp} =$$
$$(\frac{EbH}{2L} \int_0^L (((w^E)'')^2 - 2(w^E)'v')dx)((w^E)'' - v'') + n(w^E)'' + F_{elec} \tag{2.14}$$

where the creep deflection $w^C$ is incorporated into the electrostatic term alone.

Equations 2.13 and 2.14 form a two-degree-of-freedom system of equations for the determination of the beam's elastic deflection $w^E$ and creep deflection $w^C$.

The inclusion of torsion-spring boundary conditions permits the simulation of beams with a wide range of anchor conditions. This is important for practical switches as it is rare that a switch with ideal boundary conditions can be fabricated. The torsion-spring boundary conditions for an Euler-Bernoulli beam are:

$$\begin{aligned}
w(0) &= 0, \\
w(L) &= 0, \\
E_{eff}Iw''(0) &= Kw'(0), \\
E_{eff}Iw''(L) &= -Kw'(L)
\end{aligned} \tag{2.15}$$

where $K$ is the torsion spring stiffness.

As previously stated, a fixed-fixed boundary condition can be approached with a large torsion spring stiffness, $K$, and a pinned-pinned boundary condition can be simulated with the value of $K = 0$. Residual stress in the membranes is biaxial, but the axial component of the residual stress alone is considered due to the width of the membranes and the assumptions of the Euler-Bernoulli beam theory. The mode

shapes and frequencies which result from these boundary conditions for an axially loaded elastic beam are developed in reference [75].

Dielectric charging is the buildup of carriers in the dielectric film which coats the electrode; see Fig. 1.2. Its effect is to increase the electrostatic force on the membrane, resulting in a decreased PIV. It has remained difficult to separate the effect of dielectric charging from those of creep unless the dielectric is removed in the experiments. In the present work dielectric charging has been neglected.

## 2.2.2   Solution Method

The coupled Equations 2.13 and 2.14 are discretized using the Galerkin technique, which needs to be slightly modified from the direct application in the literature on microbeams [63], [70] as there are now two coupled equations. To solve Equations 2.13 and 2.14 the following nondimensional quantities are defined:

$$
\begin{aligned}
\hat{x} &= \frac{x}{L}, \\
\hat{t} &= \frac{t}{\tau} = \frac{t}{\sqrt{\frac{\rho b h L^4}{EI}})}, \\
\hat{w} &= \frac{w}{g_o}, \\
\hat{v} &= \frac{v}{g_o}, \\
\hat{x}_1 &= \frac{x_1}{L}, \\
\hat{x}_2 &= \frac{x_2}{L}, \\
\hat{N} &= \frac{N L^2}{EI}, \\
\omega_n &= \frac{\omega_n}{\sqrt{\frac{EI}{\rho b h L^4}}}.
\end{aligned}
\tag{2.16}
$$

The time $t$ is nondimensionalized with a constant $\tau = \sqrt{\frac{\rho b H L^4}{EI}}$. After nondimensionalization, Equations 2.13 and 2.14 can be expressed as:

$$(\hat{w}^E)'''' + \rho b h \ddot{\hat{w}}^E + \hat{F}_{damp} =$$
$$(6(\frac{g_o}{H^2})^2 \int_0^1 [((\hat{w}^E)'')^2 - 2(\hat{w}^E)'\hat{v}']dx)((\hat{w}^E)'' - \hat{v}'') + \hat{N}(\hat{w}^E)'' + \hat{F}_{elec}, \tag{2.17}$$

$$(\dot{\hat{w}}^C)'' = (\hat{w}^E)'' \frac{2A_c E}{3\sigma_{y0}} \sqrt{\frac{\rho b H L^4}{EI}}. \tag{2.18}$$

In order to perform a Galerkin approximation for the model Equation 2.17 and Equation 2.18, the initial shape of the membrane also needs to be approximated through an expansion. Here, the initial deflection $\hat{v}$ will be expanded as a sum of $M$ sine functions and their coefficients $p_i$ in the manner

$$\hat{v}(\hat{x}) \approx \Sigma_{i=1}^M p_i sin(\pi\hat{x}i), \tag{2.19}$$

where the coefficients $p_i$ are found from

$$p_i = \int_0^1 \hat{v} sin((\pi\hat{x}i)d\hat{x}), \tag{2.20}$$

The solution $\hat{w}^T(\hat{x}, \hat{t})$ is also assumed to be a linear combination of $M$ orthonormal linear modeshapes $\phi_i(\hat{x})$ of the undamped and straight beam, with $M$ time-dependent coefficients $u_i^T(\hat{t})$:

$$\hat{w}^T(\hat{x}, t) = \Sigma_{i=1}^M \hat{u}_i^T(\hat{t})\phi_i(\hat{x}). \tag{2.21}$$

It should be noted that the modeshapes $\phi_i$ are the solutions to the eigenvalue problem

$$\phi_i'''' = \hat{N}\phi_i'' + (\hat{\omega}_i)^2\phi_i \tag{2.22}$$

with appropriate clamped-clamped boundary conditions for a straight beam, and $\hat{\omega}_i$ is the normalized natural frequency of the $i$th mode.

The nondimensional total deflection $\hat{w}^T$ and the coefficients $\hat{u}_i^T$ are decomposed into elastic and plastic parts as $\hat{w}^T = \hat{w}^E + \hat{w}^C$ and $\hat{u}_i^T = \hat{u}_i^E + \hat{u}_i^C$. Substituting the expansions defined by Equations 2.19 to 2.22 into the equations of motion (2.17) and (2.18) in all but the damping and electrostatic terms, multiplying through by the

orthonormal modeshapes $\phi_n$, and finally integrating across the length of the beam yields $2M$ ordinary differential equations,

$$\ddot{\hat{u}}_n^E + \omega_n^2 \hat{u}_n^E + \int_0^1 \hat{F}_{damp}\phi_n d\hat{x} =$$

$$6(\frac{g_0}{h})^2 \Sigma_{i,j,k=1}^M (\hat{u}_i^E \hat{u}_j^E \hat{u}_k^E * \int_0^1 (\phi_i'\phi_j' d\hat{x}) * \int_0^1 (\phi_k''\phi_n d\hat{x}))$$

$$+ 6(\frac{g_0}{h})^2 \Sigma_{i,j,k=1}^M (\hat{u}_i^E \hat{u}_j^E \hat{u}_k^E * \int_0^1 (\pi j \phi_i' cos(\hat{x}\pi j)dx) * \int_0^1 (\phi_k''\phi_n d\hat{x}))$$

$$+ 6(\frac{g_0}{h})^2 \Sigma_{i,j,k=1}^M (\hat{u}_i^E \hat{u}_j^E p_k * \int_0^1 (\phi_i'\phi_j' d\hat{x}) * \int_0^1 (-\pi^2 k^2 sin(\hat{x}\pi k)\phi_n d\hat{x})) \qquad (2.23)$$

$$+ 6(\frac{g_0}{h})^2 \Sigma_{i,j,k=1}^M (\hat{u}_i^E p_j p_k * \int_0^1 (\pi j \phi_i' cos(\hat{x}\pi j)d\hat{x}) * \int_0^1 (-\pi^2 k^2 sin(\hat{x}\pi k)\phi_n d\hat{x}))$$

$$+ \int_0^1 (\hat{F}_{elec}\phi_n d\hat{x}),$$

$$\dot{\hat{u}}_n^c = \frac{2\tau A_c E}{3\sigma_{y0}}\hat{u}_n^E, \qquad (2.24)$$

for $n = 1, 2, 3, ..., M$.

Because the elastic response and creep response occur at different timescales, this system of equations is stiff. For this reason, the transient motion is solved numerically in MATLAB with the built-in stiff ODE solver ode23s [76].

### 2.2.3  Determination of Quantities of Interest

The static PIV is the largest DC bias voltage which may be applied steadily without the beam being pulled-in. It is calculated by setting the time-dependent terms in the equations of motion, Equations 2.23 and 2.24, to zero, choosing a location on the beam, assuming a range of deflections from zero through contact for that point, and solving for the corresponding voltages required to achieve those deflections. This technique is described in more detail in [63]. The result of this calculation is a graph of voltage against deflection, as seen in [63] and many earlier works. The largest voltage on this graph is the static PIV. Fig. 2.1 is a sketch of this graph of displacement against voltage, and the static PIV is highlighted.

Similarly, if the applied voltage is reduced after pull-in, the membrane separates from the dielectric. The minimum voltage required to maintain contact is defined as the pull-out voltage, and it is drawn from the same graph of displacement against applied voltage shown in Fig. 2.1.
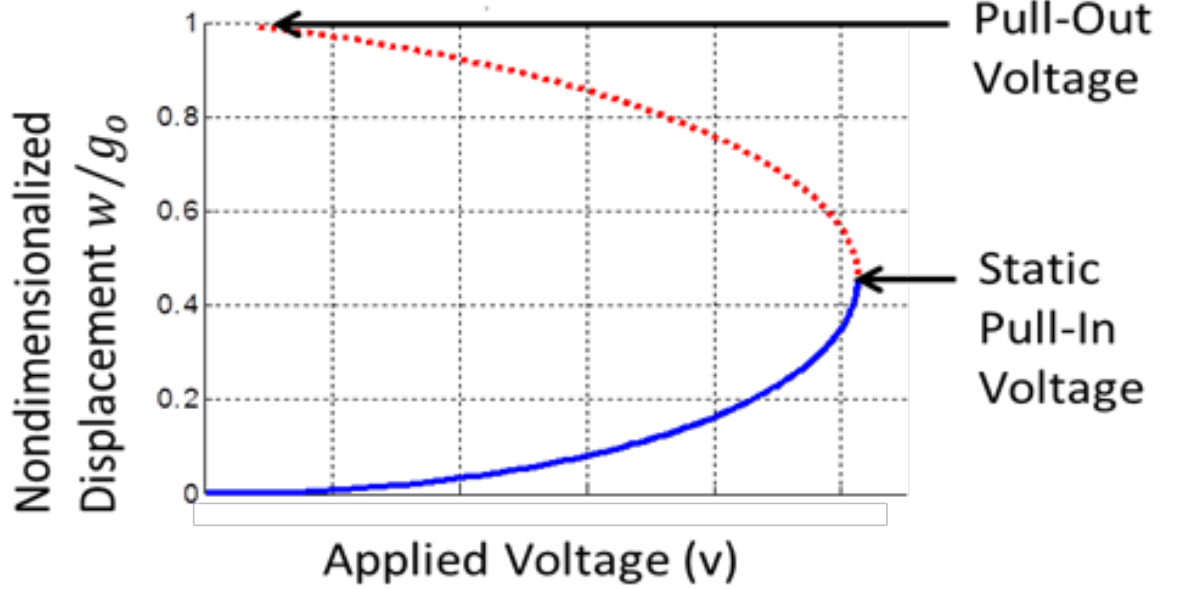


Figure 2.1.  Example of a displacement-voltage graph for an electrostatic switch.

The dynamic pull-in voltage is defined here as the DC voltage that causes pull-in when applied as a sudden step increase from 0 volts. In order to evaluate the dynamic pull-in voltage, the step voltage is applied and the equations are integrated to arrive at the transient behavior of the beam, which is solved for over several oscillations. If the beam does not pull in, as is indicated by the transient motion settling to a deflected equilibrium position, it is reset to its initial conditions and a larger voltage is attempted. If the beam pulls in, a smaller voltage is attempted until the smallest applied voltage that produces dynamic pull-in is found.

The velocity of the beam when it comes in contact with the dielectric can be used to quantify the damage that occurs during contact [35]. During the transient

simulations used to determine the dynamic pull-in voltage, the impact velocity is calculated as the velocity of the section of the beam that first contacts the dielectric.

Note that all the quantities defined here (the static and dynamic PIVs, the pull-out voltage, and the contact or impact velocity) are instantaneous responses, while creep deformation occurs over a longer time scale. However, if these QOI are calculated after a period of creep deformation leading to a degradation of the switch response, their values significantly change.

## 2.3   Model Calibration, Validation, and Sensitivity Analysis

This section focuses on calibrating the various material and geometric parameters of the model and understanding the sensitivity to these parameters by comparing the simulated results to the experiments in [61]. The sensitivity of the PIV to the geometric parameters is calculated using the beam model developed in Section II.

### 2.3.1   Experimental Characterization

Table 2.1.  Parameters of the Switch from References [61], [74], [77].

| Symbol | Quantity | Nominal Value |
|---:|---|---|
| $b$ | beam width | 120 $\mu$m |
| $\nu$ | Poisson's ratio | 0.31 |
| $\epsilon_r$ | relative permittivity | 7.9 |
| $E$ | Young's modulus | 197.3 GPa |
| $t_d$ | dielectric thickness | 200 nm |
| $L_d$ | dielectric length | 260 $\mu$m |
| $A_c$ | creep constant | 1.52e-10/s |

The geometric and material parameters are extracted from [61] and are shown in Table 2.1. The modulus of elasticity of the nanocrystalline nickel membrane for the same batch of membranes was estimated by Cantwell et al. in [77] by measuring the crystallographic texture with x-ray diffraction and applying those measurements to calculate a texture-weighted Hill polycrystal elastic average. These calculations for two batches result in moduli of E=194.7±1.4 GPa and E=199.9±1.1 GPa. The mean of 197.3 GPa is used here as the elastic modulus. The device geometry measurements are from 44 devices with nominal length $400\mu$m and 46 devices with nominal length $500\mu$m. The variability in the measured thickness $H$, anchor gap $G_1$, and rise $R$ of the 90 devices is shown in Fig. 2.2 and Fig. 2.3, along with best-fit normal distributions.



(a)

(b)

(c)
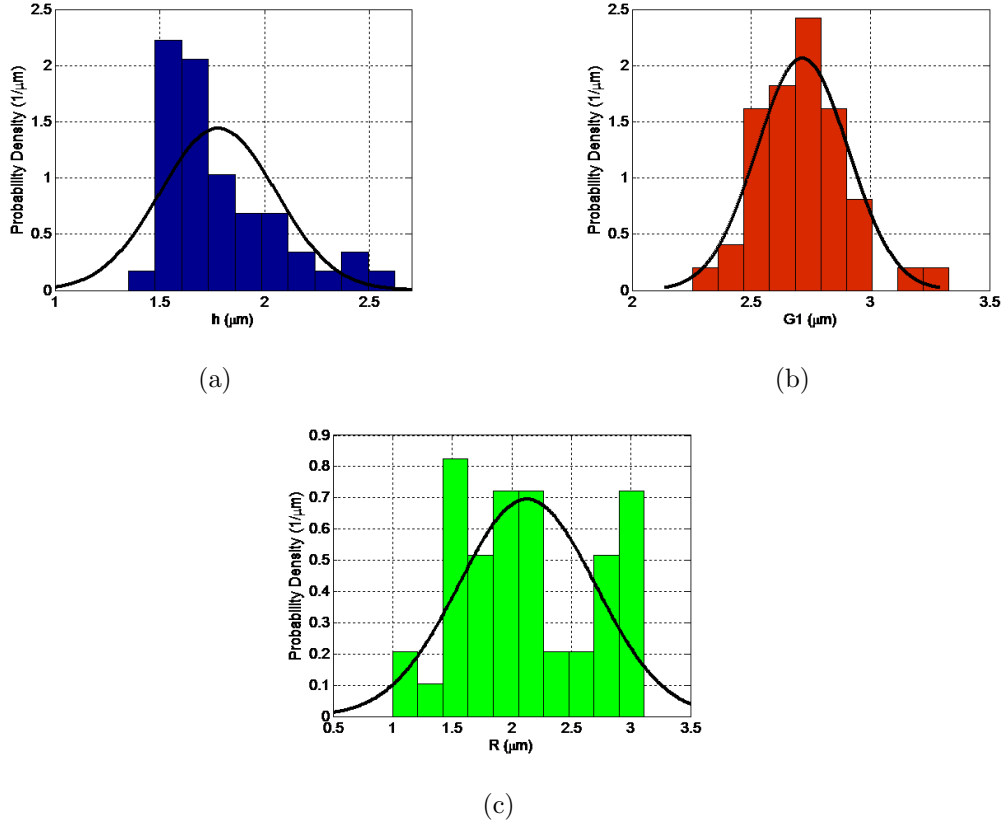
Figure 2.2. Experimentally measured parameters with fitted normal PDFs for L= 500-$\mu$m beams: (a) Thickness $H$, (b) Anchor gap $G_1$, and (c) Midpoint rise $R$.

(a)



(b)



(c)
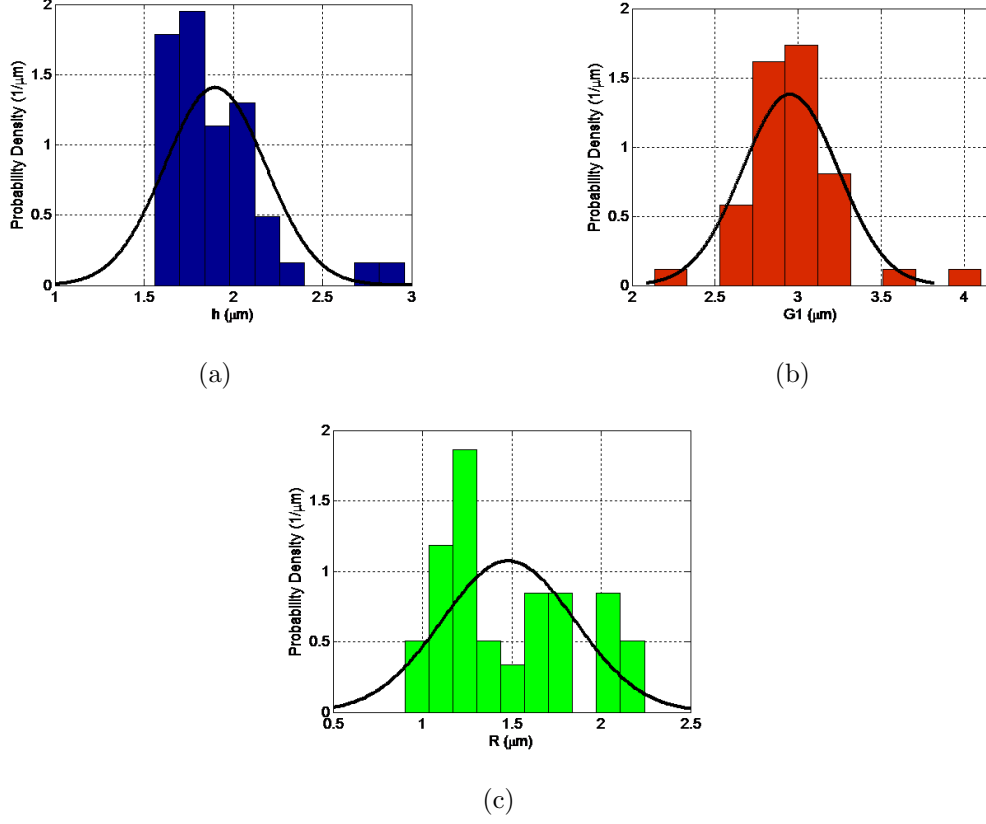
Figure 2.3. Experimentally measured parameters with scaled fitted PDFs for the 400-$\mu$m beams: (a) Thickness $H$, (b) Anchor gap $G_1$, and (c) Midpoint rise $R$.

The normal probability density function (pdf) is given by

$$P = \frac{1}{\sigma\sqrt{2\pi}}e^{-\frac{(x-\mu)^2}{2\sigma^2}} \tag{2.25}$$

where $\sigma$ is the standard deviation, and $\mu$ is the mean value. The chosen definition of the standard deviation $\sigma$ for a statistical quantity is

$$\sigma = \left(\frac{1}{n-1}\Sigma_{i=1}^{n}(x_i - \bar{x})^2\right)^{\frac{1}{2}} \tag{2.26}$$

where $n$ is the number of samples, $x_i$ is the measurement of the $i$th sample, and $\bar{x}$ is the mean of all the samples.

Table 2.2.  Measured Parameters of $500 - \mu$m Beams [77].

| Symbol | Quantity | Mean Value | Std. Dev. |
|---|---|---|---|
| PIV | Measured static pull-in voltage | 77 V | 21 V |
| $G_1$ | anchor gap | 2.72 $\mu$m | 0.19 $\mu$m |
| $R$ | rise | 2.13 $\mu$m | 0.57 $\mu$m |
| $H$ | beam thickness | 1.78 $\mu$m | 0.28 $\mu$m |

Table 2.3.  Measured Parameters of 400-$\mu$m Beams [77].

| Symbol | Quantity | Mean Value | Std. Dev. |
|---|---|---|---|
| PIV | static pull-in voltage | 100 V | 24 V |
| $G_1$ | anchor gap | 2.95 $\mu$m | 0.29 $\mu$m |
| $R$ | rise | 1.48 $\mu$m | 0.37 $\mu$m |
| $H$ | beam thickness | 1.90 $\mu$m | 0.28 $\mu$m |

The mean values and standard deviations of the measured thickness $H$, anchor gap $G_1$, and rise $R$ of the 90 devices are shown in Table 2.2 and Table 2.3. The mean and standard deviation of the PIV is also shown in Table 2.2 and Table 2.3.

The variability or uncertainty in the other geometrical and material parameters are not shown because the sensitivity of the quantities of interest to these parameters is small in comparison to the sensitivity of the quantities of interest to $H$, $G_1$, and $R$ [63].

A multivariate normal PDF is fit to the experimentally measured values of $H$, $G_1$, and $R$ to study correlations between these input variables. The form of the multivariate normal PDF is

$$P = \frac{1}{\sqrt{|\Sigma|(2\pi^{d_v})}} e^{-\frac{1}{2}(\xi-\mu)\Sigma^{-1}(\xi-\mu)} \qquad (2.27)$$

where $P$ is the probability density for any chosen vector of variable values $X$, $\Sigma$ is the covariance matrix, $d_v = 3$ is the quantity of variables, and $\mu$ is the vector of means. The mean values of these three variables are in Table 2.2 and Table 2.3, and the vectors of means are ordered corresponding to $H$, $G_1$, $R$. The covariance matrix for the 500-$\mu$m membranes is given by

$$\Sigma = \begin{pmatrix} 0.0766 & -0.0002 & 0.0028 \\ -0.0002 & 0.0373 & 0.0177 \\ 0.0028 & 0.0177 & 0.3291 \end{pmatrix} (\mu m)^2$$

and the covariance matrix for the 400-$\mu$m membranes is given by

$$\Sigma = \begin{pmatrix} 0.0803 & 0.0006 & -0.0007 \\ 0.0006 & 0.0836 & -0.0097 \\ -0.0007 & -0.0097 & 0.1382 \end{pmatrix} (\mu m)^2$$

It is evident from these matrices that the covariance is negligible. The experiments show no correlation between the rise $R$ and the anchor gap $G_1$, as illustrated in Fig. 2.4 for both sets of devices. Though not shown, the experiments show no correlation between the membrane thickness and the gap $G_1$.



(a)                                                  (b)
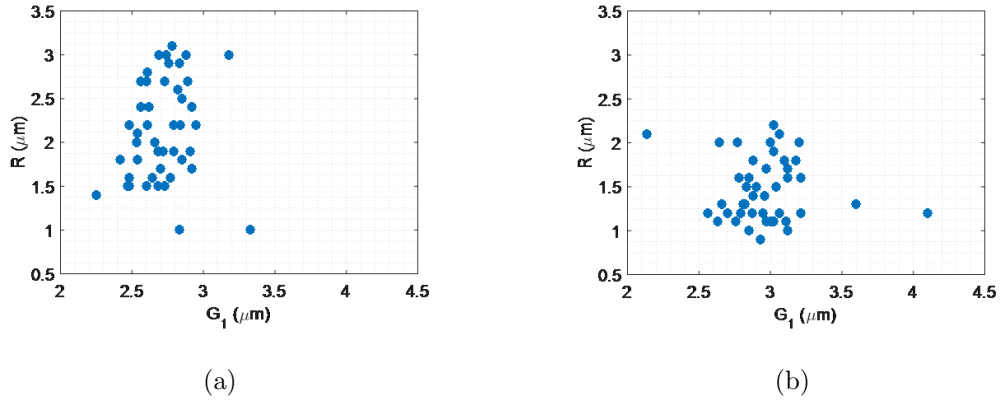
Figure 2.4. $G_1$ plotted against $R$ for (a) 500-$\mu$m membranes and (b) 400-$\mu$m membranes, illustrating no correlation between the gap $G_1$ and the rise $R$.

## 2.3.2 Sensitivity Analysis
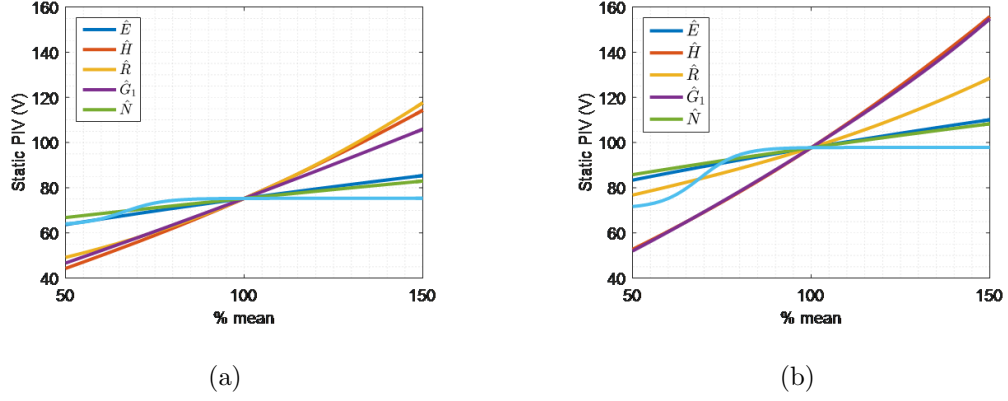


Figure 2.5.  Sensitivity of the static PIV to the normalized modulus $E$, thickness $H$, rise $R$, gap $G_1$, torsion spring stiffness $K$, and residual stress $N$ for the 400- and 500-$\mu$m beam.

Fig. 2.5 shows the sensitivity of the PIV to the Young's modulus $E$, thickness $H$, rise $R$, anchor gap $G_1$, boundary torsion spring constant $K$, and residual stress $N$. The PIV is determined as previously described, by determining quasi-static solutions to Equations 2.23 and 2.24. The variables in the plot are normalized by the mean value, and a range of $\pm 50$ percent in the thickness $H$, gap $G_1$, rise $R$, and residual stress $N$, is shown. The residual stresses are calibrated in a later section but are included here to illustrate their effect. The calibrated residual stresses are shown in Table 2.4. A range of torsion spring values from $1 * 10^{-8}$ to 1 N·m/rad is shown, as it encompasses the transition from fixed-fixed to pinned-pinned boundary conditions. The torsion spring values are normalized and plotted as a semi-log plot, so that the mean value is $1 * 10^{-4}$ N·m/rad, at which value the beams are effectively fixed-fixed. The mean values of each parameter are different for the 400-$\mu$m membranes and the 500-$\mu$m membranes, and so the two sets of membranes are normalized separately. For each set of membranes, the normalized input parameters are written as

$$\hat{E} = \frac{E}{\mu_E * 100}$$

$$\hat{H} = \frac{H}{\mu_H * 100}$$

$$\hat{R} = \frac{R}{\mu_R * 100}$$

$$\hat{G}_1 = \frac{G_1}{\mu_{G_1} * 100} \tag{2.28}$$

$$\hat{K} = 1 + \frac{ln(K) - \mu_{ln(K)}}{ln(K)_{max} - ln(K)_{min}}$$

$$\hat{N} = \frac{N}{\mu_N * 100}$$

where $\mu$ is the mean value. In the beam model, the PIV is most sensitive to changes in the normalized beam thickness $\hat{H}$, the gap $\hat{G}_1$, and the rise $\hat{R}$. A distinct sensitivity to the torsion spring stiffness is seen below 1e-5 $N \bullet m/rad$, where the boundary condition begins to transition from a fixed-fixed to a pinned-pinned boundary condition. This sensitivity is larger in the 400-$\mu$m beams. The profile of the beam is treated as a half-sinusoidal curve from a minimum value of $G_1$ to a maximum of $G_1 + R$ at the center. The effect of this assumption is studied in a later section.

### 2.3.3 Calibration of the Residual Stress

The calculated static PIVs for the 400-$\mu$m and 500-$\mu$m membranes are fitted to their experimental static PIVs by calibrating the residual stress through the Metropolis-Hastings Markov chain Monte Carlo (MCMC) algorithm [65] using the Purdue Uncertainty Quantification (PUQ) framework [78].

The general Metropolis-Hastings MCMC algorithm consists of choosing an initial value for all of the unknown parameters, then iteratively proposing new values for the parameters from their assumed distributions, and accepting or rejecting the new values according to a calculated likelihood ratio $\alpha$. The likelihood ratio describes how

much more likely the proposed values are than the current values, given the observed data. The likelihood ratio is defined as:

$$\alpha = \Sigma_{i=1}^{m} \frac{d_i - D_i(\theta_1)^2}{(d_i - D_i(\theta_2))^2} \tag{2.29}$$

where $m$ is the number of experimental data points, $d_i$ is the $i$th observed value of the output, and $D_i$ is the $i$th value of the simulation output given the parameter values $\theta$. Likelihood ratios $\alpha$ may vary depending on the sampling algorithm chosen. According to the general Metropolis-Hastings algorithm, the proposed location is accepted automatically if $\alpha > 1$, and is otherwise accepted with a probability $\alpha$.

To illustrate, for the 400-$\mu$m membranes, $m = 1$ is chosen for each membrane because each of the 44 membranes is being individually calibrated. With pull-in voltage as a calibration quantity, the parameter $d$ is the observed pull-in voltage, $D$ is the simulated pull-in voltage, $\theta_1$ will be the static PIV at the proposed step, and $\theta_2$ will be the static PIV at the current step.

Rather than repeatedly simulate the pull-in voltage using the beam model, a compact model based on a third-degree polynomial interpolation of the pull in voltage is used. The interpolation is performed for a range of residual stress from -20 MPa to 50 MPa and for the experimentally measured ranges of the rises $R$, thickness $H$, and gap $G_1$ and clamped boundary conditions. A half-sinusoidal beam profile is assumed. The distributions of residual stress that result from the calibration are shown in Table 2.4.

For the 500-$\mu$m membrane the calibration results in some compressive stress values. The critical buckling load for a fixed-fixed beam using the Euler buckling formula is given by

$$P_{cr} = \frac{4\pi EI}{L^2} \tag{2.30}$$

Under this approximation, it is estimated that 8 MPa compressive stress will cause buckling in the 500-$\mu$m membranes, which is outside of the stress range predicted in the calibration.

It should be noted that this fitting covers up other sources of error, such as the deviation of the membrane profile from a half-sinusoidal curve, errors due to simplifying assumptions, such as beam model, or the distributions chosen to fit the measured distributions of other input parameters. Thus the distribution of the residual stress found may cause the simulations to match experiments, but it may not be representative of the true value of the residual stress.

### 2.3.4 Sensitivity to the Profile
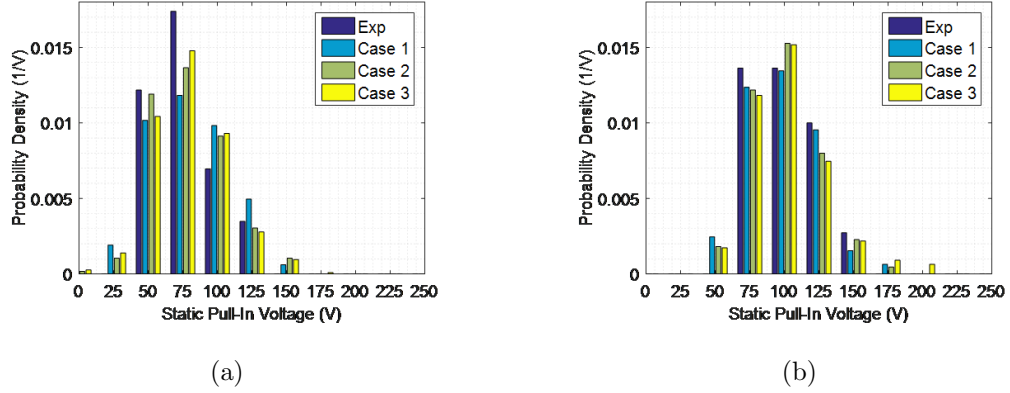


Figure 2.6. PDFs of the experimental and simulated PIVs for (a) the 500-$\mu$m beams, and (b) the 400-$\mu$m beams.

Alternative fits to the profile of the membrane are considered in order to study the sensitivity and uncertainty, resulting in three cases. In each case, ten simulations are performed for each of the 90 devices by sampling the calibrated distribution of residual stress in Table 2.4. The three cases are described as follows:

• Case 1: For each device, the measured profile of the membrane is fitted by seven terms in the expansion in 2.19.

• Case 2: This is identical to Case 1, except that the profile of the membrane is represented by a half-sinusoidal curve. This case is used to calibrate the residual stress in Table 2.4.

• Case 3: For each set of beams, 480 samples are drawn from the normal distributions in Table 2.2 and Table 2.3 of the input parameters. The profile of the membrane is represented by a half-sinusoidal curve.

For all the cases, the normal distributions of the calibrated residual stress in Table 2.4 are sampled in each simulation. The predicted distributions of PIV are shown in Fig. 2.6 and the mean and standard deviation are shown in Tables 2.5 and 2.6. Case 2 was used to calibrate the distribution of the residual stress previously used, and therefore this case provides the best fit to the experimental PIVs. The use of full profiles in Case 1 had little effect on the predicted PIV for either set of beams. The similarity of the results of Case 1, Case 2, and Case 3 suggest that the choices of a half-sinusoidal profile and normal distributions to represent the variability in the thickness, anchor gap, and midpoint was reasonable.

### 2.3.5 Calibration of the Boundary Conditions

The torsion spring stiffness value can also be considered as a candidate for calibration. A response surface is generated for the PIV as a function of the residual stress and the torsion spring constant. The Metropolis-Hastings algorithm is then used to calibrate the residual stress and torsion spring constants. Fig. 2.7 shows resulting representative pairs of residual stress and torsion spring constants for one membrane which provide a PIV in agreement with the experimental observation. The experimental error in the measurement of the PIV is assumed to have a mean of 0V and a standard deviation of 2.5V. It is evident from Fig. 2.7 that for a wide range of torsion spring stiffness, a residual stress within the range of 0-50 MPa will allow the PIV to be fitted to experimental data.

An attempt made by the authors to separate the contribution of the residual stress and the boundary conditions was unsuccessful. It was hypothesized that the boundary condition would affect the shape of the gap-voltage curve. Measurements of the gap of each beam as a function of the applied voltage were compared to simulated

Figure 2.7. Values of residual stress and torsion spring stiffness for which simulation PIV fits the experimentally measured PIV for one $500\mu$m beam.

values of the same, but despite the additional information, it remained possible to choose any value of the torsion spring constant and find a residual stress value within the range of 0-50 MPa which would allow the simulated voltage-deflection curve to reasonably fit the experimental values. Because one of the two unknown parameters could assume any value, the contributions and calibrations of the two parameters remained unidentifiable.

For the above reason, the torsion spring stiffness is fixed to a single value equivalent to a fixed boundary condition in the following analyses. It follows that the calibrated values of the residual stress do not necessarily represent the actual values which might be found with direct experimental measurement of the residual stress or by calibration with additional data; it is possible, for example, to calibrate the residual stress using measurements of the natural frequencies of the membranes, as seen in [47], where the residual stresses in similar beams were found to have a mean of 2 MPa and a standard deviation of 5 MPa.

In addition to the residual stress calibration with the simplified profile of Case 2, the residual stresses of the two sets of beams were calibrated while using the true

profiles of Case 1. This calibration yields distributions of residual stress with mean values of 7.2 MPa and 14.5 MPa for the 500-$\mu$m and 400-$\mu$m beams, respectively. These values are within 2 MPa of the calibration with simplified profiles seen in Table 2.4 and are well within the standard deviations of 6.8 MPa for both sets of beams. This result suggests that rapid simulations of the PIV using simplified profiles may offer sufficient accuracy for the beams considered.

## 2.4  Simulation of Reliability under Creep Deformation

The effect of creep on the QOI is now studied by simulating creep deformation under a constant DC bias voltage, and then calculating the QOI as described in Subsection 2.2.3. In all of these simulations, the residual stress is sampled randomly from the calibrated normal distributions in Table 2.4, and clamped boundary conditions are assumed.

### 2.4.1  Simulations of Creep Deformation

The static and dynamic pull-in voltages, impact velocity, and pull-out voltage were determined after a constant applied voltage was applied during periods of time of up to 40000 hours.

To include uncertainty in the simulations, 480 simulations were run for each applied voltage and extent of time, with random samples of the input parameters drawn from the multivariate PDFs which were fitted to the measured values of the $H$, $G_1$, and $R$ for the 500-$\mu$m beams, as well as from the calibrated residual stress distribution with fixed-fixed boundary conditions. The creep coefficient $A_c$ in Table 2.1 comes from estimation with Bayesian networks [74] and was treated here as a normal distribution with a standard deviation of 10% of its nominal value. Results for four applied voltages are shown in Fig. 2.8. The error bars include the median 10% of the simulation pull-in voltages.

Table 2.4.  Calibrated Residual Stresses of 500-$\mu m$ and 400-$\mu m$ beams.

| Beam Set | Calib. $\sigma_{resid}$ Mean (MPa) | Calib. $\sigma_{resid}$ Std. Dev. (MPa) |
|---|---|---|
| 500 $\mu m$ | 8.4 MPa | 6.8 MPa |
| 400 $\mu m$ | 12.6 MPa | 6.8 MPa |

Table 2.5.  Static PIV for 500-Micron Beams with Various Fits to Uncertain Parameters.

| Description | PIV Mean | PIV St Dev |
|---|---|---|
| Case 1 | 78 V | 29 V |
| Case 2 | 78 V | 26 V |
| Case 3 | 77 V | 27 V |

Table 2.6.  Static PIV for 400-Micron Beams with Various Fits to Uncertain Parameters.

| Description | PIV Mean | PIV St Dev |
|---|---|---|
| Case 1 | 98 V | 25 V |
| Case 2 | 99 V | 24 V |
| Case 3 | 101 V | 29 V |

### 2.4.2  Conclusions

Simulations of the response of a radio frequency micro-electro-mechanical-systems (RF-MEMS) switch composed of a nanocrystalline nickel membrane undergoing creep deformation were presented. The model includes a Coble creep formulation incorporated into a beam model of an electrically actuated RF-MEMS switch with fixed-fixed and torsion-spring boundary conditions. The pull-in voltage of the model was calibrated to experimental results before creep was simulated. The resulting degradation

of the device behavior due to creep as well as the implications of uncertainty in the device geometry and material parameters were studied, and it was shown that the range of uncertainty in the input parameters yielded a large range of uncertainty in the quantities of interest which increased over time due to creep.

A torsion-spring boundary condition was considered as a possible improvement in the model. If the residual stress in each beam were known, calibration of the effective torsion spring stiffness of each beam would be possible. Because the residual stresses were unknown, it was not possible to calibrate a reliable value of the torsion spring stiffness despite the wealth of PIV measurements and voltage-gap curves. Fig. 2.9 shows a representative sample of pairs of residual stress and torsion spring constants that result in a PIV in agreement with the experimental observation within the tolerance of the measured PIV. The variation of the residual stress and the torsion spring stiffness was carried out with the Metropolis-Hastings algorithm. It is evident from Fig. 2.9 that for any chosen value of the torsion spring stiffness, some residual stress within the chosen range of 0-50 MPa will allow the PIV to be fitted to experimental data, so that neither parameter is identifiable. The large uncertainty in the residual stresses covered up any effect of the effective torsion spring boundary condition. To continue the analysis, the boundary condition was set to be fixed-fixed and the residual stress was calibrated alone.

When creep occurs, the devices pull in after a period of hours to months at applied voltages below the pull-in voltage. A distinct decrease in device lifetime, defined as the time to failure, is noted with increasing voltage. This is expected; larger applied voltages lead to larger electrostatic forces and thus larger stresses, accelerating creep deformation.
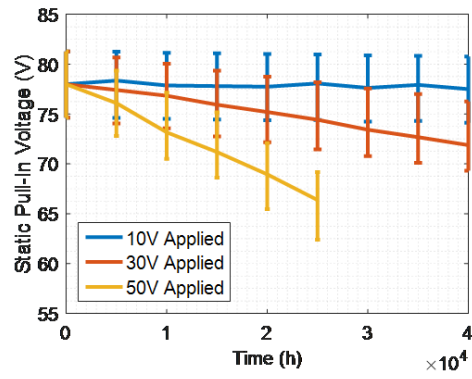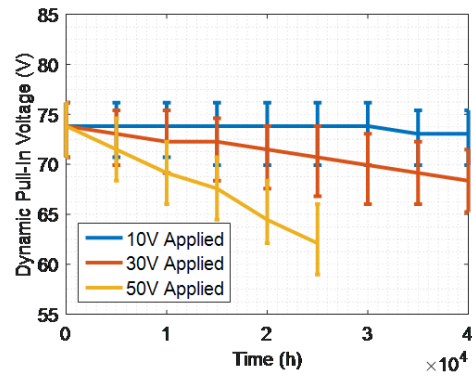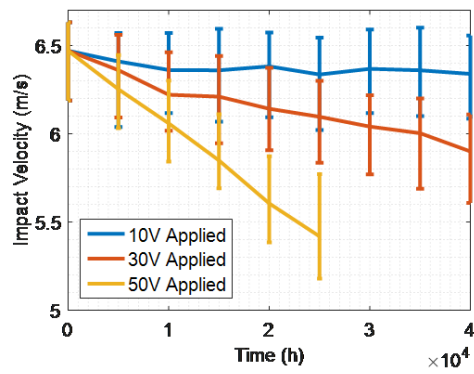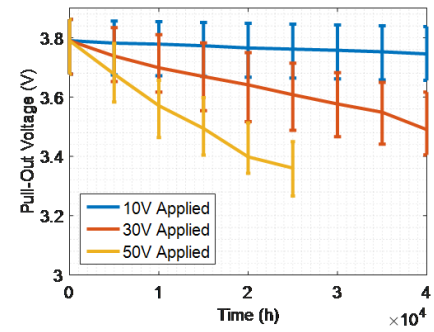
Figure 2.8. Simulation results with error bars representing the median 10% of output values are shown for the: (a) Static pull-in voltage, (b) Dynamic pull-in voltage, (c) Impact velocity, and (d) Pull-Out voltage.
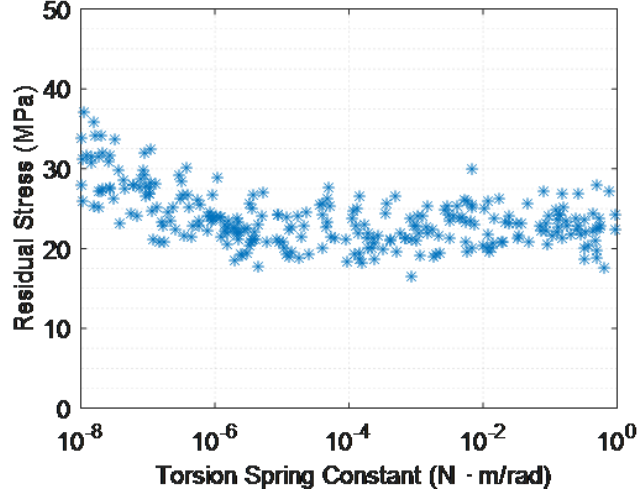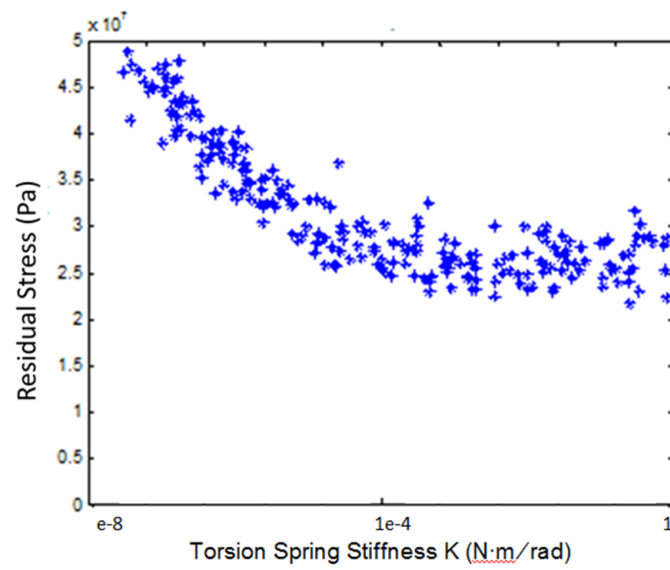
Figure 2.9. Values of residual stress and torsion spring stiffness for which the simulation PIV fits the experimentally measured PIV for one $500\mu$m beam.

# 3. VARIATION OF GRAIN SIZE ACROSS THE THICKNESS OF A BEAM AND ITS EFFECT ON THE CREEP RESPONSE

As studied in the last chapter, creep deformation is a reliability issue for RF-MEMS devices. Residual stresses which remain after fabrication, in combination with stresses developed during operation, produce permanent creep deformation of the membrane. This permanent deformation impacts the actuation voltage [79] and the impact velocity.

Creep is a permanent time-dependent deformation response that occurs at a constant applied load even for stresses below the yield stress [8]. Creep in crystalline materials operates due to one or a combination of processes that occur at the atomic scale, such as dislocation glide, grain boundary sliding, and the diffusive flow of atoms in the lattice and grain boundaries. In nanocrystalline nickel RF-MEMS operated at room temperature, creep deformation occurs due to the diffusion of atoms along grain boundaries [80]. This deformation process is known as Coble creep. The functional form of the Coble creep law has been determined in analytical form from highly idealized representations of grain boundaries [81]. While this assumption makes the model tractable, it limits its applicability to real systems. More sophisticated models not only exhibit dependence on the average grain size, which is evident in the analytical form of the Coble creep law, but also take into account the impact of the grain shape, grain size distribution [82], [83], and grain-boundary properties [84].

Creep in MEMS is measured in a variety of manners. Tensile tests of MEMS devices to obtain creep properties were performed by Wang et al. [4], Yin et al. [17], and Tuck et al. [56]. Indentation tests were performed by Wang et al. [53] and Cao et al. [54]. Tests via membrane bending were performed by Vickers-Kirby et al. [55], Bergers et al. [85], and Hsu and Peroulis [86].

The incorporation of variability and randomness in models of material behavior provides predictions which are not possible with deterministic models and parameters. It also aids in the understanding of the underlying physical processes. For example, knowledge of the variability in grain size distribution is fundamental to the prediction of plastic strain recovery due to creep deformation in nanocrystalline thin films used in MEMS [28], [25], [14].

Plastic strain recovery was recently noted by Mulloni et al [82]. In their article, the dielectric commonly used in a MEMS electrostatically actuated cantilever was replaced with a physical backstop. This substitution eliminated the possibility of dielectric charging, which may be mistaken for creep. The elimination of dielectric charging left creep as their explanation for both the time-dependent plastic strain they found in their experiments as well as the incomplete recovery of the same plastic strain when the electrostatic load was removed. Variation in grain size across the thickness of the device is one explanation for the recovery; upon removal of the electrostatic load, small grains which have only deformed elastically during the extended loading are capable of compressing the large grains which have deformed plastically.

Variability in grain size distributions also affects active deformation mechanisms. Along these lines, Raj and coworkers show that including grain size distributions leads to a gradual transition in creep deformation mechanisms at different strain rates, and that this transition is the result of a gradual change in the stress exponent which is not observed using a non-stochastic model [87], [88].

In this chapter, the effect of the uncertainty of grain size distribution is studied in RF-MEMS undergoing Coble creep during operation. The pull-in voltage is determined by numerical simulations in which the RF-MEMS is actuated for varying periods of time. The grain size variability is implemented by a representation of the membrane that takes into account grain sizes which have been measured at different heights across the membrane thickness.

### 3.1   Model and Computational Approach

The RF-MEMS switch illustrated in Figure 3.1 consists of a fixed-fixed nanocrystalline nickel membrane suspended over an electrode. The geometric and material properties of the switch are shown in Table 3.1. The electrode is coated with a dielectric material to prevent direct contact between the membrane and the electrode. In the ON state the membrane is undeformed, allowing a radio-frequency (RF) signal to pass through freely. In the OFF state, the membrane is deformed toward the electrode as a result of the application of a bias voltage. This deformation increases the capacitance of the switch, prohibiting the passage of a RF signal.
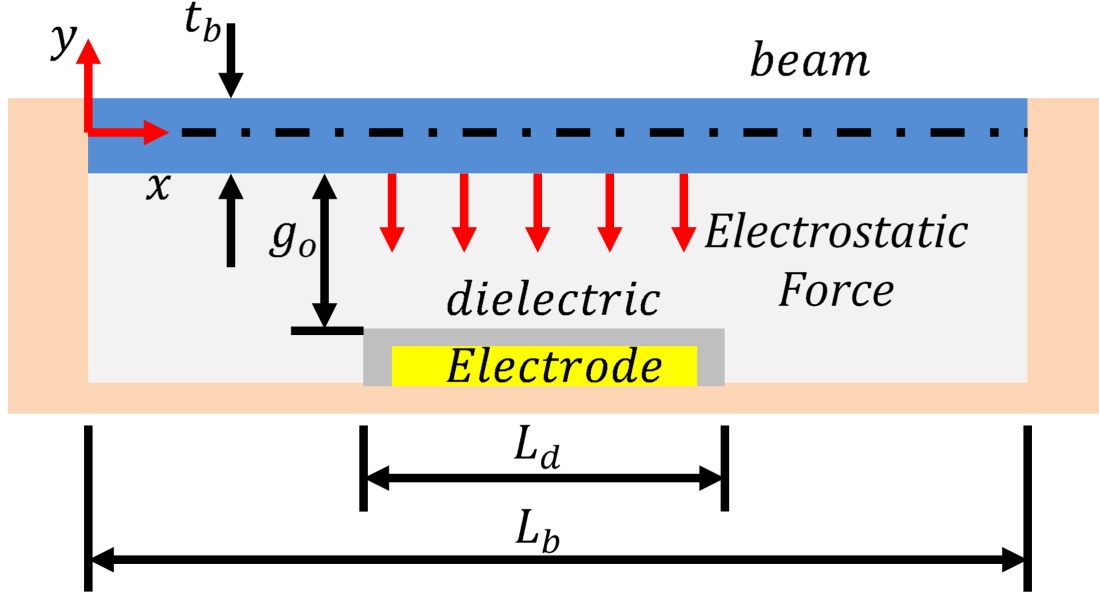


Figure 3.1.  RF MEMS switch under study. The switch is represented as a flat beam suspended over an electrode and a dielectric layer.

The transition from the ON state to the OFF state depends on the electrostatic and restoring forces on the membrane. The electrostatic force on the membrane increases with deflection at a greater rate than the elastic force resisting deformation, with the result that as the applied bias voltage is increased, the electrostatic force eventually overcomes the restoring force and the membrane "snaps through", closing

Table 3.1. Mechanical and Geometric Properties of the RF-MEMS switch used in the simulations with height-dependent grain size.

| Symbol | Quantity | Value |
|---|---|---|
| $L$ | Beam Length | 500 $\mu$m |
| $b$ | Beam Width | 120 $\mu$m |
| $g$ | Initial Gap | 5.00 $\mu$m |
| $h_o$ | Nominal Thickness of the Beam | 2.0$\mu$m |
| $t_d$ | Dielectric Thickness | 0.20 $\mu$m |
| $L_d$ | Dielectric Length | 260 $\mu$m |
| $\rho$ | Beam Density | 8912 $kg/m^3$ |
| $E$ | Young's Modulus | 200 GPa |
| $\sigma_y$ | Yield Stress | 0.7 GPa |
| $\nu$ | Poisson's Ratio | 0.30 |
| $\epsilon_r$ | Relative Permittivity | 7.9 |
| $A$ | Material Creep Coefficient | 782 |

the gap and making contact with the dielectric. This phenomenon is called pull-in, and the voltage at which the membrane makes contact with the dielectric layer is called the pull-in voltage, $V_{PI}$.

### 3.1.1 Electromechanical Response of a RF-MEMS Switch

Stress equilibrium governs the deformation of the switch, and is given by the constitutive relationship

$$\frac{\partial}{\partial t^2}(\rho u_i) - \frac{\partial}{\partial x_j}(\sigma_{ij}) = \rho f_i \tag{3.1}$$

where $\rho$ is the density of the nickel membrane, $u_i$ is the displacement, $\sigma_{ij}$ is the stress tensor, $f_i$ is the external body force, and the indices are $i = 1, 2, 3$ and $j = 1, 2, 3$. The

stress tensor $\sigma_{ij}$ is determined from the elastic strain, and is expressed as a function of the elastic strain tensor $\epsilon_{ij}^E$ in the form

$$\sigma_{ij} = C_{ijkl}\epsilon_{kl}^E \tag{3.2}$$

where $C_{ijkl}$ is the fourth-order material elasticity tensor. The stress is assumed to depend on the elastic strain $\epsilon_{kl}^E$ alone, but there is an additional plastic strain component $\epsilon_{kl}^C$ which is assumed to contribute to the total strain $\epsilon_{kl}^T$ in the manner

$$\epsilon_{ij}^T = \epsilon_{ij}^E + \epsilon_{ij}^C \tag{3.3}$$

The elastic strain is determined from the deformation, but the creep strain term $\epsilon_{kl}^C$ is obtained by time integration of the constitutive expression for the steady-state creep rate [9]:

$$\dot{\epsilon}_{ij}^C = A_c \frac{\sigma_{ij}^d}{\sigma^{vm}} \left(\frac{\sigma^{vm}}{\sigma_y}\right)^1 \tag{3.4}$$

where $\sigma^{vm}$ is the Von Mises stress, $m$ is the creep stress exponent which is $m = 1$ for Coble creep, $\sigma_y$ is the yield stress, and $A_c$ is the creep constant defined by

$$A_c = A \frac{\delta_b D_{bo} e^{\frac{-Q_b}{RT}} \sigma_{yo}}{kT} \left(\frac{b_b}{<d>}\right)^3 \tag{3.5}$$

where $\delta_b D_{b0}$ is the grain boundary diffusion coefficient [9], $Q_b$ is the boundary diffusion activation energy [8], $R$ is the ideal gas constant, $b_b$ is the Burgers vector [8], $<d>$ is the average grain size, $T$ is the absolute temperature, $k$ is the Boltzmann constant, and $\sigma_{y0}$ is the initial yield stress. The coefficient $A$ in Equation 3.5 is a geometrical factor. For nanocrystalline nickel, the values of A found in literature range from 1 to 1000 [4], [17], [89]. A value of $A = 782$ is used in the current simulations. The values for the remaining parameters are shown in Table 3.2.

The system of equations defined by Equations 3.1-3.5 is numerically integrated in an unstructured cell-centered finite volume method framework [48] in which creep strain is implemented as a source term [90]. In order to determine the increment of

Table 3.2.   Further Properties of the RF-MEMS switch used in the simulations with height-dependent grain size.

| Symbol | Quantity | Value |
|---|---|---|
| $\delta_b D_{b0}$ | Grain Boundary Diffusion Coefficient | $3.5 * 10^{-15} m^3/s$ |
| $Q_b$ | Boundary Diffusion Activation Energy | $115 * 10^3 \frac{J}{mol}$ |
| $R$ | Ideal Gas Constant | $8.314 \frac{J}{mol \bullet K}$ |
| $b_b$ | Burgers Vector | $0.25 * 10^{-9} m$ |
| $T$ | Absolute Temperature | $293 K$ |
| $k$ | Boltzmann Constant | $1.38 * 10^{-23} \frac{J}{K}$ |
| $\sigma_{y0}$ | Initial Yield Stress | $0.7 GPa$ |

plastic strain, the creep strain rate in Equation 3.4 is integrated directly with the explicit Euler method at each time step from knowledge of the stress state. This plastic strain increment is added to the total strain, and the time is advanced.

In deriving the relationship between strain rate and stress for diffusional creep, it is commonly assumed that the material consists of grains which are identical in shape and size [81]. It is also commonly assumed that all grain boundaries display equivalent behavior. However, the relative orientation of the grains with respect to the loading axis has a strong influence in the value of A [91]. In addition, Schneibel et al. calculated geometric factors for simple unimodal and bimodal grain structures and found that creep strain rates were capable of varying by over an order of magnitude as a result of the grain distribution, aspect ratios, and orientations [82].

In order to separate the effect of the grain size distribution from the aspect ratios and orientations, the aspect ratios of the grains are here assumed to remain constant through the thickness of the membranes. Therefore, the geometric material parameter A is assumed to be constant throughout the membrane and the variation of the diffusional creep law is related only to the experimentally measured variation in grain size.

In order to quantify the effect of the microstructure of the membrane on the creep and pull-in voltage of the device, numerical simulations of the mechanical response of the RF MEMS switch during and after creep deformation are carried out by means of the finite volume method as implemented in the multi-physics solver MEMOSA [90].

It is noted that the 2D finite volume model used for simulations in this chapter is distinct from the 1D Euler-Bernoulli beam model. The focus in this chapter is on understanding the effect of the microstructure, specifically the grain size distribution, on the film behavior, so the finite volume approximation is utilized to solve the model. The model used is no longer for a beam, but for a solid, which allows for a more natural incorporation of microstructural models as well as a nore natural solution of the multiphysics problems.

### 3.1.2    Microstructural Analysis of the Nickel Membrane

The distribution of grain sizes as measured by the Perouli group at Purdue University are shown in Figure 3.2. The beam was cut, and measurements of grain sizes were made at five heights.

From the measured distributions of grain sizes at five heights, the mean grain sizes at the five heights are taken and plotted against their height in the membrane in Figure 3.3. A power-law fit to the measured grain sizes is also shown.

### 3.2    Pull-In Simulations with Creep

.

### 3.2.1    Microstructural Representation of the Nickel Membrane

Three different models are considered to represent the uncertainty in the microstructure of the polycrystalline nickel membrane.
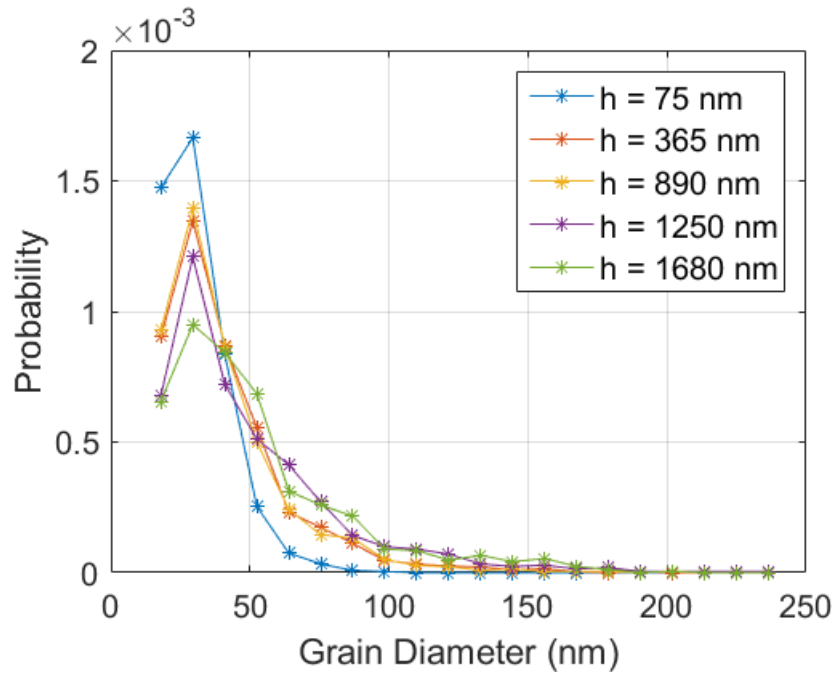
Figure 3.2. Measured probability distributions of grain sizes at five heights in the beam.
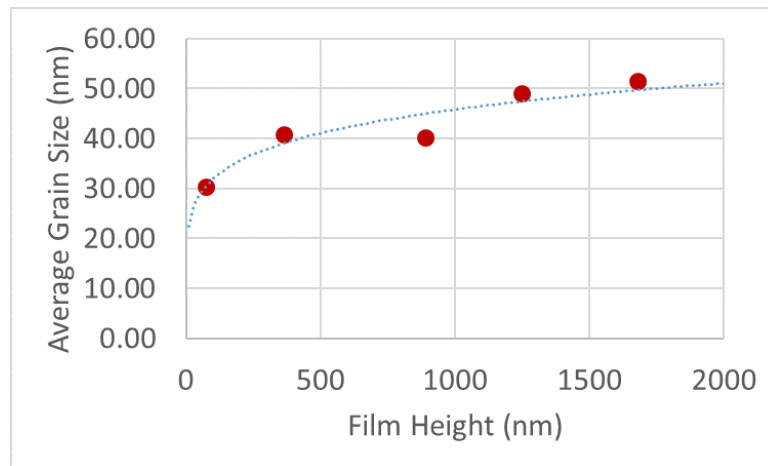


Figure 3.3. Measured average grain sizes at five heights in the beam, with a power-law curve fit.

In model 1, the grain size is assumed homogeneous within the whole beam. To understand the effect of uncertainty in the grain size distribution, different values of

the standard deviation in the grain size are then considered. Model 1.1 is deterministic, with the grain size equal to the global average grain size. In Model 1.2, the grain sizes in the homogeneous membrane are taken as samples from the lognormal distribution fit to the measured grains. In model 1.3, the standard deviation of the average grain size is increased. This is intended to show the effect of an increased deviation in the grain size.

In model 2, the membrane is divided in five layers consistent with the five film heights at which grain size measurements were taken, allotting the height between measurements equally to the measurements above and below. A constant value of the average grain size is assigned to each layer. A Gaussian process model with an exponential fit to the measured average grain sizes is used to determine the average grain size in each layer. In model 2.1, the exact values of the exponential fit at the measured heights is used at the average grain size in the corresponding layers. In model 2.2, the average grain size in each layer is taken from one sample of the gaussian process model with low covariance between grain size and height, with signal strength $s = 0.06$ and length scale $l = 0.5$. In model 2.3 a stricter covariance was chosen, with a signal strength of $s = 0.02$ and a length scale of $l = 1.0$. This resulted in less variability in the average grain size distributions at each height. In Figure 3.4 and Figure 3.5, examples of draws from these two processes are plotted in green. The experimentally determined average grain sizes are shown in red.

Details of the different grain size distributions are shown in Table 3.3.

## 3.3   Results and Discussion

To investigate the effect of the grain size distribution on the pull-in voltage, constant bias voltages of 10V and 20V are applied in the simulation for time periods ranging from $1 * 10^3$ to $4 * 10^3$ hours. After this period of deterioration, the pull-in voltage is measured by increasing the applied DC voltage at a rate of $1V/s$. The
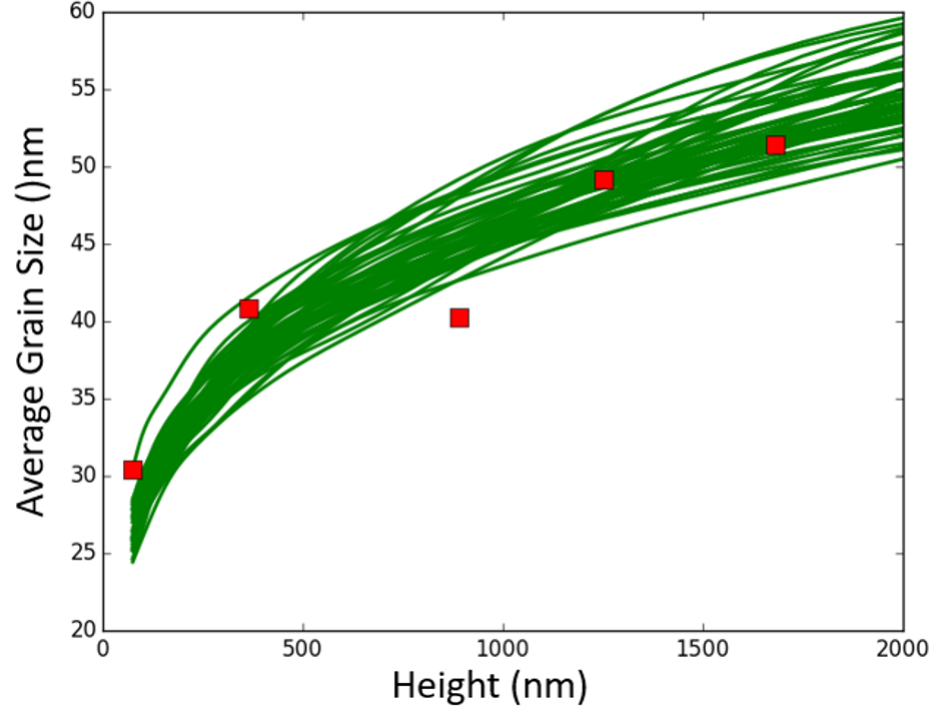
Figure 3.4. Examples of samples from the Gaussian process modelling the grain size distribution, with low covariance given by s=0.06, l=0.5.

pull-in voltage is defined as the voltage at which the gap is reduced to one-tenth of the initial gap.

Figure 3.6 and Figure 3.7 show the predicted pull-in voltage as a function of the time during which the bias voltage is applied. Clearly, increasing the constant bias voltage causes more rapid degradation and a more rapid decrease in the pull-in voltage. The pull-in voltage continues to decrease as the constant bias voltage is applied for greater periods of time. As the time during which creep is active increases, the uncertainty in the PIV value increases.

Figure 3.8 shows a comparison of the results for models 2.1-2.3 with the deterministic model 1.1. It can be seen that when uncertainty is taken into account in this model, the pull-in voltage decreases faster than in either the uniform deterministic model 1.1 or the deterministic model 2.1. As the the uncertainty in the grain size is
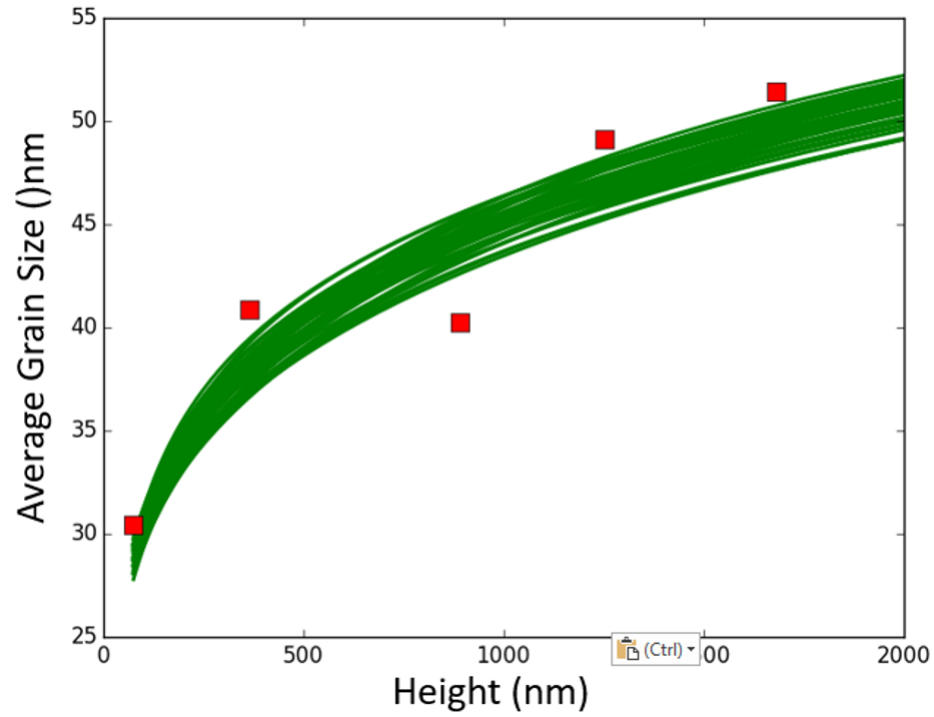
Figure 3.5. Examples of samples from the Gaussian process modelling the grain size distribution, with high covariance given by s=0.02,l=1.0.
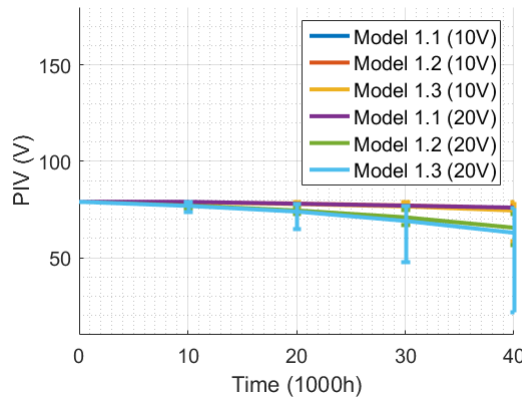


Figure 3.6. Models 1.1 - 1.3:Predicted PIV as a function of time for the beams with grain size varying as a function of height.

increased, the deterioration of the pull-in voltage is more rapid and the uncertainty in the pull-in voltage increases considerably.

Table 3.3.  Input parameters for the two models with grain size vary-
ing as a function of height in the membrane.

| Model | Layer # | Layer Thickness [$\mu$m] | $\mu$ [nm] | $\sigma$ [nm] |
|---|---|---|---|---|
| 1.1 | 1 | 2.000 | 3.785 | 0.0 |
| 1.2 | 1 | 2.000 | 3.780 | 0.1 |
| 1.3 | 1 | 2.000 | 3.765 | 0.2 |
| 2.1 | 1 | 0.220 | 3.354 | 0.0 |
| | 2 | 0.408 | 3.587 | 0.0 |
| | 3 | 0.443 | 3.574 | 0.0 |
| | 4 | 0.395 | 3.728 | 0.0 |
| | 5 | 0.535 | 3.780 | 0.0 |
| 2.2 | 1 | 0.220 | - | - |
| | 2 | 0.408 | - | - |
| | 3 | 0.443 | - | - |
| | 4 | 0.395 | - | - |
| | 5 | 0.535 | - | - |
| 2.3 | 1 | 0.220 | - | - |
| | 2 | 0.408 | - | - |
| | 3 | 0.443 | - | - |
| | 4 | 0.395 | - | - |
| | 5 | 0.535 | - | - |

Contours of the effective von Mises stress for model 1.1 and model 2.1 under the applied voltage of 10 volts are shown in Figure 3.9 and Figure 3.10. The scales in these plots differ. The use of multiple layers with differing grain sizes is seen to lead to greater asymmetry in the stress profile as well as greater concentrations of stress.
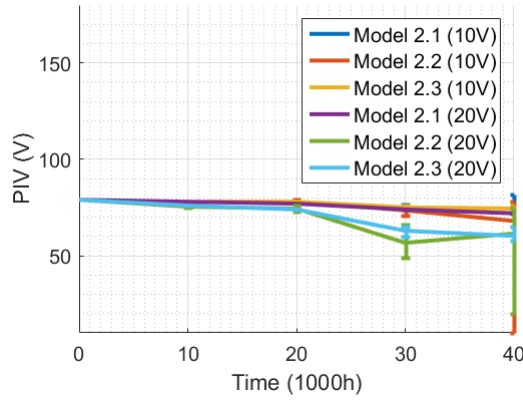
Figure 3.7. Models 2.1 - 2.3: Predicted PIV as a function of time for the beams with grain size varying as a function of height.
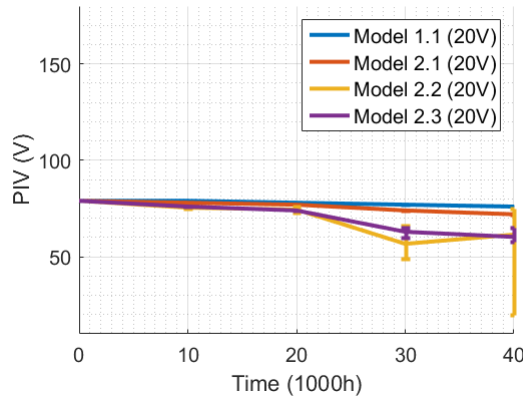


Figure 3.8. Predicted PIV after 40,000 hours of applied bias voltage 10V, as the grain size distribution uncertainty increases, for the model with grain size varying as a function of height.

## 3.4 Conclusions

The influence of grain size distributions in a thin film has been demonstrated with a finite-volume model which incorporated Coble creep. The inclusion of multiple layers with grain sizes representative of the grain size experimentally seen in those layers is seen to increase the simulated creep rate, as compared to models in which the beam is treated as one homogeneous layer with a uniform grain size. The inclusion of
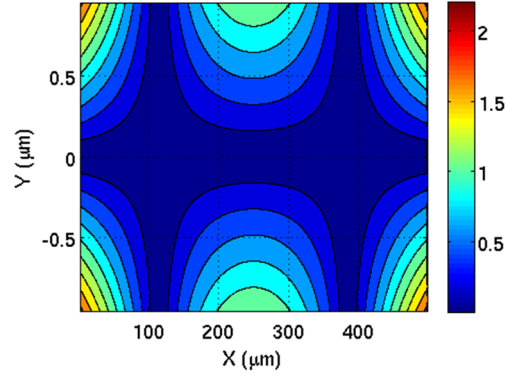
Figure 3.9. Plots of Von Mises stress contours in Model 1.1 at 40000 hours.
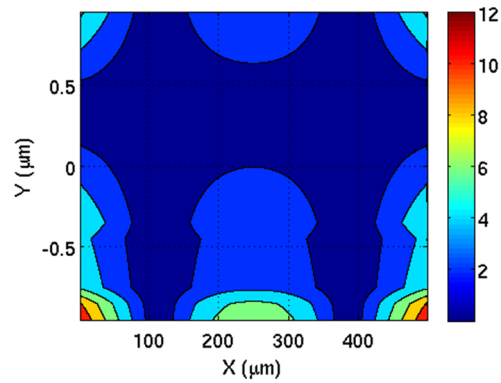


Figure 3.10. Plots of Von Mises stress contours in Model 2.1 at 40000 hours. The bottom layer of grains is particularly evident in the asymmetry of the stress profile.

uncertainty in the grain size distribution resulted in distributions of the PIV which show increasing variability with time and with greater loads. The distribution of grains in multiple layers is seen to result in an asymmetric stress profile in which the layer with the smallest grains experiences greater plastic strain. This distribution of stress may result in plastic strain recovery when the load is removed.

# 4. FILM THICKNESS VARIABILITY EFFECTS ON FIXED-FIXED RF-MEMS CAPACITORS

Thickness variations occur in the suspended electrode films of fixed-fixed RF-MEMS capacitive switches, as discussed in, e.g., [92]. Thickness uniformity is more frequently discussed on the scale of the wafer on which devices are fabricated, as in reference [93], in which a 5% variation of film thickness is seen across a wafer, suggesting a smaller intra-device variation of thickness. Device-to-device variations in film thickness are seen among devices fabricated on the same wafer, as in references [94] and [61], although the film thickness is assumed uniform within each device in both of these works.

The effects that these variations in thickness within a device have on the natural frequencies and pull-in voltages (PIVs) of the switches are studied here by means of finite element simulations in one and three dimensions. Variation of the upper and lower surfaces of the suspended film are considered separately. This separation is used to distinguish the effects of the thickness variation from those of the change in the electrostatic gap resulting from varying the profile of the lower film surface. The profiles of each surface are represented using 1D and 2D Fourier series. The coefficients of these series are varied, and simulations of the modal harmonics and quasi-static electrostatic loading of the resulting films are performed using ANSYS to determine the resulting natural frequencies and PIVs of the films.

Polynomial response surfaces are fit to the PIVs, and probability density functions (PDFs) of the PIVs are generated for assumed uncertainties in the Fourier coefficients using ranges of approximately $\pm 5\%$ in the film thickness across the $400\mu$m film length. These variations in thickness cause standard deviations of approximately 2% in the PIVs and natural frequencies. Variation in thickness across the width of the films is seen to have a smaller impact than variation across their length. In an effort to rapidly

calculate PIVs of switches of variable thickness, these variations across the film width are neglected, leaving only variations in thickness along the length; this permitted the derivation of a 1D equation of motion for the film with variable thickness along its length, which is applied to further explore the sensitivity to the film thickness.

## 4.1 Introduction

Chemical vapor deposition (CVD), magnetron sputtering, molecular beam epitaxy, and electron beam deposition are among the wide variety of thin film deposition techniques used to manufacture RF-MEMS. Because the thickness and uniformity of thin films is frequently a critical factor in their application, much research has been dedicated to measuring and improving the uniformity of deposited thin films [95], [96].

Thin film uniformity remains a critical parameter in MEMS fabrication. Some measured values of non-uniformity are mentioned: In reference [97], a non-uniformity of 5% across a 100-mm wafer of 30-$\mu$m thick electrodeposited copper, as measured by spectroscopic ellipsometry and achieved by means of a current thief, is described as excellent. A uniformity of 1.9% is achieved for electrodeposited copper films of about 1-$\mu m$ thickness across 200-mm wafers in reference [98] and standard electroplating is described in that reference as having uniformity of "at best within 5.5%". The heights of deposited nickel through-metal vias (TMVs) across a 4-in wafer are seen to vary within 3±0.25-$\mu$m, or about 8%, and separately, the heights of nickel TMVs in a 160x220 array of MEMS are seen to vary within 4±0.5-$\mu$m, or about 11%, as measured by scanning electron microscope (SEM) [99]. In [100] the authors were able to reduce the thickness non-uniformity to around 4% for a copper film with a thickness of 46$\mu$m, and they cite [101], in which approximately 11% non-uniformity was achieved for a deposited 10-$\mu$m-thick nickel film.

Measurements of film thickness within or across single devices are less frequently found. Measurements of the thickness of a single RF-MEMS device at multiple locations are shown in Figure 4.1. These measurements were performed and provided by

Dr. Nurul Shaik. In this figure, an overhead view of a single device is shown. Dr. Shaik made two cuts with a focused ion beam in order to remove the center portion of the suspended film and estimated the thickness of the film at multiple locations along these cuts, as seen in Figure 4.1, by examining the cuts via scanning electron microscope. Additional measurements along the long edges of the film showed sub-micron thicknesses, but these are considered to have a negligible impact on the effective width of the film. The thickness of the film in the locations shown range from $2.88\mu m$ to $5.27\mu m$ across the length and width of the interior of the suspended film [102].



Figure 4.1. Measurements from Dr. Nurul Shaik of the thickness of a single RF-MEMS device at multiple locations across two cuts [102].

## 4.2   3D Finite Element Model

The finite element method, as executed by ANSYS, is used to model the moving electrode of a fixed-fixed radio-frequency microelectromechanical switch as well as the electric potential in the region below the film. The material properties used are representative of a nickel film and an air gap. Two-dimensional Fourier coefficients are used to systematically vary the profile of the film without changing its average thickness.

To estimate the natural frequencies of each film, a modal analysis is also performed in ANSYS.

To estimate the PIV, a quasi-static simulation is performed for each film. In this simulation, the electric potential at the base of the gap below the film is increased in increments until the simulation is unable to converge due to the inherent instability near contact. The voltage at which the simulation fails to converge is treated as the PIV, i.e. the voltage at which the electrostatic force upon the film overcomes the mechanical restoring forces of the deformed film, causing the film to snap down toward the electrode. The error due to this approximation is in the range of the voltage increment size.

Numerical stability is used as an indicator of the PIV; see, for example, reference [57]. As the applied voltage is increased in steps, though, it is possible for numerical instability to occur prior to the PIV. This is particularly of some concern for the thin, flat elements used to model the film in this 3D model. This phenomenon of numerical instability prior to the expected PIV was not observed in simulations of films with uniform or non-uniform thickness; as tolerances on the force and electrostatic potential were decreased, or as the voltage increment was reduced, the estimated PIV was not seen to vary by more than the voltage increment and remained in reasonable agreement with estimations of the PIV from the 1D Euler-Bernoulli beam model previously discussed.

To provide further validation, additional estimations of the PIV were made by adjusting the device length, thickness, and gap size in the example electrostatic-structural analysis of a MEMS device presented in the ANSYS documentation [103]. This example is a reduced-order model in which the displacement of the suspended film is described as a weighted sum of its calculated linear elastic mode shapes. The displacement of the film under a test load is used to select a small number of important mode shapes. The strain energy of the system is then calculated for a variety of applied displacements, and polynomial functions of the strain energy are fit to these samples. Finally, these polynomial strain energy functions are applied to estimate the displacement of the film under applied electrostatic loading up to pull-in. These approximations serve to reduce the computational complexity of modeling the device.

The PIVs estimated in this manner were in reasonable agreement with both the full 3D finite element simulations and the 1D simulations.

Additional error in the estimated PIV is introduced by the inaccuracies inherent in modeling the mechanics and electric potential using the finite element method; by the chosen tolerances on the force and electric potential as used to determine convergence of the simulation; and by neglecting the medium surrounding the film on its sides and top. It is noted that this assumption, i.e. neglecting the surrounding medium, neglects the fringing electric field in this volume, thereby decreasing the estimated capacitance and increasing the estimated PIV.

### 4.2.1 Switch Description

A schematic of the switch under consideration is shown in Figure 4.2. The film length $L$, electrode length $L_e$, film width $b$, nominal film thickness $h$, dielectric thickness $t_d$, and initial gap $g$ are illustrated.
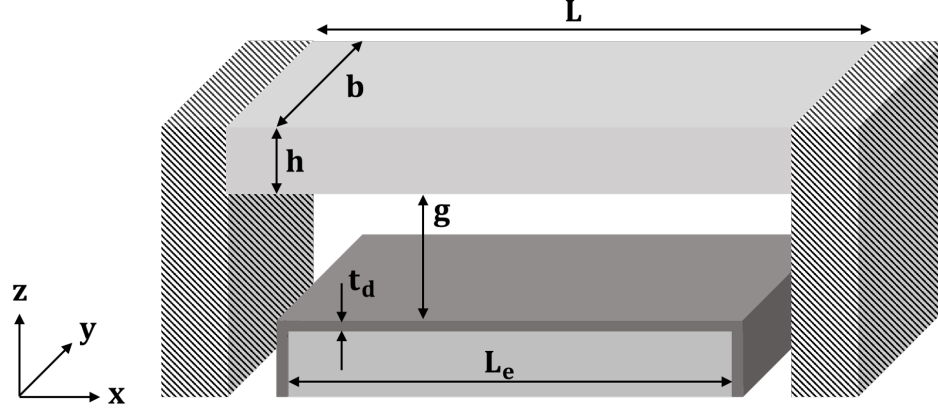


Figure 4.2. Illustration of Nominal Switch Properties.

The switch is composed of a metal film, fixed on either side, suspended above an electrode. When a bias voltage is applied between the film and the electrode, an electrostatic force is generated, attracting the film toward the electrode. The

dielectric material between the suspended film and the electrode serves to prevent contact between film and electrode as well as to increase the capacitance of the device.

The nominal properties of the modeled RF-MEMS switch illustrated in Figure 4.2 are shown in Table 4.1. In order to reduce the complexity of the model and isolate the effects of the thickness non-uniformity the dielectric thickness is set to zero, so that the dielectric layer covering the electrode is not considered.

Table 4.1. Nominal Switch Parameters.

| Symbol | Quantity | Value |
|---:|---|---|
| $L$ | Film Length | 400 $\mu$m |
| $L_e$ | Electrode Length | 400 $\mu$m |
| $b$ | Film Width | 100 $\mu$m |
| $h$ | Nominal Film Thickness | 3.0 $\mu$m |
| $\nu$ | Film Poisson's Ratio | 0.30 |
| $E$ | FilmYoung's Modulus | 200 GPa |
| $g$ | Initial Air Gap | 3.0 $\mu$m |
| $t_d$ | Dielectric Thickness | 0.0 $nm$ |

### 4.2.2   Origins of Film Non-Uniformity

Deviation from planarity in the film profile does not by itself indicate thickness non-uniformity, as non-planarity may be the result of multiple factors. Several of these factors are discussed below.

A film's deviation from flatness may be the result of a stress-free initial curvature. A nonplanar film with uniform thickness and stress-free initial curvature may be generated if a film of uniform thickness is deposited on a curved surface. When the material beneath the film is removed, a stress-free curved film of uniform thickness remains.

The deviation from a flat surface may be the result of curvature from residual stresses, where the film bows up or down as the result of some combination of compressive or tensile stresses. Compressive residual stresses in the direction of the film's length may increase the PIV if they cause the film to buckle away from the electrode, as the greater distance from the electrode reduces the electrostatic force for a given applied bias voltage. If the film buckles toward the electrode or does not buckle, the PIV will generally be reduced by compressive residual stresses. In the case of tensile stresses, the film is likely to exhibit an increased stiffness, meaning a greater resistance to deflection, which results in an increased PIV.

The deviation from a flat surface may be the result of surface roughness due to the crystallographic growth of the film. As polycrystalline films are deposited, some crystallographic orientations result in a faster rate of growth normal to the substrate surface. As the film thickness grows, the combination of crystallographic orientations and resulting growth rates will result in an uneven surface. This surface roughness on the scale of individual grains is differentiated from the waviness and considered in this chapter, where the thickness of the film surface varies along its length at a larger length scale.

The deviation from a flat surface may be the result of the deposition method. Several film deposition methods are known to deposit films with some inherent randomness in the deposited thickness at a length scale smaller than the device, or to deposit films with a pattern of film thickness on a larger length scale. Depending on the scale of the variability in the deposited film thickness, the film thickness may vary within individual devices or it may vary from device to device.

### 4.2.3 Profile Description

Superpositions of 2D Fourier sine and cosine functions are used to model the shape of the top and the bottom surfaces of the film. Considering the top of the film first,

the change $dH^{Top}(x, y)$ in the total thickness of the film at a given location $(x, y)$ resulting from the top profile is given by

$$
\begin{aligned}
dH^{Top} =& \Sigma_{j=0}^{n} \Sigma_{k=0}^{n} [C_{jk}^{top} cos((j)\frac{2\pi x}{L} + (k)\frac{2\pi y}{b})] \\
& + \Sigma_{j=0}^{n} \Sigma_{k=0}^{n} [S_{jk}^{top} sin((j)\frac{2\pi x}{L} + (k)\frac{2\pi y}{b})]
\end{aligned}
\tag{4.1}
$$

where $j$ and $k$ are indices which range from 0 up to the maximum number $n$ of sine or cosine coefficients considered in each direction, $C_{jk}^{top}$ are the cosine coefficients in $\mu m$ and $S_{jk}^{top}$ are the sine coefficients in $\mu m$ describing the height of the top surface of the film above or below its nominal location, $x$ is the coordinate along the length $L$ of the film, and $y$ is the coordinate across the width $b$ of the film.

The four cosinusoidal profiles whose coefficients are $C_{00}^{top}$, $C_{10}^{top}$, $C_{01}^{top}$, and $C_{11}^{top}$ are illustrated in Figure 4.3. As the top surface is modified according to these profiles, the mean value of the whole film's thickness does not change in any case except when $C_{00}^{top}$ is nonzero. Adjusting $C_{00}^{top}$ causes a uniform increase (or decrease) of the thickness. This section is concerned with nonuniform profiles, so $C_{00}^{top}$ is not considered in this chapter. Similarly, the sinusoidal coefficient $S_{00}^{top}$ causes no change in the thickness and is therefore ignored. The same arguments will apply for the first sine and the first cosine coefficients on the bottom surface, $S_{00}^{bot}$ and $C_{00}^{bot}$ on the bottom surface, and these are also neglected.

The bottom surface of the moving electrode may, in the same manner as the top surface, be modeled as a superposition of 2D Fourier sine and cosine functions. The change in thickness $dH^{Bot}$ resulting from this modification may then be written as

$$
\begin{aligned}
dH^{Bot} = & - \Sigma_{j=0}^{n} \Sigma_{k=0}^{n} [C_{jk}^{bot} cos((j)\frac{2\pi x}{L} + (k)\frac{2\pi y}{b})] \\
& - \Sigma_{j=0}^{n} \Sigma_{k=0}^{n} [S_{jk}^{bot} sin((j)\frac{2\pi x}{L} + (k)\frac{2\pi y}{b})]
\end{aligned}
\tag{4.2}
$$

where $C_{jk}^{bot}$ and $S_{jk}^{bot}$ are the cosine and sine coefficients for the bottom surface, respectively.
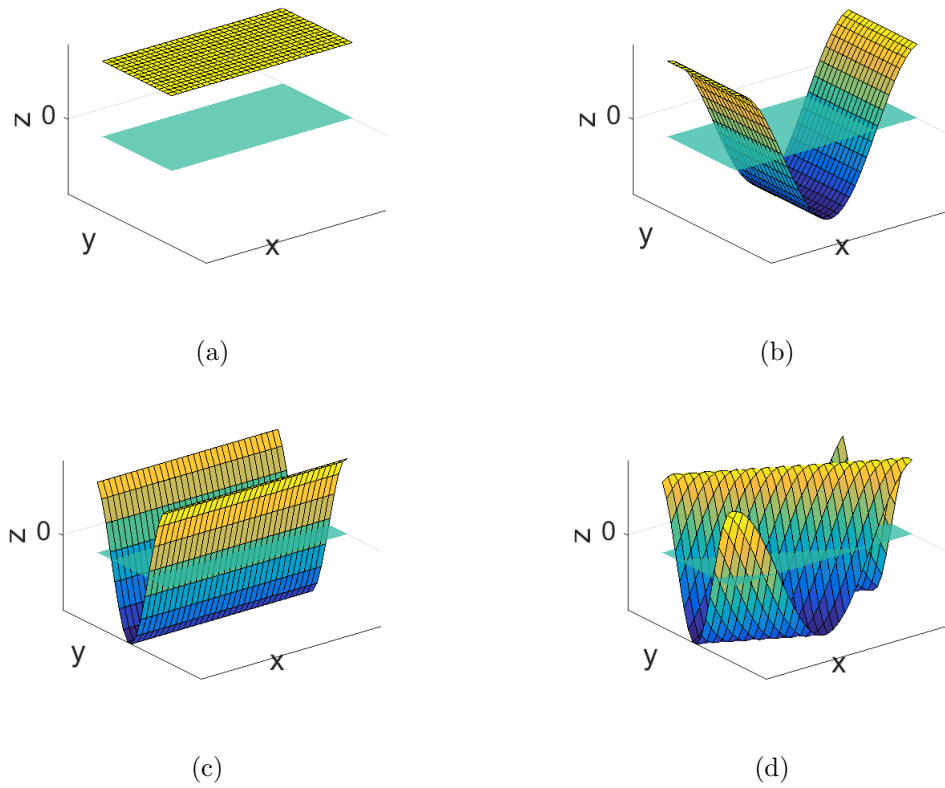
Figure 4.3. Illustration of four 2D Fourier cosinusoidal profiles: (a) the coefficient $C_{00}$, a uniform change in thickness, which is not applied here; (b) the coefficient $C_{10}$, varying the thickness along the length of the film; (c) the coefficient $C_{01}$, varying the thickness across the width of the film; and (d) the coefficient $C_{11}$, varying the thickness across both the width and length of the film. The $z = 0$ surface is also shown. The length, width, and profile depth are not to scale.

Simultaneous variation of the top and bottom profiles may then be described with superpositions of these Fourier sine and cosine functions on the top and bottom surfaces, so that the total change $dH$ in the film thickness at any location $(x, y)$ will be described as

$$
\begin{aligned}
dH = {}& \Sigma_{j=0}^{n}\Sigma_{k=0}^{n}[C_{jk}^{top}cos((j)\frac{2\pi x}{L} + (k)\frac{2\pi y}{b})] \\
& + \Sigma_{j=0}^{n}\Sigma_{k=0}^{n}[S_{jk}^{top}sin((j)\frac{2\pi x}{L} + (k)\frac{2\pi y}{b})] \\
& - \Sigma_{j=0}^{n}\Sigma_{k=0}^{n}[C_{jk}^{bot}cos((j)\frac{2\pi x}{L} + (k)\frac{2\pi y}{b})] \\
& - \Sigma_{j=0}^{n}\Sigma_{k=0}^{n}[S_{jk}^{bot}sin((j)\frac{2\pi x}{L} + (k)\frac{2\pi y}{b})]
\end{aligned}
\tag{4.3}
$$

It is noted that Equation 4.3 describes the change in thickness of the film from its mean value at any location (x,y) but that the mean thickness of the whole film remains unchanged; that is, integrating the changes in thickness $dH$ across the width and length will result in no change in the volume of the film. It is further noted that Equation 4.3 does not describe the location of the film centerline. That is, a film may have a uniform thickness $dH = 0$ but may yet have a stress-free initial displacement. For example, applying an identical sinusoidal profile $C_{10}^{top} = C_{10}^{bot}$ on the top and bottom surfaces results in a film with uniform thickness but a sinusoidal initial curvature. The descriptor "stress-free" is used again here to differentiate a film which is manufactured with some innate curvature from a film which develops curvature absent of loading due to tensile or compressive residual stresses, stress gradients, buckling, dielectric charging, or plastic deformation due to, e.g., creep or fatigue.

### 4.2.4  Mesh Convergence and Verification of 3D Model

The deformation of the film under electrostatic loading is simulated, and the resulting stresses and displacements are determined, using the finite element method as implemented in ANSYS. The mesh used in ANSYS is studied to determine a suitable mesh size and element aspect ratio. The voltage-displacement curve of a single switch with the nominal properties shown in Table 4.1 is calculated by the quasi-static application of a bias voltage in increments of $\Delta V = 1V$.

The element size along the thickness is determined by dividing the film into eight equal layers, which is found to be sufficient. When the film thickness is later varied, maintaining this constant number of elements across the thickness requires that the element sizing across the thickness vary with the film thickness. The element sizing across the width and length are made increasingly finer. The discretization of the air gap follows the discretication of the width and length, with one element across the height of the gap.

The differences in the vertical displacement $d$ of the bottom surface of the film at an applied voltage near the PIV for each of the $M$ meshes are used to determine the convergence. Because the meshes differ and do not share nodes at predetermined locations, it is necessary to interpolate displacement of the bottom surface at predetermined locations. The $N$ points at which the displacement is calculated are regularly distributed across the bottom surface with a spacing of $10\mu m$. The root mean square error (RMSE) is used to determine the convergence and is calculated from the formula shown in Equation 4.4.

$$RMSE = \sqrt{\frac{\Sigma_{i=1}^{i=N}(d_i - d_i^F)^2}{N}} \tag{4.4}$$

where $RMSE$ is the calculated error in meters for the chosen mesh, $N$ is the total number of points at which the displacement is interpolated, $d_i$ is the vertical displacement of the $i$th interpolated point, and $d_i^F$ is the vertical displacement of the $i$th interpolated point for the finest mesh used.

The interpolated displacement of one film under electrostatic loading is illustrated in Figure 4.4.

The nominal element sizes and calculated PIV for the film for each of the meshes are shown in Table 4.2. These nominal element sizes are approximations in each dimension.

The approximated RMSE for each mesh is shown in Figure 4.5.

The film used in this mesh convergence study is flat, so any error resulting from the discretization of the curves in the non-flat profiles is not represented.
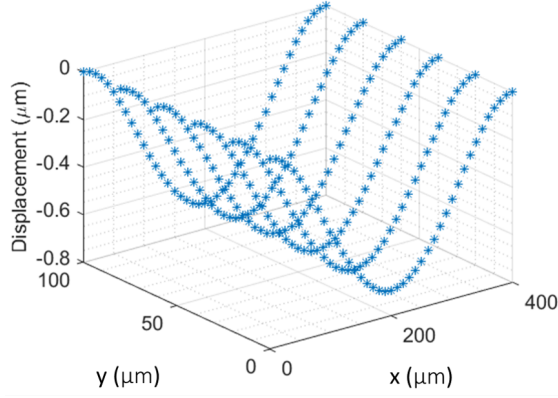
Figure 4.4. Illustration of interpolated displacement of a film under electrostatic loading.

Table 4.2. Nominal Mesh Element Sizes ($\mu m$).

| Mesh # | $\Delta x$ | $\Delta z$ | $\Delta y$ | $PIV$ |
|--------|--------|--------|--------|-------|
| 1 | 100 | 50.0 | 0.375 | 155 $\pm$1V |
| 2 | 50.0 | 50.0 | 0.375 | 100 $\pm$1V |
| 3 | 25.0 | 25.0 | 0.375 | 97 $\pm$1V |
| 4 | 12.5 | 12.5 | 0.375 | 96 $\pm$1V |
| 5 | 6.25 | 6.25 | 0.375 | 96 $\pm$1V |
| 6 | 3.125 | 3.125 | 0.375 | 97 $\pm$1V |

The voltage-displacement curves for the meshes are shown in 4.6. The curves for meshes 2-6 largely overlap. The fourth mesh is considered to be sufficient for determining the PIV and natural frequency of the flat film.

As the voltage is increased, the onset of numerical instability is taken as evidence of pull-in, as in reference [57]. Decreasing the voltage increment and force tolerance negligibly affected the onset of numerical instability. Decreasing the voltage increment showed that 1V increments was sufficient to determine an estimated PIV to within 1V. A voltage which causes the estimated displacement to exceed the gap, or a voltage
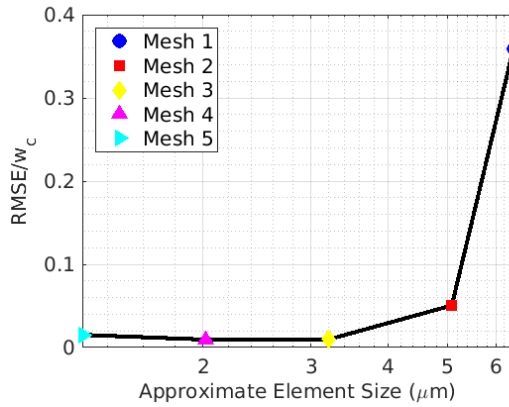
Figure 4.5. Ratio of RMSE to the center displacement at 95V of the finest mesh, for Meshes 1-5.

which results in greater than 20 iterations of the solver, was considered to have caused the device to pull-in. The final voltage which converged above the gap was taken as the PIV for the film.
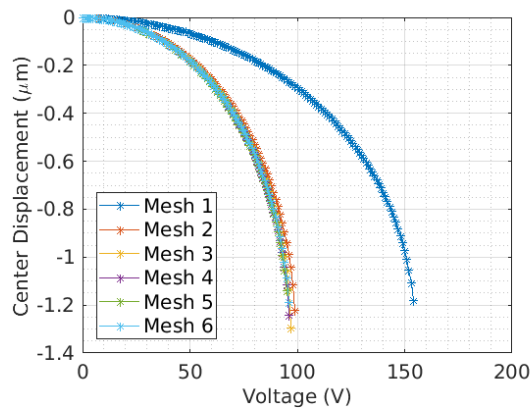


Figure 4.6. Voltage-Displacement curves for six meshes of the flat film.

The mesh of the film with non-uniform thickness is now considered. In order to feasibly represent the curvature of the film's surface, the film's volume is subdivided into a sequence of vertically-oriented triangular prisms. These prisms are then meshed with two or more elements along each side. The mesh is described further in the appendix.

For the case of the film whose thickness non-uniformity profile is represented by a single coefficient $C_{22}^{top} = 0.3 \mu m$ on the top surface, representing a variation of $\pm 10\%$ in the thickness, the volumetric resolution was increased from 9 points/prisms per sine or cosine period to 17 points/prisms per period. For both meshes, the side of each prism was further divided into two second-order elements. The PIV calculated for the finer mesh decreased by 1V. This change was not considered sufficiently large to justify the additional computational expense of the finer mesh. For this reason the discretization of the chosen mesh was set with $\Delta x = 12.5 \mu m$ and $\Delta z = 6.25 \mu m$, meaning 32 volumes across the length and 16 across the width, to assure a minimum of 9 points/prisms in the width- and length-directions per sine or cosine period for all of the profiles considered.

## 4.2.5 Sensitivity of Natural Frequencies and PIV to Variations in Film Thickness on Top Film Surface

The sensitivity of the PIV and first natural frequency to the first several fourier coefficients is first examined by varying each of these coefficients one-at-a-time and applying the finite element model discussed above to estimate the PIV and first natural frequency for the film with the profile described by that coefficient. The top and bottom surfaces are varied separately here, not simultaneously. These PIVs and natural frequencies are compared to the those of the nominal flat film of uniform thickness, so that the effect of each profile on the PIV is measured by the change of the PIV from its "nominal" value.

Additional coefficients varying the thickness of the film along its length with smaller sinusoidal and cosinusoidal periods are included because variation of the thickness in this direction was seen to have the greatest impact on the PIV. Further profiles with linear variations in the film thickness are also considered because these profiles are considered to be realistic but would require a very large number of sine or cosine coefficients.

The sensitivity of the PIV of the device to the first several coefficients is considered, allowing only the profile of the top surface of the film to change.

The top surface of the film described in Table 4.1 is modified using the sine and cosine profiles described in Equation 4.1. Each coefficient is individually adjusted by $0.3\mu m$, which is 10% of the film thickness.

The sensitivity of the PIV and the first natural frequency of the film to the first several cosine coefficients is shown in Table 4.3 and Table 4.4. These results are divided into two tables to show the effect of positive and negative coefficients separately. The sensitivity of the PIV and first natural frequency to the sine coefficients is shown in Table 4.5. The sensitivity of the PIV to three additional profiles is shown in Table 4.6.

Table 4.3. Sensitivity of the PIV and first natural frequency to the positive Cosine Coefficients $C_{jk}^{top}$ on the top surface, as difference from the nominal value. The simulation voltage step size is 0.1V. The nominal device resolves a PIV of 96.1V and natural frequency of 95.2 kHz. Yellow and blue represent +0.3 and -0.3 microns thickness, respectively.
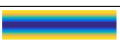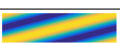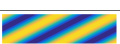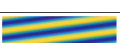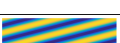
| j | k | $C_{jk}^{top}$ ($\mu$m) | $\Delta PIV(V)$ | $\Delta\omega_n(kHz)$ | Profile |
|---|---|---|---|---|---|
| **1** | **0** | **+0.3** | **6.7** | **6.6** | |
| **2** | **0** | **+0.3** | **7.1** | **6.4** | |
| **3** | **0** | **+0.3** | **1.8** | **1.5** | |
| 4 | 0 | +0.3 | 0.7 | 0.3 | |
| 0 | 1 | +0.3 | 1.0 | 1.1 | |
| 0 | 2 | +0.3 | 1.0 | 1.2 | |
| 1 | 1 | +0.3 | 1.0 | 1.2 | |
| 2 | 1 | +0.3 | 0.9 | 1.0 | |
| 1 | 2 | +0.3 | 0.9 | 1.1 | |
| 2 | 2 | +0.3 | 0.8 | 1.0 | |

Table 4.4. Sensitivity of the PIV and first natural frequency to the negative Cosine Coefficients $C_{jk}^{top}$ on the top surface, as a difference from the nominal value. The simulation voltage step size is 0.1V. The nominal device resolves a PIV of 96.1V and natural frequency of 95.2 kHz. Yellow and blue represent +0.3 and -0.3 microns thickness, respectively.

| j | k | $C_{jk}^{top}$ ($\mu$m) | $\Delta PIV(V)$ | $\Delta\omega_n(kHz)$ | Profile |
|---|---|---|---|---|---|
| **1** | **0** | **- 0.3** | **-5.7** | **-4.9** | |
| **2** | **0** | **- 0.3** | **-7.9** | **-7.4** | |
| **3** | **0** | **- 0.3** | **-4.1** | **-3.9** | |
| **4** | **0** | **- 0.3** | **-2.9** | **-2.6** | |
| 0 | 1 | - 0.3 | 1.0 | 1.2 | |
| 0 | 2 | - 0.3 | 1.0 | 1.1 | |
| 1 | 1 | - 0.3 | 0.8 | 0.8 | |
| 2 | 1 | - 0.3 | 0.5 | 0.6 | |
| 1 | 2 | - 0.3 | 1.0 | 1.1 | |
| 2 | 2 | - 0.3 | 0.9 | 1.1 | |

Because these three profiles seen in Table 4.6 are not expressed in terms of the Fourier functions, they are not used in generating the response surfaces, which are written in terms of the Fourier functions. The sensitivity seen here is underestimated when these profiles are approximated using the response surfaces generated later in this chapter, which suggests that caution should be applied when estimating the PIV and natural frequencies of profiles which are not well-represented by Fourier series.

The greatest sensitivity of the PIV to a profile is seen in the first several cosine profiles $C_{10}$, $C_{20}$, and $C_{30}$. It is noted that these profiles are thinnest where the ends are fixed. Additional coefficients which, like these, vary the profile along the length direction alone were considered, but the sensitivity to these additional profiles was

Table 4.5. Sensitivity of the PIV and first natural frequency to the Sine Coefficients $S_{jk}^{top}$ on the top surface, as a difference from the nominal value. The simulation voltage step size is 0.1V. The nominal device resolves a PIV of 96.1V and natural frequency of 95.2 kHz. Yellow and blue represent +0.3 and -0.3 microns thickness, respectively.

| j | k | $S_{jk}^{top}$ ($\mu$m) | $\Delta PIV(V)$ | $\Delta\omega_n(kHz)$ | Profile |
|---|---|---|---|---|---|
| 1 | 0 | +0.3 | -0.3 | -0.4 |  |
| 2 | 0 | +0.3 | 0.0 | -0.1 |  |
| 3 | 0 | +0.3 | -0.7 | -0.8 |  |
| 4 | 0 | +0.3 | -0.8 | -0.9 |  |
| 0 | 1 | +0.3 | 0.5 | 0.8 |  |
| 0 | 2 | +0.3 | 0.8 | 1.0 |  |
| 1 | 1 | +0.3 | 0.7 | 0.9 |  |
| 2 | 1 | +0.3 | 0.5 | 0.6 |  |
| 1 | 2 | +0.3 | 0.9 | 1.1 |  |
| 2 | 2 | +0.3 | 0.8 | 1.0 |  |

Table 4.6. Sensitivity of three additional profiles on the top surface, as a difference from the nominal value. The simulation voltage step size is 0.1V. The nominal device resolves a PIV of 96.1V and natural frequency of 95.2 kHz. Yellow and blue represent +0.3 and -0.3 microns thickness, respectively.

| j | k | ($\mu$m) | $\Delta PIV(V)$ | $\Delta\omega_n(kHz)$ | Profile |
|---|---|---|---|---|---|
| - | - | +0.3 | -0.3 | -0.2 |  |
| **-** | **-** | **+0.3** | **-12.2** | **-8.6** |  |
| **-** | **-** | **+0.3** | **-6.3** | **-4.5** |  |

small. The sensitivity to other coefficients beyond the ten shown are also presumed to be small in comparison to those shown.

### 4.2.6   Sensitivity to Nonuniformity on Bottom Film Surface

The simulations carried out to estimate the sensitivity of the PIV to variations in the top surface of the film are repeated for the bottom surface. The tabulated results for the positive cosine coefficients, negative cosine coefficients, and sine coefficients, are shown in Table 4.7, Table 4.8, and Table 4.9 respectively.

It is seen from these simulations that the greatest sensitivity of the PIV to the film profile, on either the top or bottom surface, appears to occur in the lower coefficients for the bottom surface, and specifically those which vary the film thickness along the direction of its length; see Table 4.7, Table 4.8, and Table 4.9. A large sensitivity is also seen when the profile of the bottom surface is varied in a linear fashion across the width of the film; see Table 4.10.

As with the ramped profiles seen in Table 4.10, the three profiles seen in Table 4.10 are not expressed in terms of the Fourier functions and are not used in generating the response surfaces. The sensitivity seen here is also underestimated when these profiles are approximated using the response surfaces generated later in this chapter.

The sensitivity of the PIV to the cosine coefficients is again seen to be greater than the sensitivity to the sine coefficients. The thickness of the film at the fixed ends appears to greatly influence the PIV; profiles which are thicker at the fixed ends provide higher PIVs.

### 4.3   Uncertainty Quantification for 3D Model

In this section, estimated uncertainty in the profile of the suspended electrode is propagated from the film profile to the PIV and natural frequency. Uncertainty in the profile is approximated by means of assumed probability density functions for each of the Fourier coefficients representing variation of the top and bottom surfaces

Table 4.7. Sensitivity of the PIV and first natural frequency to the Cosine Coefficients $C_{jk}^{bot}$ on the bottom surface, as difference from the nominal value. The simulation voltage step size is 0.1V. The nominal device resolves a PIV of 96.1V and natural frequency of 95.2 kHz. Yellow and blue represent +0.3 and -0.3 microns thickness, respectively.

| j | k | $C_{jk}^{bot}$ ($\mu$m) | $\Delta PIV(V)$ | $\Delta\omega_n(kHz)$ | Profile |
|---|---|---|---|---|---|
| **1** | **0** | **+0.3** | **-9.0** | **-4.8** |  |
| **2** | **0** | **+0.3** | **-4.9** | **-7.4** |  |
| **3** | **0** | **+0.3** | **-5.5** | **-3.9** |  |
| **4** | **0** | **+0.3** | **-4.0** | **-2.6** |  |
| 0 | 1 | +0.3 | -1.0 | 1.2 |  |
| 0 | 2 | +0.3 | -0.7 | 1.1 |  |
| 1 | 1 | +0.3 | -1.1 | 0.8 |  |
| 2 | 1 | +0.3 | -1.4 | 0.6 |  |
| 1 | 2 | +0.3 | -0.8 | 1.1 |  |
| 2 | 2 | +0.3 | -0.8 | 1.1 |  |

of the suspended electrode. These probability density functions are estimated based on wafer-scale measurements of film nonuniformity found in the literature. These assumed ranges of the Fourier coefficients are heavily sampled, generating a large number of estimates of the PIV and natural frequency. If the space is sufficiently sampled, these estimates may be plotted as a probability density function which will show the likelihood of obtaining a particular PIV or natural frequency for the chosen range of uncertainty in the profile.

In order to avoid the computational expense of running a full 3D finite element simulation for each sample during this sampling, surrogate models for the PIV and natural frequency are created and are heavily sampled in place of the full simulations. The surrogate model chosen here is a polynomial response surface.

Table 4.8. Sensitivity of the PIV and first natural frequency to the negative Cosine Coefficients $C_{jk}^{bot}$ on the bottom surface, as a difference from the nominal value. The simulation voltage step size is 0.1V. The nominal device resolves a PIV of 96.1V and natural frequency of 95.2 kHz. Yellow and blue represent +0.3 and -0.3 microns thickness, respectively.

| j | k | $C_{jk}^{bot}$ ($\mu$m) | $\Delta PIV(V)$ | $\Delta \omega_n(kHz)$ | Profile |
|---|---|---|---|---|---|
| **1** | **0** | **- 0.3** | **9.0** | **6.5** |  |
| **2** | **0** | **- 0.3** | **1.1** | **6.5** |  |
| **3** | **0** | **- 0.3** | **0.5** | **1.6** |  |
| 4 | 0 | - 0.3 | -1.3 | 0.3 |  |
| 0 | 1 | - 0.3 | -0.7 | 1.1 |  |
| 0 | 2 | - 0.3 | -0.8 | 1.2 |  |
| 1 | 1 | - 0.3 | -0.9 | 1.2 |  |
| 2 | 1 | - 0.3 | -1.0 | 1.0 |  |
| 1 | 2 | - 0.3 | -0.8 | 1.1 |  |
| 2 | 2 | - 0.3 | -1.0 | 1.0 |  |

The response surfaces generated for the PIV and for the natural frequency are generated by means of the following procedure. First, a number of full 3D simulations sufficient to fit a polynomial of degree one are run. The polynomial response surface is fit by means of a least-squared error curve-fit in Matlab. A number of full 3D simulations sufficient to generate a polynomial fit one degree higher are then run. The lower-degree response surface is applied to estimate the results obtained in the higher-degree sampling. If the error is sufficiently small, the response surface is accepted. If the error is unacceptably large, the polynomial degree is increased and the procedure is repeated. In this manner, a polynomial response surface of degree two for the PIV is obtained and found to be sufficient, and similarly a polynomial response surface of degree two is found to be sufficient for the natural frequency.

Table 4.9. Sensitivity of the PIV and first natural frequency to the Sine Coefficients $S_{jk}^{bot}$ on the bottom surface, as a difference from the nominal value. The simulation voltage step size is 0.1V. The nominal device resolves a PIV of 96.1V and natural frequency of 95.2 kHz. Yellow and blue represent +0.3 and -0.3 microns thickness, respectively.
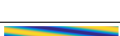
| j | k | $S_{jk}^{bot}$ ($\mu$m) | $\Delta PIV(V)$ | $\Delta\omega_n(kHz)$ | Profile |
|---|---|---|---|---|---|
| **1** | **0** | **+0.3** | **-1.4** | **-0.3** | |
| **2** | **0** | **+0.3** | **-1.9** | **-0.1** | |
| **3** | **0** | **+0.3** | **-2.2** | **-0.8** | |
| **4** | **0** | **+0.3** | **-2.5** | **-0.9** | |
| 0 | 1 | +0.3 | -1.1 | 0.8 | |
| 0 | 2 | +0.3 | -0.8 | 1.0 | |
| 1 | 1 | +0.3 | -1.3 | 0.9 | |
| 2 | 1 | +0.3 | -1.3 | 0.6 | |
| 1 | 2 | +0.3 | -0.9 | 1.1 | |
| 2 | 2 | +0.3 | -0.9 | 1.0 | |

Table 4.10. Sensitivity of three additional profiles on the bottom surface, as a difference from the nominal value. The simulation voltage step size is 0.1V. The nominal device resolves a PIV of 96.1V and natural frequency of 95.2 kHz. Yellow and blue represent +0.3 and -0.3 microns thickness, respectively.

| j | k | ($\mu$m) | $\Delta PIV_{BOT}(V)$ | $\Delta\omega_n(kHz)$ | Profile |
|---|---|---|---|---|---|
| - | - | +0.3 | -0.2 | -0.2 | |
| **-** | **-** | **+0.3** | **-4.8** | **9.5** | |
| **-** | **-** | **+0.3** | **-1.9** | **4.6** | |

The following subsections step through the generation of the response surfaces for the PIV and natural frequency and their application in propagating the estimated uncertainty in the film thickness.

### 4.3.1  Response Surface Generation

A single simulation with a chosen set of input parameters yields a single, deterministic result. If each input parameter is instead assigned a probability distribution function, e.g. a uniform distribution or a normal distribution, then the output quantities of interest of the system (e.g. the PIV and natural frequency) may be described with an as-yet unknown probability distribution function. It is possible to estimate this output PDF with generally increasing accuracy by sensibly sampling the PDFs of the inputs and running a simulation for each sample; as the number of samples and simulations increases, the histogram of the output samples approximates the true output PDF with generally increasing accuracy.

As the number of samples and full 3D simulations required to reasonably approximate these output PDFs is computationally prohibitively expensive, a response surface is fitted to a smaller number of samples of the input space. This response surface is sampled using a large number of samples of the input parameters, and the values generated from the response surface are used (in place of full simulations) to generate the PDF of the output quantities of interest (the PIV and natural frequency).

Two first-order polynomial response surfaces were first generated from the results of the sensitivity analysis above, considering only the 40 simulations with positive values of the Fourier coefficients, in addition to the nominal simulation. The response surface, then, required 41 simulations and is expressed in terms of the 40 sine and cosine profiles. The 40 sine and cosine profiles are those shown in Table 4.3, Table 4.5, Table 4.7, and Table 4.9. The linearly-ramped profiles in Table 4.6 and Table 4.10 are not included here because they were not expressed in terms of the Fourier functions used in generating the response surfaces. The simulations with negative coefficients in

Table 4.4 and Table 4.8 are neglected here for simplicity but are incorporated in the next iteration of response surface generation. The two response surfaces generated in this polynomial curve fit provide estimates of the PIV and the natural frequency, respectively, as functions of the 40 chosen Fourier coefficients.

Results from an additional 880 simulations were applied in order to test the first-order response surfaces. These 880 simulations are comprised of four sets of 220 simulations. Each set of 220 simulations came from a second-order Smolyak sparse grid sampling of a subsection of the parameter space. The Smolyak sparse grid algorithm, like Latin hypercube sampling, is an efficient method for sampling a parameter space, but it is optimized for a polynomial approximation of the results at the sampled points [78]. The first set of 220 simulations sampled only the cosine profiles on the top surface; the second set of 220 sampled the cosine profiles on the bottom surface; the third set of 220 sampled the sine profiles on the top surface; and the fourth set of 220 sampled only the sine profiles on the bottom surface. The original purpose of these 880 simulations was the generation of four response surfaces, i.e. one for each of sine and cosine profiles on the top and bottom surfaces. This approach was discarded in favor of developing a single unified response surface including all 40 Fourier coefficients, but the simulation results are reused here as a testing data for the first-order response surface. The maximum amplitude for any profile in these 880 additional simulations was adjusted down from the previously-considered $0.3\mu m$ to $0.095\mu m$ to avoid nonphysical configurations, e.g. devices where the two electrodes would be in contact before being loaded. Predictions of the results of these same 880 simulations were generated using the first-order response surface, resulting in root mean square errors (RMSE) of 0.74 volts and 405 hertz for the PIV and the natural frequency, respectively. These 880 predictions are compared to the corresponding simulations in Figure 4.7 and Figure 4.8.

An attempt was made to improve this initial first-order response surface by including the 20 simulations with negative coefficients seen in Tables 4.4 and 4.8. These negative values of the Fourier coefficients are treated as additional parameters. Fur-

Figure 4.7. Comparison of predictions from a first-order polynomial response surface of the PIV to 880 additional simulations. Results are sorted by the simulation PIV.
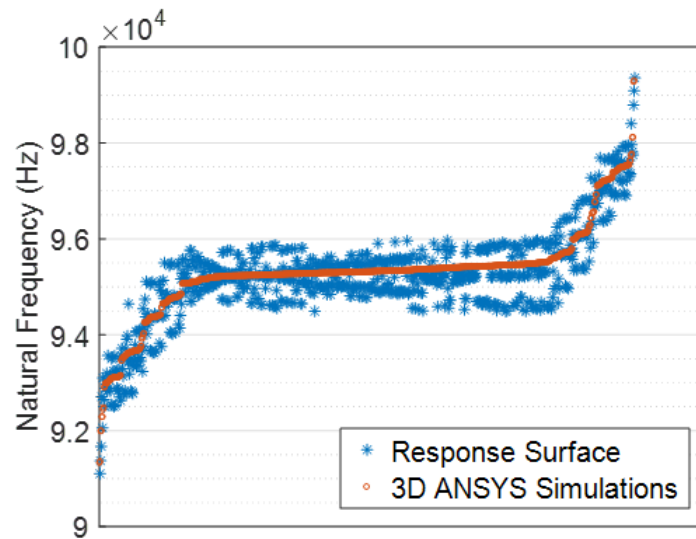


Figure 4.8. Comparison of predictions from a first-order polynomial response surface of the first natural frequency to 880 additional simulations. Results are sorted by the simulation frequency.

thermore, the 20 simulations with sine profiles shown in Tables 4.5 and 4.9 may be reused; in considering the symmetry of the sine profiles, it is evident that the PIV and natural frequency will not change if the sign of the Fourier coefficient is changed. This provides 20 additional simulations and parameters. The response surface is therefore expressed in terms of 80 parameters and, noting the use of symmetry, required only 61 simulations. A first-order polynomial response surface, modified by treating the positive and negative values of the Fourier coefficients in this manner, is thereby generated. Predictions of the results of the 880 simulations previously discussed were generated using this response surface, resulting in root mean square errors (RMSE) of 0.73 volts and 563 hertz for the PIV and the natural frequency, respectively. These 880 predictions are compared to the corresponding simulations in Figure 4.9 and Figure 4.10.
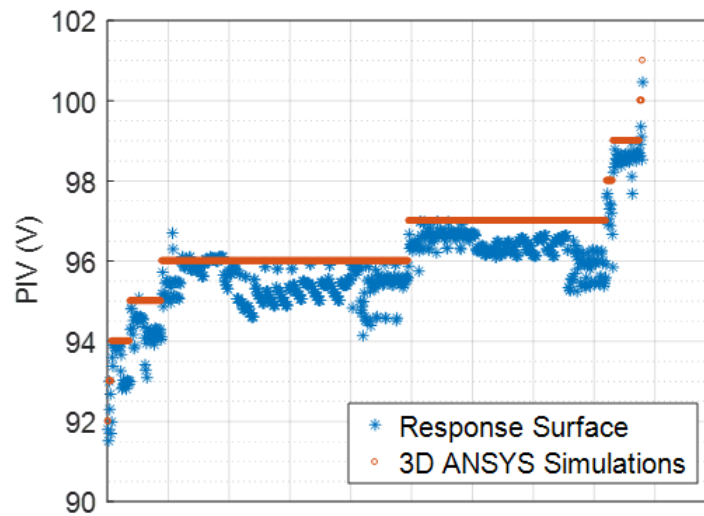


Figure 4.9. Comparison of predictions from a modified first-order polynomial response surface of the PIV to 880 additional simulations. Results are sorted by the simulation PIV.

The improvement from a RMSE of 0.74 volts to 0.73 volts in the PIV is considered negligible. The RMSE of 563 hertz in the natural frequency is worse than the original

Figure 4.10. Comparison of predictions from a modified first-order polynomial response surface of the first natural frequency to 880 additional simulations. Results are sorted by the simulation frequency.

405 hertz, despite a decrease in the mean absolute error. To improve these values, a second-order polynomial response surface is considered.

The 961 simulations already available, consisting of the nominal case, 40 sensitivity results for positive values of the Fourier coefficients, 40 more sensitivity results for the negative values of the coefficients, plus the 880 additional simulations discussed above, were applied to generate a least-squares polynomial fit of degree two for each of the PIV and the natural frequency.

An additional 1300 simulations were run; these provide results with which to test the second-order polynomial response surfaces. This does not constitute a number of simulations sufficient to generate third-order polynomial response surfaces but is considered sufficient for testing the second-order response surfaces. A partial factorial design was applied in generating these samples [104]. A full factorial simulation design for the 40 chosen parameters, allowing each factor to assume a value of $-0.15\mu m$, $0.00\mu m$, or $+0.15\mu m$ would require $3^{40}$ simulations. Such a design would permit the

combinatorial effects of every possible set of parameters to be explicitly found, but the computational power required is prohibitively expensive. The partial factorial design illustrated in Table 4.11 reduces that number of simulations significantly, while still sampling important regions of the design space.

The "X" mark in the first row and third column of Table 4.11 represents 100 simulations generated by linearly superposing each of the 10 $C_{jk}^{top}$ profiles set at $+0.15\mu m$ with each of the 10 $C_{lm}^{bot}$ profiles set at $+0.15\mu m$. The remaining three "X" marks in this row represent a total of 300 additional simulations generated by the linear superpositions of $C_{jk}^{top} = +0.15\mu m$ with $C_{lm}^{bot} = -0.15\mu m$, $S_{lm}^{top} = +0.15\mu m$, and $S_{lm}^{bot} = +0.15\mu m$, respectively. The second, third,fourth, and fifth row add an additional 400, 200, 200, and 100 simulations, for a total of 1300 simulations.

Table 4.11.  Illustration of factorial design applied in generating 1300 simulations for testing of the second-order polynomial response surfaces.

| | $+C_{lm}^{top}$ | $-C_{lm}^{top}$ | $+C_{lm}^{bot}$ | $-C_{lm}^{bot}$ | $+S_{lm}^{top}$ | $+S_{lm}^{bot}$ |
|---|---|---|---|---|---|---|
| $+C_{jk}^{top}$ | | | X | X | X | X |
| $-C_{jk}^{top}$ | | | X | X | X | X |
| $+C_{jk}^{bot}$ | | | | | X | X |
| $-C_{jk}^{bot}$ | | | | | X | X |
| $+S_{jk}^{top}$ | | | | | | X |
| $+S_{jk}^{bot}$ | | | | | | |

Predictions of the results of these 1300 simulations were generated using the second-order response surface, resulting in root mean square errors (RMSE) of 0.38 volts and 387 hertz for the PIV and the natural frequency, respectively. These 1300 predictions are compared to the corresponding simulations in Figure 4.11 and Figure 4.12. Based on the magnitude of this error and on its minor reduction from the ini-

tial RMSE of 0.74 volts and 405 hertz, the response surfaces were considered to have converged and to perform with reasonable accuracy.
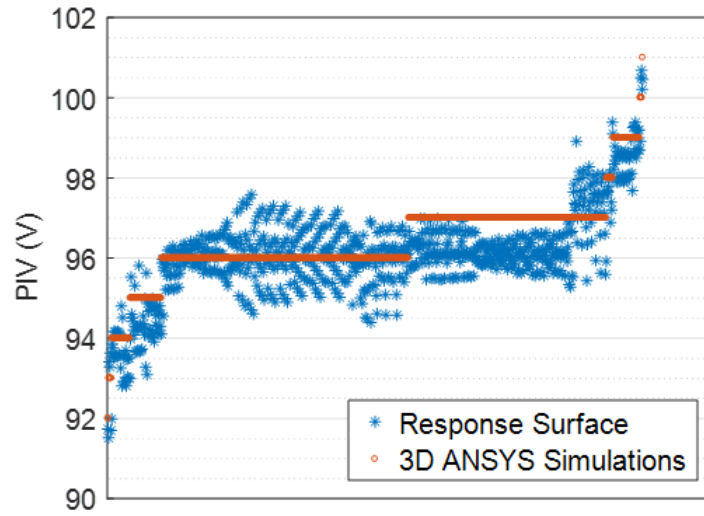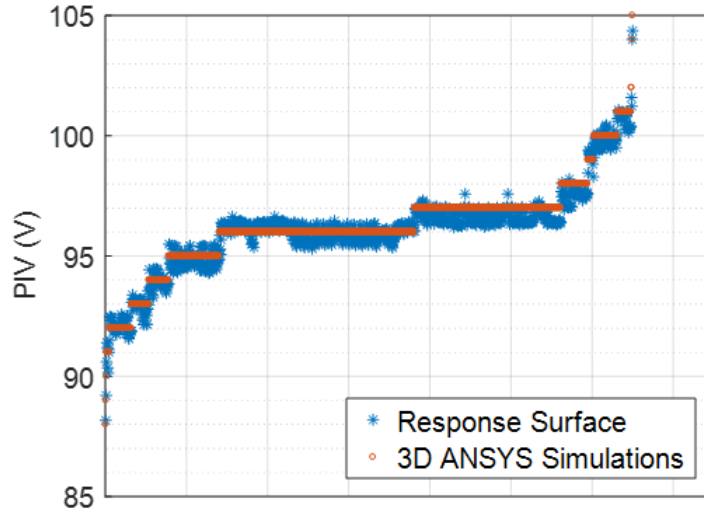


Figure 4.11.   Comparison of predictions from a second-order polynomial response surface of the PIV to 1300 additional simulations. Results are sorted by the simulation PIV.

### 4.3.2   Propagation of Uncertainty

To generate the output PDF of expected PIV and natural frequency ranges, the cosine coefficients and sine coefficients, for each of the top and bottom surfaces, are sampled. Uniform probability distributions were assumed for all parameters. Ranges of $\pm0.07\mu m$ were chosen for the low-frequency coefficients where $(i + j) = 1$, such as $C_{10}^{top}$ and $S_{10}^{bot}$. This was halved to $\pm0.035\mu m$ for coefficients where $(i + j) = 2$ such as $C_{20}^{top}$ and $S_{02}^{bot}$, halved again for coefficients where $(i+j) = 3$ such as $C_{21}^{top}$ and $S_{12}^{bot}$, and finally halved again for coefficients where $(i + j) = 4$ such as $C_{22}^{top}$ and $S_{31}^{bot}$; the minimum uniform range used was therefore approximately $\pm0.01\mu m$. The profiles and associated distributions of uncertainty are shown in Table 4.12.
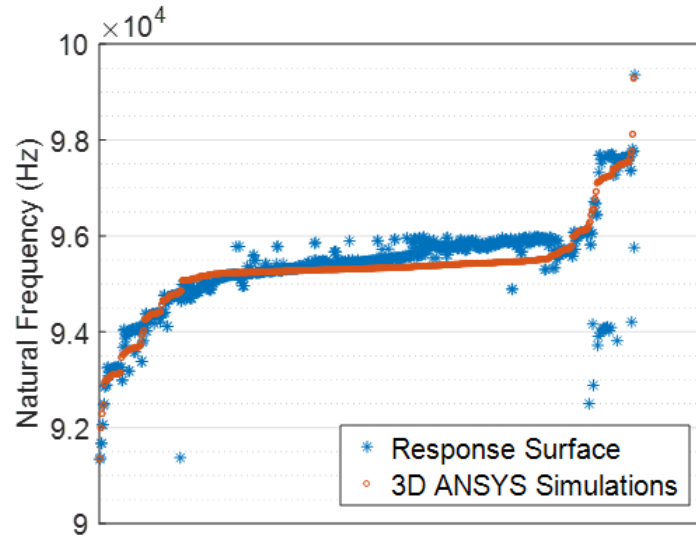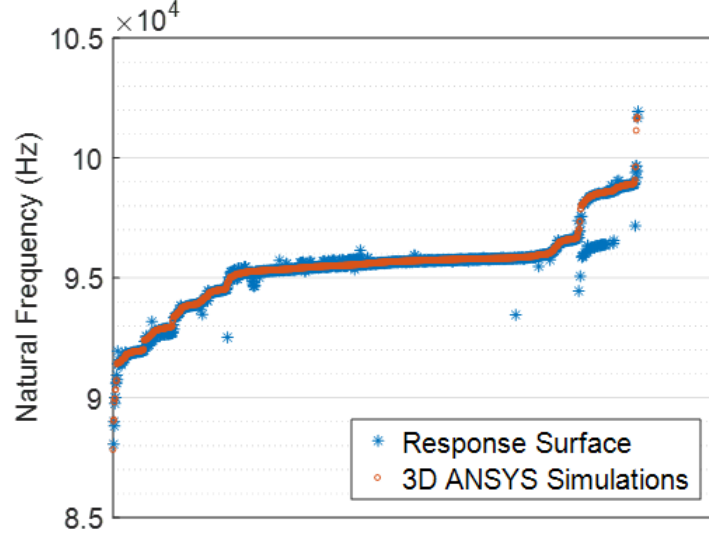
Figure 4.12. Comparison of predictions from a second-order polynomial response surface of the first natural frequency to 1300 additional simulations. Results are sorted by the simulation frequency.

The distributions of uncertainty shown in Table 4.12 are assumptions of the real values; they are not the results of experimental sampling of profile thicknesses. It is assumed here that the lower-frequency coefficients (e.g. $C_{10}^{bot}$) occur at greater amplitudes than the higher-frequency coefficients (e.g. $S_{22}^{bot}$) in manufactured devices. The magnitudes of these ranges, however, have been intentionally scaled to generate films in which the thickness varies within 5% to 10% of the nominal thickness of 3 microns, which is in the range of the wafer-scale thickness nonuniformity seen in, e.g., [93] and [94]. This is achieved, as the maximum thickness at any point on this set of films is increased by a mean of 7.1% with a standard deviation of 1.7%.

250,000 samples are randomly drawn from this parameter space of profile coefficients, and a PIV and natural frequency is calculated for each sample by application of the second-order polynomial response surfaces. These collections form probability density functions (PDFs) of the PIV and natural frequency. The resulting PDFs are shown in Figure 4.13 and Figure 4.14, in addition to the mean values of the PDFs

Table 4.12. Assumed distributions of uncertainty in the amplitudes of the 2D Fourier coefficients representing, separately, the top and and bottom surfaces.

| Profiles (Top and Bottom Surfaces) | | | Uniform Distribution |
|---|---|---|---|
| $C_{10}$ | | $S_{10}$ | $\pm 70.0 nm$ |
| $C_{01}$ | | $S_{01}$ | |
| $C_{20}$ | | $S_{20}$ | $\pm 35.0 nm$ |
| $C_{11}$ | | $S_{11}$ | |
| $C_{02}$ | | $S_{12}$ | |
| $C_{30}$ | | $S_{30}$ | $\pm 17.5 nm$ |
| $C_{21}$ | | $S_{21}$ | |
| $C_{12}$ | | $S_{12}$ | |
| $C_{40}$ | | $S_{40}$ | $\pm 8.75 nm$ |
| $C_{22}$ | | $S_{22}$ | |

and the nominal values for the flat film. The mean values of the PIV and natural frequency are both seen to be greater than their nominal values.
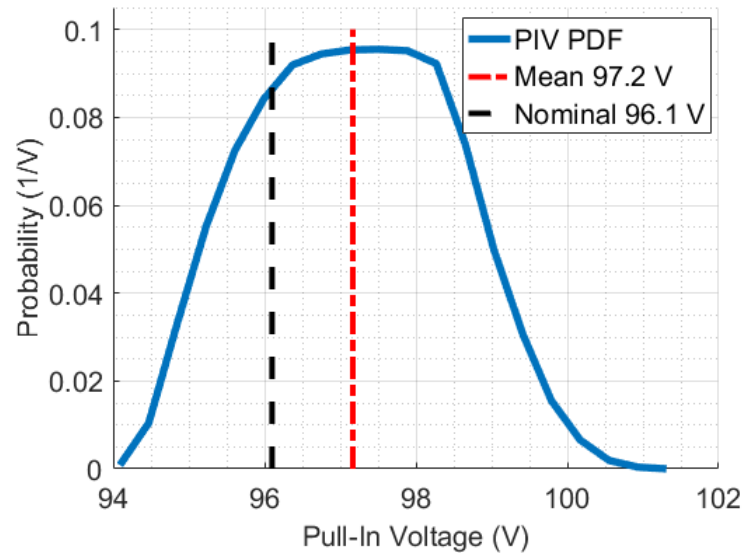
Figure 4.13. PDF of PIVs generated by sampling response surface.
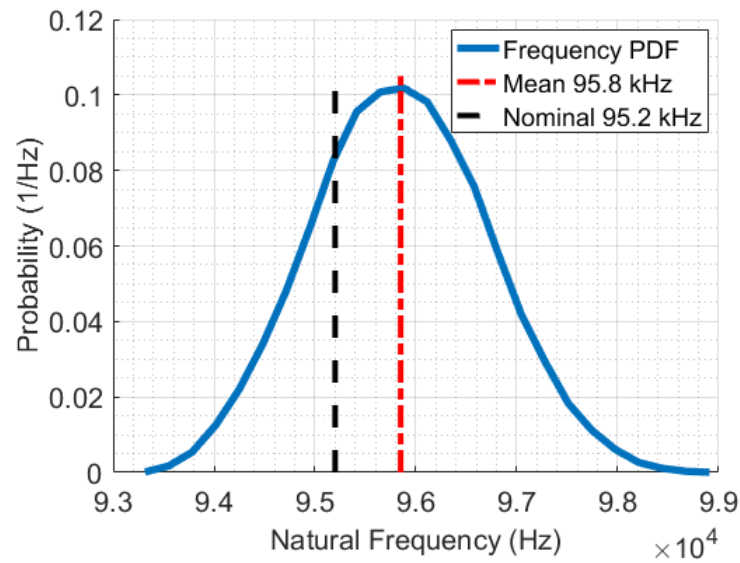


Figure 4.14. PDF of first natural frequency generated by sampling response surface.

An example top and bottom film surface generated during this process is shown in Figure 4.15. The length and width of the film have been scaled down to make the

variation in thickness more evident. The middle surface, halfway between the top and bottom surfaces, is also shown.
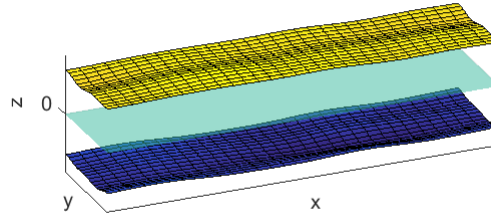


Figure 4.15. Example surface generated during response surface sampling. Contains contributions from all 40 parameters. The $z = 0$ surface is also shown.

## 4.4   Discussion of 3D Finite Element Model Results

A portion of the response surface generated for the PIV is illustrated in Figure 4.16. In this figure, the 1300 full 3D simulations not used in generating the reponse surface are scatter-plotted against the two Fourier cosine coefficients $C_{10}^{top}$ and $C_{20}^{top}$ for the top surface. The response surface is plotted as a function of these two variables in the range of $\pm 0.15 \mu m$ for each parameter, with the remaining parameters set to their nominal values of zero. The response surface is seen to be approximately linear for these two variables.

The response surface is shown again as level curves in Figure 4.17. The linear response of the PIV to each parameter remains evident.

The portion of the PIV response surface level curves representing only the variation of the coefficients $C_{10}^{bot}$ and $C_{20}^{bot}$ on the bottom surface are shown in Figure 4.18. In contrast to the effect of these two coefficients on the top surface, the response on
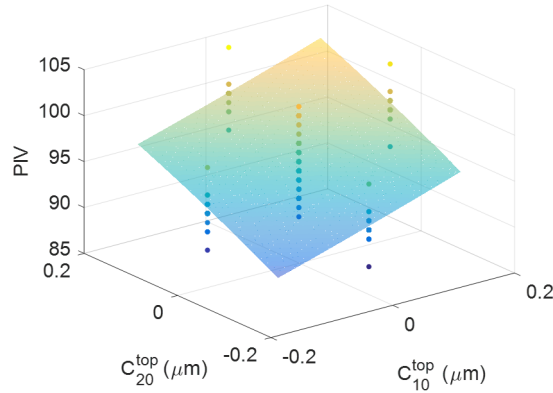
Figure 4.16. Illustration of the PIV polynomial response surface as it varies for two cosine coefficients on the top surface of the film, plotted with simulated values of the PIV.
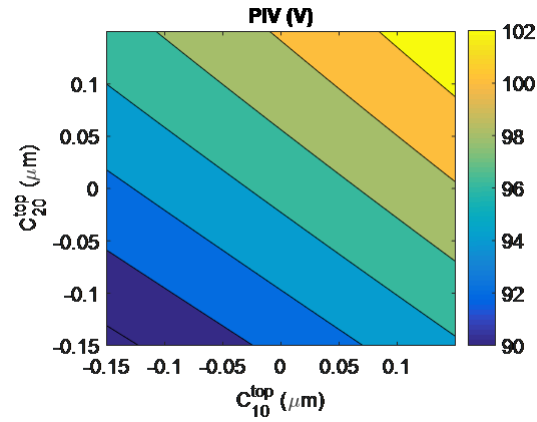


Figure 4.17. Illustration of the level curves of the PIV polynomial response surface as it varies for two cosine coefficients on the top surface of the film.

the bottom surface is evidently nonlinear; as both coefficients are decreased, the PIV increases by more than the linear combination of their linear effects.

Finally, the level curves of the response surface for the natural frequency are shown in Figure 4.19 as a comparison of the effects of the sine and cosine profiles. Each cosine profile in the plots shown monotonically increased or decreased the PIV.
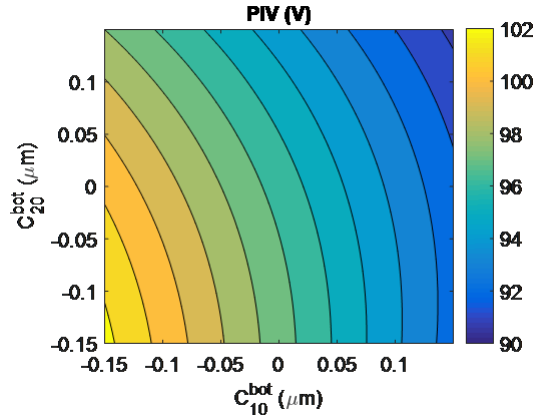
Figure 4.18. Illustration of the level curves of the PIV polynomial response surface as it varies for two cosine coefficients on the bottom film surface.

The sine profiles, in contrast, have a smaller impact on the PIV and natural frequency and have a much less linear effect, as illustrated in Figure 4.19.
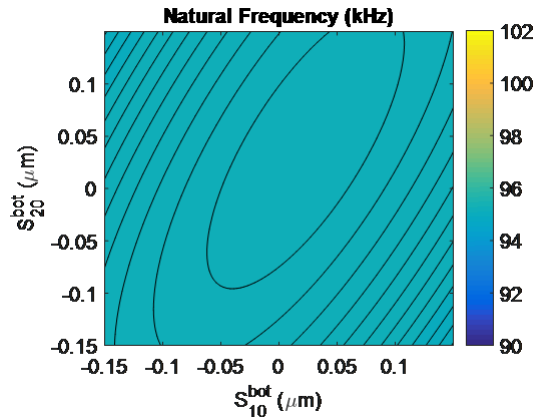


Figure 4.19. Illustration of the level curves of the polynomial response surface generated for the natural frequency as it varies for two sine coefficients on the bottom film surface.

Noting that the greatest sensitivity to the change in profile occurs when the profile is varied along its length, variability in thickness is added to a 1D Euler-Bernoulli continuum beam model of the same device. The model is introduced as a rapid alter-

native to the full 3D or similar 2D simulations. It allows a more thorough examination of the effect of the profiles which vary along the length of the film.

## 4.5    1D Euler-Bernoulli Continuum Beam Model of the Film

### 4.5.1    Description of 1D Model

It would be possible to model the system described above in ANSYS using a 1D model composed of, for example, a large number of 1D beam elements with varying assigned thicknesses. However, because a 1D Euler-Bernoulli beam model has already been used in Chapter 2 to represent the film, and in the hope that it provides additional insight into the effects of varying thickness, the 1D Euler-Bernoulli beam model previously descibed, solved using the Ritz-Galerkin method, will be further modified to incorporate the varying thickness of the film.

In the following simulations, the dielectric thickness is set to zero, and damping and fringe field effects are neglected in the 1D model in order to better match the assumptions made in the 3D model, which does not include these effects. An effective modulus is still applied in the 1D model in order to better approximate the plate-like stiffness of the wide film. Material and geometric properties are otherwise identical between the 1D and 3D models.

### 4.5.2    Derivation of 1D Equation of Motion

The moments acting on a section of the undeformed curved film are first balanced.

Figure 4.20 shows the dimensions of and forces on a section of the undeformed, initially-curved film with non-uniform thickness. The film is described as a core of constant thickness, with additional thickness $h_t(x)$ above the film core and $h_b(x)$ below the core.

Summing the moments on the film shown in Figure 4.20 about the left-center of the film, which is the assumed location of the neutral axis at this cross-section,
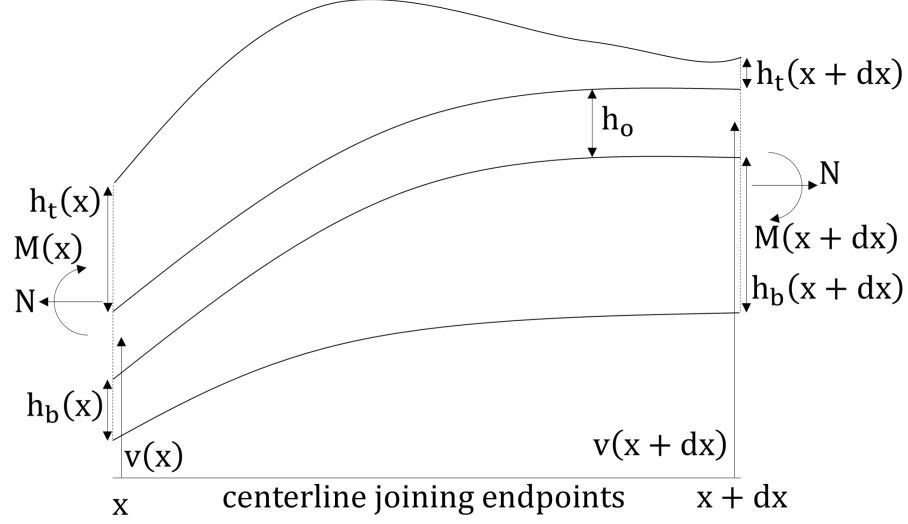
Figure 4.20. Schematic of the RF-MEMS switch of non-uniform thickness with the membrane deflected in the form of an arch due to residual stresses.

$$0 = M_o(x + dx) - M_o(x) -$$
$$N([v(x + dx) - v(x)] + [h_t(x + dx) - h_t(x)]/2 - [h_b(x + dx) - h_b(x)]/2),$$

(4.5)

where $dx$ is the length of the element, $M_o(x)$ is the moment on the element's cross-section, $N$ is the axial force which is meant to approximate the residual stress on the element, and $v(x)$ is the initial height of the film's core above its location at the film's anchors. This height $v(x)$ comprises the initial shape of the film before electrostatic deformation.

Dividing Equation 4.5 by $dx$ and taking the limit as $dx$ goes to zero,

$$M_o' = N(v' + h_t'/2 - h_b'/2).$$

(4.6)

where $[\bullet]'$ denotes differentiation of $[\bullet]$ with respect to the x-coordinate.

Having balanced the moments on the undeformed curved film, the moments acting on the deformed curved film are now balanced.

The film shown in Figure 4.20 is shown in a deformed position in Figure 4.21, where a positive-downward deflection $w(x)$ has occurred.
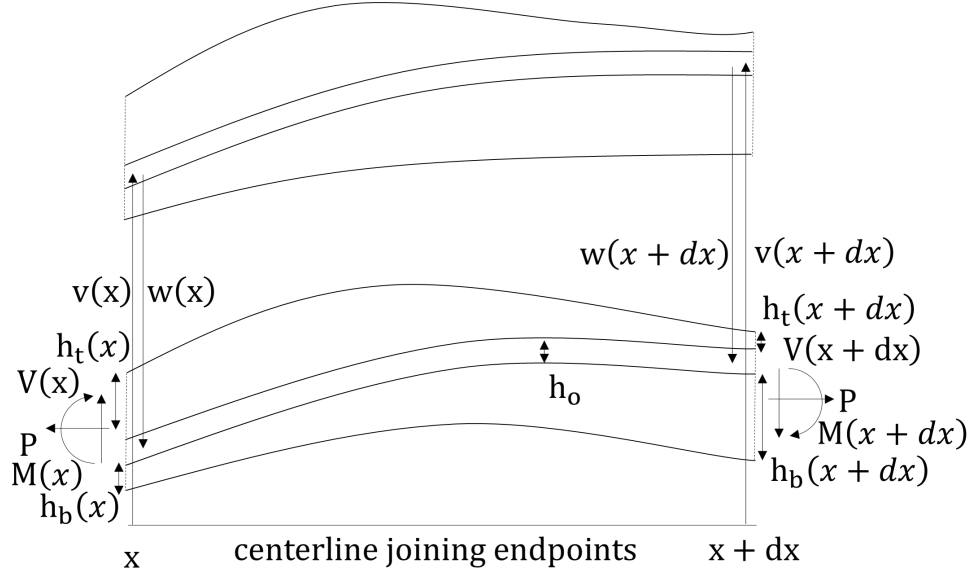


Figure 4.21. Schematic of the RF-MEMS switch of non-uniform thickness with initial curvature, deformed by the application of electrostatic forcing.

The deformation will cause an additional moment $M_w(x)$, which is added to the initial moment $M_o(x)$. This combination yields the moment $M(x)$ shown in Figure 4.21, where

$$M(x) = M_o(x) + M_w(x). \tag{4.7}$$

Similarly, the deformation will result in additional axial stress $N_w$ which is combined with the pre-existing axial stress $N$ to yield

$$P = N + N_w, \tag{4.8}$$

as shown in Figure 4.21.

Summing moments about the left-center of the film shown in Figure 4.21 yields

$$0 = M_w(x + dx) - M_w(x) + M_o(x + dx) - M_o(x)$$
$$- P([v(x + dx) - v(x)] - [w(x + dx) - w(x)]+$$
$$[h_t(x + dx) - h_t(x)]/2 - [h_b(x + dx) - h_b(x)]/2)-$$
$$V(x + dx)dx. \tag{4.9}$$

where $V(x)$ is the shear force on the film's cross-section.

Dividing Equation 4.9 by $dx$, and taking the limit as $dx$ goes to zero gives

$$0 = M_w' + M_o' - P(v' - w' + h_t'/2 - h_b'/2) - V \tag{4.10}$$

Substituting the equation for $M_o'(x)$ from Equation 4.6 into Equation 4.10 gives

$$0 = M_w' + N(v' + h_t'/2 - h_b'/2) - P(v' - w' + h_t'/2 - h_b'/2) - V \tag{4.11}$$

After balancing the moments on the deformed curved film, the vertical forces acting on a section of the deformed, curved film are balanced.

Summing forces in the vertical direction on the film element shown in Figure 4.21,

$$\rho b h(x)\ddot{x}dx = f(x)dx - V(x + dx) + V(x) \tag{4.12}$$

where $f(x)$ is a distributed load per unit length applied to the film, $\rho$ is the film density, $b$ is the width of the film, and $h(x)$ is the film thickness, given by the sum of the uniform film core thickness $h_o$ and the additional thickness above and below the film core, $h_t(x)$ and $h_b(x)$, respectively, or

$$h(x) = h_b(x) + h_o + h_t(x). \tag{4.13}$$

Dividing Equation 4.12 by $dx$ and taking the limit as $dx$ goes to zero gives the equation of motion for the lateral displacement of the film,

$$\rho b h(x)\ddot{x} = f(x) - V'(x). \tag{4.14}$$

The $V'$ term in Equation 4.14 will be expanded into known terms by the use of two further equations.

Equation 4.11, the summation of moments on the deformed film, is differentiated with respect to x and solved for $V'$ to yield

$$V' = M_w'' + N(v'' + h_t''/2 - h_b''/2) - P(v'' - w'' + h_t''/2 - h_b''/2) \qquad (4.15)$$

In accordance with the Euler-Bernoulli beam theory applied here to represent the film, it is known that the deformation-related moment $M_w$ is related to the deformation $w(x)$, modulus of elasticity $E$, and area moment of inertia $I(x)$ by

$$M_w'' = [EI(x)w'']''. \qquad (4.16)$$

Substituting Equation 4.16 and Equation 4.15 into the governing equation of motion, Equation 4.14, yields

$$\rho b h(x)\ddot{x} = f(x) - [EI(x)w'']'' - N(v'' + \frac{h_t''}{2} - \frac{h_b''}{2}) - P(v'' - w'' + \frac{h_t''}{2} - \frac{h_b''}{2}). \ (4.17)$$

Having balanced the vertical forces acting on a section of the deformed curved film, the electrostatic forcing function is now considered.

The electrostatic forcing function used in this 1D model of the system models the same effect as, but is not identical to, the electrostatic model used in the ANSYS simulations previously described. As with other modeling differences between the 1D and 3D model, this difference is presumed to cause a small difference in the estimated PIV. The fringe-field model of the electrostatic force on the film is taken from [73]. The capacitance per unit length in this model is given by

$$C = \frac{\epsilon_0}{b}[1 - 0.36\frac{g(x)}{b} + (0.85\frac{1}{b^{0.76}} + 2.5\frac{h(x)^{0.24}}{b}g(x)^{0.76})], \qquad (4.18)$$

where $C$ is the capacitance, $\epsilon_0 = 8.85 * 10^{-12} F/m$ is the permittivity of free space, the gap $g(x)$ is given by

$$g(x) = g_o - h_b(x) + v(x) - w(x), \tag{4.19}$$

where the thickness $h_b(x)$ added to the bottom of the film has affected the gap, and where the effective air gap $g_o$ is given by

$$g_o = t_{air} + \frac{t_d}{\epsilon_0}. \tag{4.20}$$

The formula in Equation 4.18 has been modified from its initial form to incorporate the non-uniform thickness $h(x)$ and the initial curvature $v(x)$.

The electrostatic potential energy resulting from the capacitance given in Equation 4.18 is given by

$$E_p = \frac{1}{2}C\bar{v}^2, \tag{4.21}$$

where $\bar{v}$ is the voltage differential between the two terminals of the capacitor.

Inserting the capacitance from Equation 4.18 yields the electrostatic potential energy between the film and the electrode beneath,

$$E_p = \frac{\bar{v}^2}{2}\frac{\epsilon_0}{b}[1 - 0.36\frac{g(x)}{b} + (0.85\frac{1}{b^{0.76}} + 2.5\frac{h(x)^{0.24}}{b}g(x)^{0.76})]. \tag{4.22}$$

Differentiating the electrostatic potential energy in Equation 4.22 with respect to the gap $g(x)$ yields the magnitude of the electrostatic force on the film,

$$|F_{elec}| = \frac{\bar{v}^2\epsilon_0 b}{2g^2}(1 + 0.24g^{0.76}(0.85\frac{1}{b^{0.76}})g^{0.76}). \tag{4.23}$$

The electrostatic force in Equation 4.23 is further modified with a Heaviside step function $H(x)$ to allow for the possibility of an electrode of finite width below the film. Only the electrostatic force between the left side of the electrode where $x = x_1$ and the right side of the electrode where $x = x_2$ is included in the final electrostatic force, given by

$$|F_{elec}| = \frac{\bar{v}^2\epsilon_0 b}{2g^2}(1 + 0.24g^{0.76}(0.85\frac{1}{b^{0.76}})g^{0.76})(H(x - x_1) - H(x - x_2)). \tag{4.24}$$

Although it is presented here, an electrode of finite width is not used here; the electrode is treated as though it extends across the full length of the suspended film above it.

With the electrostatic forcing function determined, the stretching function is now considered.

The stretching force $P_w$ on the film is given simply by

$$P_w = \frac{Ebh(x)}{L}\Delta S \tag{4.25}$$

where $\Delta S$ is the change in the length of the film between the current deformed length and the initial undeformed length, and is given by the change in the arc length of the film,

$$\Delta S = \int_0^L \sqrt{1 + (v' + \frac{h_t'}{2} - \frac{h_b'}{2} - w')^2}dx - \int_0^L \sqrt{1 + (v' + \frac{h_t'}{2} - \frac{h_b'}{2})^2}dx, \tag{4.26}$$

which is approximated by its first-order binomial expansion,

$$\Delta S \approx \int_0^L (1 + \frac{1}{2}(v' + \frac{h_t'}{2} - \frac{h_b'}{2} - w')^2)dx - \int_0^L (1 + \frac{1}{2}(v' + \frac{h_t'}{2} - \frac{h_b'}{2})^2)dx). \tag{4.27}$$

Equation 4.27 simplifies to

$$\Delta S \approx \frac{1}{2}\int_0^L [h_b'w' - h_t'w' + w'^2 - 2v'w']dx. \tag{4.28}$$

Substituting Equation 4.27 into the equation for the stretching force on the film, Equation 4.25, gives the stretching force $P_w$,

$$P_w = \frac{Ebh(x)}{2L}[\int_0^L (h_b'w' - h_t'w' + w'^2 - 2v'w')dx]. \tag{4.29}$$

With the stretching function determined, the damping forcing function is now considered.

The magnitude of the damping force will be given by

$$|F_{damp}| = c_f(w, x)\dot{w}, \tag{4.30}$$

where $c_f$ is given by [71] as

$$c_f = \frac{10.39 * \left(\frac{b}{t_{air} - h_b + v + \gamma - w}\right)^{3.1}}{1 + 1.374\left(\frac{b}{t_{air} - h_b + v + \gamma - w}\right)^{1.825}\left(\frac{\gamma}{b}\right)^{0.966}} h, \tag{4.31}$$

which has been modified here to account for the thickness $h_b$ added to the bottom of the film as well as the initial curvature $v$. A minimum gap of $\gamma = 20nm$ is assumed to exist due to asperities in the film and electrode surfaces.

The total magnitude of the damping force is therefore given by

$$|F_{damp}| = \frac{10.39 * \left(\frac{b}{t_{air} - h_b + v + \gamma - w}\right)^{3.1}}{1 + 1.374\left(\frac{b}{t_{air} - h_b + v + \gamma - w}\right)^{1.825}\frac{\gamma^{0.966}}{b}} h\dot{w}, \tag{4.32}$$

Although the damping force is derived here, damping is not considered in the simulations in this chapter.

With the damping function determined, the impact forcing function is now considered.

If impact occurs, the resulting impact force will be given by a simple spring model wherever contact occurs. This model is given by

$$F_{impact} = -\frac{Eb}{t_d}(w - v - t_{air} + h_b)(w \geq v + t_{air} - h_b). \tag{4.33}$$

Although the impact term is derived here, impact is not considered in the simulations in this chapter.

### 4.5.3 Governing Equation of Motion for the Lateral Vibration of a Film with Non-Uniform Thickness

Combining the vertical force balance given by Equation 4.17 with each of the forcing functions given by Equation 4.24, Equation 4.29, Equation 4.32, and Equation

4.33 yields the final governing equation of motion for the lateral motion of the film with non-uniform thickness,

$$
\rho b h \ddot{w} + [E \frac{b h^3}{12} w'']'' =
$$
$$
\frac{\bar{v}^2 \epsilon_0 b}{2 g^2} (1 + 0.24 g^{0.76} (0.85 \frac{1}{b^{0.76}}) g^{0.76})(H(x - x_1) - H(x - x_2)) +
$$
$$
\frac{E b h}{2 L} [\int_0^L (h_b' w' - h_t' w' + w'^2 - 2 v' w') dx](v'' - w'' + \frac{h_t''}{2} - \frac{h_b''}{2}) -
$$
$$
\frac{10.39 * (\frac{b}{t_{air} - h_b + v + \gamma - w})^{3.1}}{1 + 1.374(\frac{b}{t_{air} - h_b + v + \gamma - w})^{1.825}(\frac{\gamma}{b})^{0.966}} h \dot{w}
$$
$$
- \frac{E b}{t_d}(w - v - t_{air} + h_b)(w \geq v + t_{air} - h_b) - N(v'' + \frac{h_t''}{2} - \frac{h_b''}{2}).
$$
(4.34)

### 4.5.4 Nondimensionalization of the Governing Equation of Motion for the Lateral Vibration of a Film with non-uniform thickness

To solve Equation 4.34 the following nondimensional quantities are defined:

$$
\begin{aligned}
\hat{x} &= \frac{x}{L}, \\
\hat{t} &= \frac{t}{T} = \frac{t}{\sqrt{\frac{\rho b h_o L^4}{E b h_o^3/12}})}, \\
\hat{w} &= \frac{w}{g_o}, \\
\hat{v} &= \frac{v}{g_o}, \\
\hat{x}_1 &= \frac{x_1}{L}, \\
\hat{x}_2 &= \frac{x_2}{L}, \\
\hat{N} &= \frac{N L^2}{EI}, \\
\omega_n &= \frac{\omega_n}{\sqrt{\frac{EI}{\rho b h L^4}}}.
\end{aligned}
$$
(4.35)

The time $t$ is nondimensionalized with a constant $T = \sqrt{\frac{\rho b h_o L^4}{E b h_o^3/12}}$. After nondimensionalization, Equation 4.34 can be expressed as:

$$\frac{h}{h_o}\ddot{\hat{w}} + \frac{h^3}{h_o^3}\hat{w}^{''''} + \frac{6h^2h'}{h_o^3}\hat{w}^{'''} + \frac{3h^2h'' + 6hh'^2}{h_o^3}\hat{w}^{''} =$$

$$\frac{6\bar{v}^2\epsilon_0 L^4}{g^2 E h_o g_o}(1 + 0.24g^{0.76}(0.85\frac{1}{b^{0.76}})g^{0.76})(H(x - x_1) - H(x - x_2))+$$

$$\frac{6hg_o^2}{h_o^3}[\int_0^1 (\frac{h_b'}{g_o}\hat{w}' - \frac{h_t'}{g_o}\hat{w}' + \hat{w}'\hat{w}' - 2\hat{v}'\hat{w}')d\hat{x}](\hat{v}'' - \hat{w}'' + \frac{h_t''}{2g_o} - \frac{h_b''}{2g_o})-$$ 

$$\frac{10.39 * (\frac{b}{t_{air}-h_b+v+\gamma-w})^{3.1}}{1 + 1.374(\frac{b}{t_{air}-h_b+v+\gamma-w})^{1.825}(\frac{\gamma}{b})^{0.966}}\frac{12L^4 h}{Ebh_o^3 g_o}\dot{w}$$

$$- \frac{12L^4}{t_d h_o^3}(\hat{w} - \hat{v} - 1 + \frac{h_b}{g_o})(\hat{w} \geq \hat{v} + 1 - \frac{h_b}{g_o}) - \frac{12L^2 N}{Ebh_o^3}(\hat{v}'' + \frac{h_t''}{2g_o} - \frac{h_b''}{2g_o}).$$

(4.36)

Into Equation 4.36 the assumed solution

$$\hat{w}(\hat{x}, \hat{t}) \approx \sum_{i=0}^{i=M} u_i(\hat{t})\phi_i(\hat{x}), \tag{4.37}$$

is inserted, where $u_i$ is the time-varying coefficient of the $i^{th}$ mode of the uniform undamped flat film, $\phi_i$ is the mode shape of the $i^{th}$ mode of the uniform undamped flat film, and $M$ is the number of modes chosen. Multiplying through by the orthonormal modeshapes $\phi_n$ and integrating along the length of the film yields the the final set of ordinary differential equations which is to be solved.

### 4.5.5 Verification of 1D Model

In this section, the calculation of the natural frequencies of a non-uniform film are verified and the convergence characteristics of the calculated natural frequencies for a fixed-fixed tapered film with the properties given in Table 4.13 are considered. Later, the natural frequencies of this tapered film are compared to reference values from [105].

Neglecting the forcing functions and stretching of the film, the governing equation for the motion of the non-uniform film was previously derived as

$$\frac{\partial^2}{\partial x^2}(E\frac{bh^3}{12}\frac{\partial^2}{\partial x^2}(w)) + \rho bh\frac{\partial^2}{\partial t^2}(w) = 0, \tag{4.38}$$

Table 4.13.  Parameters of the Linearly Tapered Film.

| Symbol | Quantity | Value |
|---|---|---|
| $L$ | Film Length | 400 $\mu$m |
| $b$ | Film Width | 120 $\mu$m |
| $\nu$ | Poisson's Ratio | 0.30 |
| $E$ | Young's Modulus | 200 GPa |
| $h_o$ | Nominal Thickness of the Film | 4.0$\mu$m |
| $h_t$ | Non-Uniform Thickness on Film Top | 1.5$\frac{x}{L}\mu$m |
| $h_b$ | Non-Uniform Thickness on Film Underside | 2.5$\frac{x}{L}\mu$m |

where $E$ is the Young's modulus, $b$ is the width, $h = h(x)$ is the thickness, $w$ is the deflection, and $\rho$ is the density of the film.

Multiplying Equation 4.38 by $12L^4/Ebh_o^3g_o$ and nondimensionalizing with the use of

$$\hat{x} = \frac{x}{L} \tag{4.39}$$

$$\hat{w} = \frac{w}{g_o} \tag{4.40}$$

$$\hat{t} = \frac{t}{T} \tag{4.41}$$

$$T = \sqrt{\frac{\rho bh_o L^4}{Ebh_o^3/12}} \tag{4.42}$$

where $h_o$ is the initial thickness of the film, results in the nondimensionalized equation of motion for the unforced motion of the non-uniform film,

$$(1 + \frac{h_t + h_b}{h_o})\ddot{\hat{w}} + ((1 + \frac{(h_t + h_b)^3}{h_o^3})\hat{w}'')'' = 0, \tag{4.43}$$

where $[\dot{\bullet}]$ represents differentiation of $[\bullet]$ with respect to time, $[\bullet]'$ represents differentiation of $[\bullet]$ with respect to $\hat{x}$, and $h_t = h_t(x)$ and $h_b = h_b(x)$ represent the non-uniform thicknesses added to the top and the bottom of the film, respectively.

Into Equation 4.43 the assumed solution

$$\hat{w}(\hat{x}, \hat{t}) \approx \sum_{i=0}^{i=M} u_i(\hat{t})\phi_i(\hat{x}), \tag{4.44}$$

is inserted, where $u_i$ is the time-varying coefficient of the $i^{th}$ mode of the uniform undamped flat film, $\phi_i$ is the mode shape of the $i^{th}$ mode of the uniform undamped flat film, and $M$ is the number of modes chosen. The substitution of Equation 4.44 into Equation 4.43 yields the equations of motion

$$\sum_{i=0}^{i=M} \frac{h_o + h_t + h_b}{h_o}\ddot{u}_i\phi_i + \sum_{i=0}^{i=M}(\frac{(h_o + h_t + h_b)^3}{h_o^3}u_i\phi_i'')'' = 0, \tag{4.45}$$

which, when the differentiation on the second term is carried out, becomes

$$\begin{aligned}
0 = &\sum_{i=0}^{i=M} \frac{h_o + h_t + h_b}{h_o}\ddot{u}_i\phi_i + \\
&\sum_{i=0}^{i=M} \frac{(h_o + h_t + h_b)^3}{h_o^3}u_i\phi_i'''' + \\
&\sum_{i=0}^{i=M} 2\frac{3(h_o + h_t + h_b)^2(h_t' + h_b')}{h_o^3}u_i\phi_i''' + \\
&\sum_{i=0}^{i=M} \frac{3(h_o + h_t + h_b)^2(h_t'' + h_b'') + 6(h_o + h_t + h_b)(h_t' + h_b')^2}{h_o^3}u_i\phi_i''.
\end{aligned} \tag{4.46}$$

Following the procedure of the Galerkin Method, further multiplication of this equation by the modeshapes $\phi_n$ and integration from $\hat{x} = 0$ to $\hat{x} = 1$ yields the system of equations

$$0 = M_{in}\ddot{u}_i + K_{in}u_i \tag{4.47}$$

where $M_{ij}$ is given by

$$M_{in} = \int_{\hat{x}=0}^{\hat{x}=1} [\frac{h_o + h_t + h_b}{h_o}\phi_i]\phi_n d\hat{x} \tag{4.48}$$

and $K_{ij}$ is given by

$$K_{ij} =$$

$$\int_{\hat{x}=0}^{\hat{x}=1} [\frac{(h_o + h_t + h_b)^3}{h_o^3} u_i \phi_i''''] \phi_n d\hat{x} +$$

$$\int_{\hat{x}=0}^{\hat{x}=1} [2\frac{3(h_o + h_t + h_b)^2(h_t' + h_b')}{h_o^3} u_i \phi_i'''] \phi_n d\hat{x} +$$

$$\int_{\hat{x}=0}^{\hat{x}=1} [\frac{3(h_o + h_t + h_b)^2(h_t'' + h_b'') + 6(h_o + h_t + h_b)(h_t' + h_b')^2}{h_o^3} u_i \phi_i''] \phi_n d\hat{x}.$$

$$(4.49)$$

The natural frequencies in $rad/s$ of the uniform, fixed-fixed, undamped, flat film of thickness $h_o$ are defined by the equations (see references [105] and [106])

$$f_i = \frac{\lambda_i^2}{L^2} \sqrt{\frac{Ebh^3}{12\rho A}}, \qquad (4.50)$$

and the mode shapes are given by the function (see reference [105])

$$\hat{\phi}_i = cosh(\lambda_i \frac{x}{L}) - cos(\lambda_i \frac{x}{L}) - (\frac{cosh(\lambda_i) - cos(\lambda_i)}{sinh(\lambda_i) - sin(\lambda_i)})(sinh(\lambda_i \frac{x}{L}) - sin(\lambda_i \frac{x}{L})), \quad (4.51)$$

which suffers in that higher-order modeshapes $(M > 22)$ are difficult to calculate in double-precision. The first and twenty-second modeshapes, scaled so that their maximum amplitudes are one, are shown in Figure 4.22.

Nondimensionalizing with

$$\hat{x} = \frac{x}{L}, \qquad (4.52)$$

these modeshapes and their derivatives with respect to $\hat{x}$ may be written as

$$\hat{\phi}_i = cosh(\lambda_i \hat{x}) - cos(\lambda_i \hat{x}) + (sin(\lambda_i \hat{x}) - sinh(\lambda_i \hat{x}))\frac{cos(\lambda_i) - cosh(\lambda_i)}{sin(\lambda_i) - sinh(\lambda_i)} \qquad (4.53)$$

$$\hat{\phi}_i' = \lambda_i sin(\lambda_i \hat{x}) + \lambda_i sinh(\lambda_i \hat{x}) + (\lambda_i cos(\lambda_i \hat{x}) - \lambda_i cosh(\lambda_i \hat{x}))\frac{cos(\lambda_i) - cosh(\lambda_i)}{sin(\lambda_i) - sinh(\lambda_i)} \quad (4.54)$$
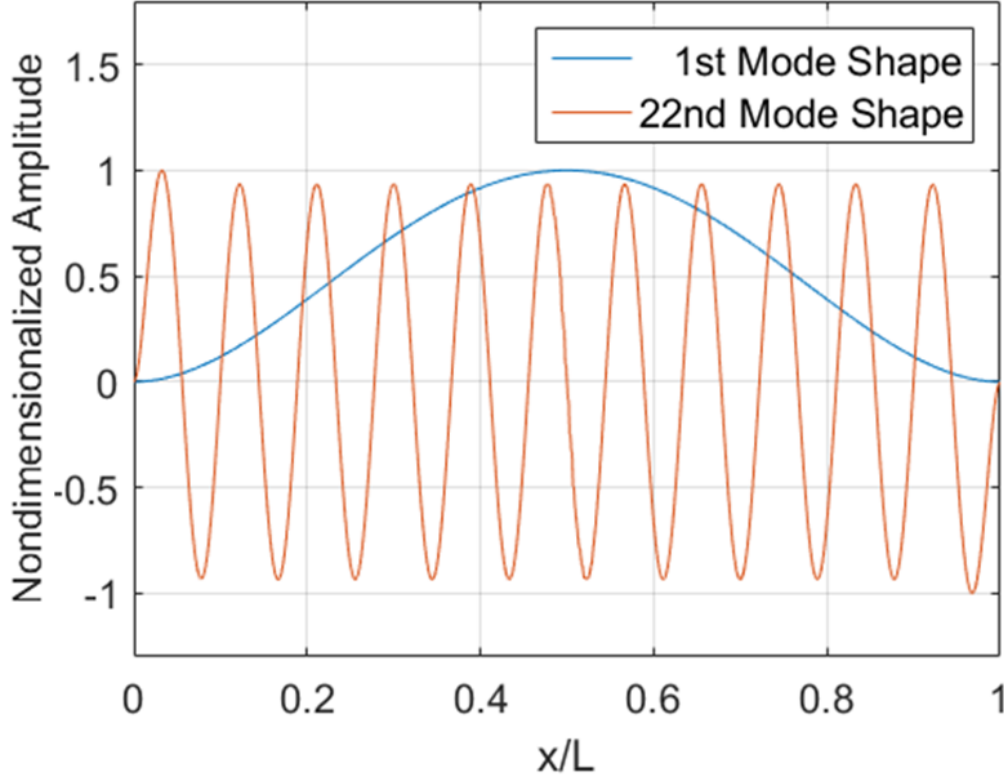
Figure 4.22.  Mode shapes 1 and 22 for the undamped uniform fixed-fixed film.

$$\hat{\phi}_i'' = \lambda_i^2 cos(\lambda_i\hat{x}) + \lambda_i^2 cosh(\lambda_i\hat{x}) - (\lambda_i^2 sin(\lambda_i\hat{x}) + \lambda_i^2 sinh(\lambda_i\hat{x})) \frac{cos(\lambda_i) - cosh(\lambda_i)}{sin(\lambda_i) - sinh(\lambda_i)} \quad (4.55)$$

$$\hat{\phi}_i''' = \lambda_i^3 sinh(\lambda_i\hat{x}) - \lambda_i^3 sin(\lambda_i\hat{x}) - (\lambda_i^3 cos(\lambda_i\hat{x}) + \lambda_i^3 cosh(\lambda_i\hat{x})) \frac{cos(\lambda_i) - cosh(\lambda_i)}{sin(\lambda_i) - sinh(\lambda_i)}$$
$$(4.56)$$

$$\hat{\phi}_i'''' = \lambda_i^4 cosh(\lambda_i\hat{x}) - \lambda_i^4 cos(\lambda_i\hat{x}) + (\lambda_i^4 sin(\lambda_i\hat{x}) - \lambda_i^4 sinh(\lambda_i\hat{x})) \frac{cos(\lambda_i) - cosh(\lambda_i)}{sin(\lambda_i) - sinh(\lambda_i)}$$
$$(4.57)$$

These modeshapes and their derivatives are used to calculate the natural frequencies of the non-uniform film, which are the eigenvalues of the equations defined by Equation 4.47. These natural frequencies are seen to converge in Figure 4.23, in which the natural frequencies of the non-uniform film are divided by their final approximation after 22 modes are included. The natural frequency of the first mode

is seen to drop from about 11% above its final value when one mode is used in its approximation to within about 1% of its final value when two modes are used.

The first approximations of each new mode appear to decline in accuracy, as may be seen when the first mode, initially about 10% higher than its ultimate value, is compared to the 17th mode, which is initially about 15% higher than its ultimate value. The final few modes appear to have not yet converged and therefore are not expected to display this trend which was observed among the converged modes.
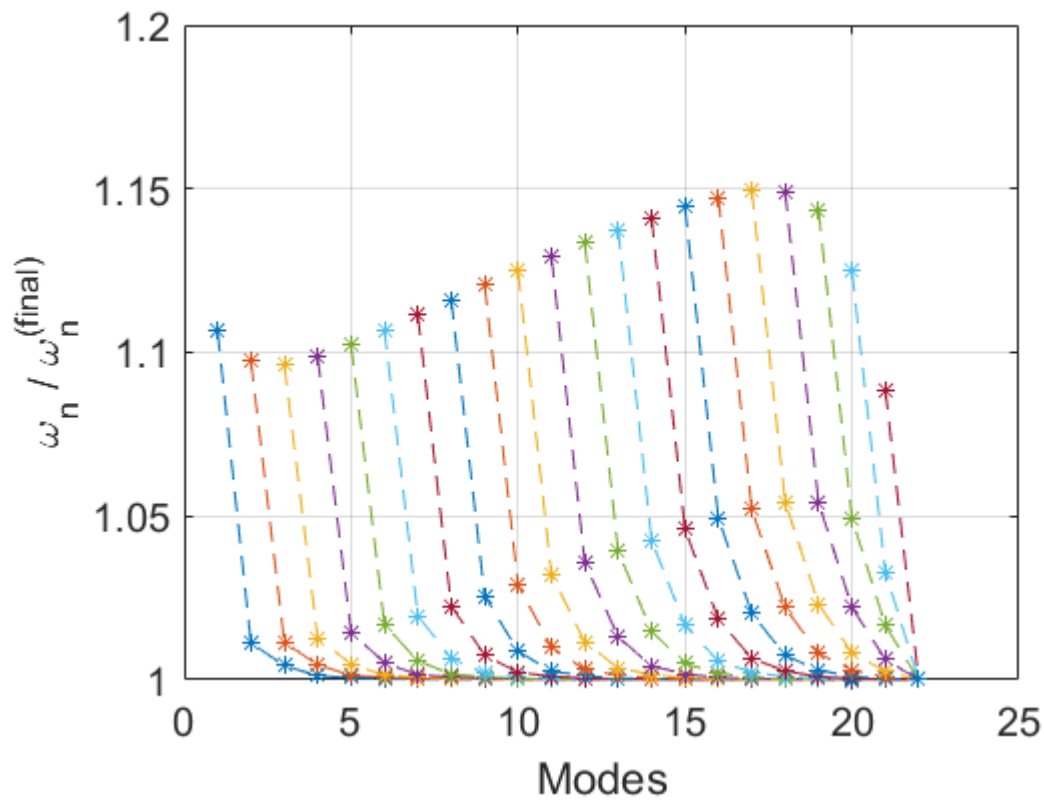


Figure 4.23. Natural Frequencies of the non-uniform film described in Table 4.13, divided by their final value with 22 modes, as a function of the number of modes included.

The first three natural frequencies of the film described in Table 4.13 are computed with 22 modes and compared to values obtained from [107] in Table 4.14. The appropriate natural frequencies in reference [107] are those for a clamped-clamped

truncated wedge, and for the film described in Table 4.13 the truncation factor is $\alpha = 0.5$. This describes a linearly tapered film in which the thickness of the film at one end is one-half the thickness at the other end.

Table 4.14. Natural Frequencies of the Non-Uniform (tapered) Film of Table 4.13.

| Mode | Naguleswaran [107] (rad/s) | Calculated (rad/s) | Error (%) |
|---|---|---|---|
| Mode 1 | 1.11697e6 | 1.11692e6 | .004 |
| Mode 2 | 3.07562e6 | 3.07547e6 | .005 |
| Mode 3 | 6.02663e6 | 6.02628e6 | .006 |

The mode shapes of the non-uniform film are the eigenvectors of the system of equations described by Equation 4.47. The calculated first three mode shapes of the non-uniform film are shown in Figure 4.24 and are compared to the mode shapes of the uniform film. It is seen that the peaks of the mode shapes shift to the left, where the film is thinner and where greater deflection may be expected to occur.

### 4.5.6 Comparison with 3D Model Results

Simulations of the PIV are run for each of the profiles in the 1D model. Table 4.15 and Table 4.16 present the changes in the PIV for both the 3D and 1D models.

Considering each profile separately, when the nonuniformity is adjusted by 10% of the film thickness, the difference in the PIV between the 3D and 1D simulations is generally less than one volt and varies by no more than 2.5 volts, or about 3% of the nominal value. The estimated natural frequencies are even closer, differing by no more than 1 kHz, or about 1% of the nominal value.
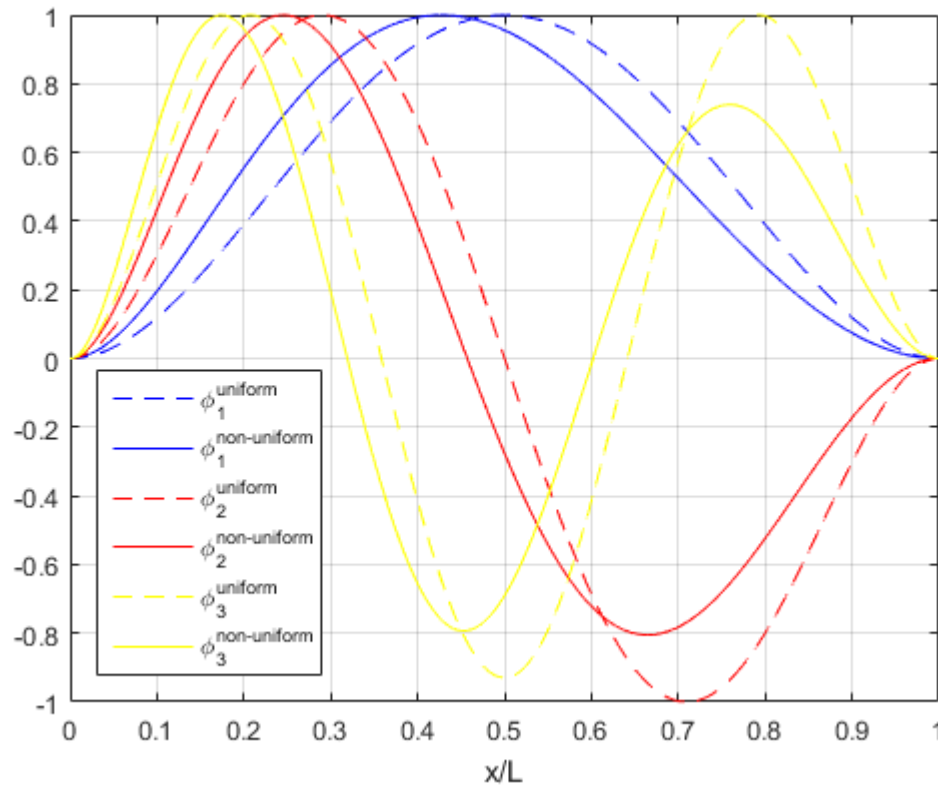
Figure 4.24. Comparison of the first three mode shapes of the uniform film to the first three mode shapes of the non-uniform film described in Table 4.13.

## 4.6 Conclusions

Three-dimensional electro-structural simulations of RF-MEMS device performance were carried out by means of the finite element method in order to investigate the effects of non-uniform film thicknesses on the pull-in voltage and the natural frequency of fixed-fixed capacitive radio-frequency microelectromechanical systems (RF-MEMS) used as radio-frequency switches. The switch under investigation consists of a long thin film suspended over an electrode, which in turn is covered by a dielectric. The film is treated as fixed at its ends and free along its long edges. These simulations estimated the pull-in voltage and the natural frequency, key device characteristics, as the non-uniformity of the thin film thickness was systematically varied by adjusting

Table 4.15. Sensitivity of the PIV and first natural frequency to the Cosine coefficients $C_{jk}$ and Sine coefficients $S_{jk}$ as applied to the top surface of the film, as a difference from the nominal value. The simulation voltage step size is 0.1V for the 3D model and less than 0.1V for the 1D model. The nominal device resolves a PIV of 96.1V and a natural frequency of 95.2 kHz in the 3D model. Yellow and blue represent +0.3 and -0.3 microns thickness, respectively.

| Profile | $PIV_{3D}(V)$ | $PIV_{1D}(V)$ | $\omega_{n1,3D}(kHz)$ | $\omega_{n1,1D}(kHz)$ | Profile |
|---|---|---|---|---|---|
| $C_{10}^{top} = 0.30\mu m$ | 102.8 | 103.8 | 101.9 | 101.7 | |
| $C_{20}^{top} = 0.30\mu m$ | 103.2 | 101.7 | 101.7 | 102.7 | |
| $C_{30}^{top} = 0.30\mu m$ | 97.9 | 98.4 | 96.8 | 97.4 | |
| $C_{40}^{top} = 0.30\mu m$ | 96.8 | 96.7 | 95.5 | 96.0 | |
| $C_{10}^{top} = -0.30\mu m$ | 90.4 | 89.6 | 90.4 | 90.2 | |
| $C_{20}^{top} = -0.30\mu m$ | 88.2 | 89.8 | 87.9 | 87.7 | |
| $C_{30}^{top} = -0.30\mu m$ | 92.0 | 91.8 | 91.4 | 91.4 | |
| $C_{40}^{top} = -0.30\mu m$ | 93.2 | 93.1 | 92.6 | 92.6 | |
| $S_{10}^{top} = 0.30\mu m$ | 95.8 | 96.1 | 94.9 | 95.3 | |
| $S_{20}^{top} = 0.30\mu m$ | 96.1 | 96.1 | 95.2 | 95.7 | |
| $S_{30}^{top} = 0.30\mu m$ | 95.4 | 95.6 | 94.5 | 94.9 | |
| $S_{40}^{top} = 0.30\mu m$ | 95.3 | 95.2 | 94.4 | 94.5 | |

the top and bottom surfaces of the suspended electrode according to two-dimensional Fourier functions.

One-dimensional simulations of the same devices, considering only nonuniformity along the length of the devices and subject to the assumptions of Euler-Bernoulli beam theory, were then performed. The results of these one-dimensional simulations were then compared to those of the three-dimensional simulations and were seen to be in reasonable agreement.

Table 4.16. Sensitivity of the PIV and first natural frequency to the Cosine coefficients $C_{jk}$ and Sine coefficients $S_{jk}$ as applied to the bottom surface of the film, as a difference from the nominal value. The simulation voltage step size is 0.1V for the 3D model and less than 0.1V for the 1D model. The nominal device resolves a PIV of 96.1V and a natural frequency of 95.2 kHz in the 3D model. Yellow and blue represent +0.3 and -0.3 microns thickness, respectively.

| Profile | $PIV_{3D}(V)$ | $PIV_{1D}(V)$ | $\omega_{n1,3D}(kHz)$ | $\omega_{n1,1D}(kHz)$ | Profile |
|---------|---------------|---------------|------------------------|------------------------|---------|
| $C_{10}^{bot} = 0.30\mu m$ | 87.1 | 89.6 | 90.4 | 90.2 |  |
| $C_{20}^{bot} = 0.30\mu m$ | 91.2 | 89.8 | 87.9 | 87.7 |  |
| $C_{30}^{bot} = 0.30\mu m$ | 90.6 | 91.8 | 91.4 | 91.4 |  |
| $C_{40}^{bot} = 0.30\mu m$ | 92.1 | 93.1 | 92.6 | 92.6 |  |
| $C_{10}^{bot} = -0.30\mu m$ | 105.1 | 103.8 | 101.8 | 101.7 |  |
| $C_{20}^{bot} = -0.30\mu m$ | 97.4 | 101.7 | 101.7 | 102.7 |  |
| $C_{30}^{bot} = -0.30\mu m$ | 96.6 | 98.4 | 96.8 | 97.4 |  |
| $C_{40}^{bot} = -0.30\mu m$ | 94.8 | 96.7 | 95.5 | 96.0 |  |
| $S_{10}^{bot} = 0.30\mu m$ | 94.7 | 96.1 | 94.9 | 95.3 |  |
| $S_{20}^{bot} = 0.30\mu m$ | 94.2 | 96.1 | 95.2 | 95.7 |  |
| $S_{30}^{bot} = 0.30\mu m$ | 93.9 | 95.6 | 94.5 | 94.9 |  |
| $S_{40}^{bot} = 0.30\mu m$ | 93.6 | 95.2 | 94.4 | 94.5 |  |

Polynomial response surfaces of the PIV and natural frequency of these devices as functions of the 40 chosen Fourier coefficients were generated from the 3D simulations. The final response surfaces, generated from 961 3D FEM simulations, were tested on 1300 separate 3D FEM simulations and performed well, with RMSE of 0.38 volts and 387 hertz for the PIV and the natural frequency respectively, which is less than 0.5% of the nominal value of each. The generation of well-fitted response surfaces required a larger number of 3D simulations than was initially expected. Despite a small mean error, some natural frequencies were grossly overtimated by that response

surface, especially as the 3D simulation natural frequency increased above its nominal value. These response surfaces were applied to propagate uncertainty from assumed distributions of the profile coefficients into estimates of the PIV and natural frequency.

The cosine and sine profiles on the top and bottom surfaces were seen to have unique impacts on the PIV and natural frequency. Sine profiles are seen to have much less impact on either surface. Varying the profile on the bottom surface of the film using cosine profiles generally shifted the estimated PIV and natural frequency down, with a few exceptions. Among the tested profiles, the deviation of the PIV from the value found for the nominally flat device was greatest among those profiles which were thickest and thinnest near the fixed ends of the film. Variation of the film thickness across its width was seen to have a smaller impact on the PIV.

It is concluded that attention to the thickness uniformity and to device orientation in fabrication will permit the reduction of observed variability in device-to-device PIV, resulting in increased reliability in fabricated switches.

# 5. SUMMARY

The first chapter of this work introduced thin films and their application in RF-MEMS. In the second chapter, simulations of the response of an electrostatically-actuated RF-MEMS switch nickel membrane with fixed-fixed and torsion-spring boundary conditions and undergoing plastic deformation due to Coble creep were presented. This required the introduction of a Coble creep formulation incorporated into an existing Euler-Bernoulli beam model. The model was calibrated against published experimental PIVs before creep was simulated. Uncertainty in the device geometry and material properties was propagated through the simulations to the output quantities of interest, and it was shown that the range of uncertainty in the input parameters yielded uncertainty in the quantities of interest which increased over time due to creep. A torsion-spring boundary condition was considered as a possible improvement in the model, but because the residual stresses were unknown, it was not possible to calibrate a reliable value of the torsion spring stiffness despite the wealth of PIV measurements and voltage-gap curves; the large uncertainty in the residual stresses covered up any effect of the effective torsion spring boundary condition. Finally, a distinct decrease in device lifetime is noted with increasing voltage.

In the third chapter, the influence of grain size distributions in a thin film undergoing Coble creep was demonstrated using a finite-volume model. The inclusion of multiple layers with grain sizes representative of those seen in experiments, as opposed to a model in which the grain size is treated as uniform at the mean experimental value, was seen to increase the simulated creep rate. The inclusion of uncertainty in the grain size distribution resulted in distributions of the PIV which show increasing variability with time and with greater loads. An asymmetric stress profile developed in the multi-layer films, with the smallest grains experiencing greater plastic strain and possibly contributing to the creep recovery phenomenon.

In the final chapter, three-dimensional electro-structural finite element simulations were performed to investigate the effects of non-uniform film thicknesses on the PIV and natural frequencies of fixed-fixed switches as the non-uniformity of the thin film thickness was systematically varied. Among the tested profiles, the deviation of the PIV from its nominal value was greater among the those profiles which varied along the length alone. Variation of the film thickness across its width was seen to have a smaller impact on the PIV. Furthermore, cosine profiles had a greater impact than the sine profiles, and varying the profile on the bottom surface of the film using cosine profiles generally shifted the estimated PIV down. Finally, assumed uncertainty in the profiles was propagated to the PIV and natural frequency, resulting in an estimate of the uncertainty in these quantities of interest.

# 6. FUTURE WORK

In this chapter, limitations of the current work and suggestions for future work are presented.

Chapter 2 presents the incorporation of creep into a 1D Euler-Bernoulli beam model and the propagation of uncertainty from material and geometric parameters of a RF-MEMS switch to four chosen output quantities of interest, including the PIV. Missing among these quantities of interest are several key device parameters, including the closing time and the natural frequency of the suspended electrode. Furthermore, noting that uncertainty was only propagated forward, a tool to predict required manufacturing specifications in order to achieve a given device lifetime may prove useful. Because creep is one of several reliability issues which cause device failure, such a tool would be most useful if it were to include other failure mechanisms, such as dielectric charging.

Chapter 3 considers the effects of the microstructural characteristics of the suspended electrodes, generating representative distributions of grain sizes and presenting estimations of the resulting PIVs as a function of time. Although stress distributions in the loaded film as creep is occurring are shown, behavior after unloading of the film is not considered. This unloading may provide some insight into observed recovery from creep, as seen in, e.g., references [85] and [55].

Chapter 4 addresses the possibility of film thickness non-uniformity in the suspended electrode of the RF-MEMS switch. The natural frequency of the suspended film is introduced as a quantity of interest in addition to the PIV, but here the remaining QOI previously discussed, e.g. the dynamic PIV and impact velocity, are neglected and may deserve further treatment. Again, only forward propagation of uncertainty is considered, where the reverse problem of determining required tolerances to meet desired specifications may prove more useful. Further, if the importance of

the profile non-uniformity is to be determined, the resulting uncertainty in the PIV and natural frequency would be best compared to similar effects from other uncertain parameters, e.g. device-to-device variations in thickness as well as initial curvature.

Preliminary work into the residual stress distribution is not presented here but remains a topic of interest. In general, residual stresses in MEMS alter the shape of the devices and effectively increase their stiffness, resulting in larger applied loads and larger stresses if a certain deformation is required. These larger stresses will be concentrated in areas of greater residual stress if gradients of residual stress exist within a device – and with the wide distributions of residual stress seen from device to device, it appears reasonable to make the assumption that residual stresses will vary within a device. It would be useful in design to distinguish the effects of residual stress, initial curvature, and relaxed (e.g. torsion spring) boundary conditions, and to present a method for the determination of each of these parameters in manufactured devices.

REFERENCES

# REFERENCES

[1] Lei Cao and Marisol Koslowski. Effect of microstructural uncertainty on the yield stress of nanocrystalline nickel. *Acta Materialia*, 61(4):1413–1420, 2013.

[2] AH Chokshi, A Rosen, J Karch, and H Gleiter. On the validity of the hall-petch relationship in nanocrystalline materials. *Scripta Metallurgica*, 23(10):1679–1683, 1989.

[3] VY Gertsman, M Hoffmann, H Gleiter, and R Birringer. The study of grain size dependence of yield stress of copper for a wide grain size range. *Acta metallurgica et materialia*, 42(10):3539–3544, 1994.

[4] Ning Wang, Zhirui Wang, KT Aust, and U Erb. Room temperature creep behavior of nanocrystalline nickel produced by an electrodeposition technique. *Materials Science and Engineering: A*, 237(2):150–158, 1997.

[5] Jakob Schiøtz, Francesco D Di Tolla, and Karsten W Jacobsen. Softening of nanocrystalline metals at very small grain sizes. *Nature*, 391(6667):561–563, 1998.

[6] MA Haque and MT A Saif. Mechanical behavior of 30–50 nm thick aluminum films under uniaxial tension. *Scripta Materialia*, 47(12):863–867, 2002.

[7] YM Wang, RT Ott, T Van Buuren, TM Willey, MM Biener, and AV Hamza. Controlling factors in tensile deformation of nanocrystalline cobalt and nickel. *Physical Review B*, 85(1):014101, 2012.

[8] Harold J Frost and Michael F Ashby. Deformation mechanism maps: the plasticity and creep of metals and ceramics. 1982.

[9] Hao-Han Hsu, Marisol Koslowski, and Dimitrios Peroulis. An experimental and theoretical investigation of creep in ultrafine crystalline nickel rf-mems devices. *Microwave Theory and Techniques, IEEE Transactions on*, 59(10):2655–2664, 2011.

[10] Aurelio Somà, Muhammad Mubasher Saleem, and Giorgio De Pasquale. Effect of creep in rf mems static and dynamic behavior. *Microsystem Technologies*, 22(5):1067–1078, 2016.

[11] DA Hardwick. The mechanical properties of thin films: a review. *Thin Solid Films*, 154(1):109–124, 1987.

[12] Akshdeep Sharma, Maninder Kaur, Deepak Bansal, Dinesh Kumar, and Kamaljit Rangra. Review of mems test structures for mechanical parameter extraction. *Journal of Nano- and Electronic Physsics*, 3:243–253, 2011.

[13] Ioannis Chasiotis and Wolfgang G Knauss. Mechanical properties of thin polysilicon films by means of probe microscopy. In *Micromachining and Microfabrication*, pages 66–75. International Society for Optics and Photonics, 1998.

[14] R Spolenak, WL Brown, N Tamura, AA MacDowell, RS Celestre, HA Padmore, B Valek, JC Bravman, T Marieb, H Fujimoto, et al. Local plasticity of al thin films as revealed by x-ray microdiffraction. *Physical review letters*, 90(9):096102, 2003.

[15] Xiaoding Wei and Jeffrey W Kysar. Residual plastic strain recovery driven by grain boundary diffusion in nanocrystalline thin films. *Acta Materialia*, 59(10):3937–3945, 2011.

[16] X Yan, WL Brown, Y Li, John Papapolymerou, C Palego, J Hwang, and RP Vinci. Anelastic stress relaxation in gold films and its impact on restoring forces in mems devices. *Microelectromechanical Systems, Journal of*, 18(3):570–576, 2009.

[17] WM Yin, SH Whang, R Mirshams, and CH Xiao. Creep behavior of nanocrystalline nickel at 290 and 373 k. *Materials Science and Engineering: A*, 301(1):18–22, 2001.

[18] F Dalla Torre, H Van Swygenhoven, and M Victoria. Nanocrystalline electrodeposited ni: microstructure and tensile properties. *Acta Materialia*, 50(15):3957–3970, 2002.

[19] MJNV Prasad, S Suwas, and AH Chokshi. Microstructural evolution and mechanical characteristics in nanocrystalline nickel with a bimodal grain-size distribution. *Materials Science and Engineering: A*, 503(1):86–91, 2009.

[20] Somnath Ghosh and Dennis M Dimiduk. *Computational methods for microstructure-property relationships*. Springer, 2011.

[21] RA Masumura, PM Hazzledine, and CS Pande. Yield stress of fine grained materials. *Acta Materialia*, 46(13):4527–4534, 1998.

[22] B Zhu, RJ Asaro, P Krysl, and R Bailey. Transition of deformation mechanisms and its connection to grain size distribution in nanocrystalline metals. *Acta materialia*, 53(18):4825–4838, 2005.

[23] B Zhu, RJ Asaro, P Krysl, K Zhang, and JR Weertman. Effects of grain size distribution on the mechanical response of nanocrystalline metals: Part ii. *Acta materialia*, 54(12):3307–3320, 2006.

[24] MP Phaniraj, MJNV Prasad, and Atul Harish Chokshi. Grain-size distribution effects in plastic flow and failure. *Materials Science and Engineering: A*, 463(1):231–237, 2007.

[25] Marisol Koslowski. Effect of grain size distribution on plastic strain recovery. *Physical Review B*, 82(5):054110, 2010.

[26] Xu Weichang and Dai Pinqiang. Tensile deformation microstructures and deformation behaviours in electrodeposited nanocrystalline ni with broad grain size distribution. *Rare Metal Materials and Engineering*, 39(6):953–957, 2010.

[27] Yingguang Liu, Jianqiu Zhou, and Xiang Ling. Impact of grain size distribution on the multiscale mechanical behavior of nanocrystalline materials. *Materials Science and Engineering: A*, 527(7):1719–1729, 2010.

[28] Jagannathan Rajagopalan, Jong H Han, and M Taher A Saif. Plastic deformation recovery in freestanding nanocrystalline aluminum and gold thin films. *Science*, 315(5820):1831–1834, 2007.

[29] Yujie Wei, Allan F Bower, and Huajian Gao. Recoverable creep deformation and transient local stress concentration due to heterogeneous grain-boundary diffusion and sliding in polycrystalline solids. *Journal of the Mechanics and Physics of Solids*, 56(4):1460–1483, 2008.

[30] Xiaoyan Li, Yujie Wei, Wei Yang, and Huajian Gao. Competing grain-boundary-and dislocation-mediated mechanisms in plastic strain recovery in nanocrystalline aluminum. *Proceedings of the National Academy of Sciences*, 106(38):16108–16113, 2009.

[31] Peter Smereka, Xingquan Li, Giovanni Russo, and David J Srolovitz. Simulation of faceted film growth in three dimensions: microstructure, morphology and texture. *Acta Materialia*, 53(4):1191–1204, 2005.

[32] JM Thijssen. Simulations of polycrystalline growth in 2+ 1 dimensions. *Physical Review B*, 51(3):1985, 1995.

[33] JM Thijssen, HJF Knops, and AJ Dammers. Dynamic scaling in polycrystalline growth. *Physical Review B*, 45(15):8650, 1992.

[34] Colin Ophus, Erik J Luber, and David Mitlin. Analytic description of competitive grain growth. *Physical Review E*, 81(1):011601, 2010.

[35] Gabriel M Rebeiz. *RF MEMS: theory, design, and technology.* John Wiley & Sons, 2004.

[36] Gabriel M Rebeiz and Jeremy B Muldavin. Rf mems switches and switch circuits. *IEEE Microwave magazine*, 2(4):59–71, 2001.

[37] Stepan Lucyszyn. *Advanced RF Mems.* Cambridge University Press, 2010.

[38] Yunhan Huang, Arvind Sai Sarathi Vasan, Ravi Doraiswami, Michael Osterman, and Michael Pecht. Mems reliability review. *IEEE Transactions on Device and Materials Reliability*, 12(2):482–493, 2012.

[39] Allyson L Hartzell, Mark G Da Silva, and Herbert Shea. *MEMS reliability.* Springer Science & Business Media, 2010.

[40] Danelle M Tanner. Mems reliability: Where are we now? *Microelectronics Reliability*, 49(9):937–940, 2009.

[41] Daniel J Fonseca and Miguel Sequera. On mems reliability and failure mechanisms. *International Journal of Quality, Statistics, and Reliability*, 2011, 2011.

[42] Wilhelmus de Groot, Daniel Felnhofer, and Evgeni Gusev. Reliability aspects of capacitive mems devices. *Procedia Engineering*, 25:180–186, 2011.

[43] Jin Woo Lee, Ajit K Mahapatro, Dimitrios Peroulis, and Arvind Raman. Vibration-based monitoring and diagnosis of dielectric charging in rf-mems switches. *Microelectromechanical Systems, Journal of*, 19(6):1490–1502, 2010.

[44] WM Van Spengen. Capacitive rf mems switch dielectric charging and reliability: a critical review with recommendations. *Journal of Micromechanics and Microengineering*, 22(7):074001, 2012.

[45] George Papaioannou, Fabio Coccetti, and Robert Plana. On the modeling of dielectric charging in rf-mems capacitive switches. In *Silicon Monolithic Integrated Circuits in RF Systems (SiRF), 2010 Topical Meeting on*, pages 108–111. IEEE, 2010.

[46] Shankhadeep Das, Sanjay R Mathur, and Jayathi Y Murthy. Finite-volume method for creep analysis of thin rf mems devices using the theory of plates. *Numerical Heat Transfer, Part B: Fundamentals*, 61(2):71–90, 2012.

[47] Ankit Jain, Sambit Palit, and Muhammad Ashraful Alam. A physics-based predictive modeling framework for dielectric charging and creep in rf mems capacitive switches and varactors. *Microelectromechanical Systems, Journal of*, 21(2):420–430, 2012.

[48] Shankhadeep Das, Marisol Koslowski, Sanjay R Mathur, and Jayathi Y Murthy. Finite volume method for simulation of creep in rf mems devices. In *ASME 2011 International Mechanical Engineering Congress and Exposition*, pages 119–128. American Society of Mechanical Engineers, 2011.

[49] Hao-Han Hsu and Dimitrios Peroulis. A cad model for creep behavior of rf-mems varactors and circuits. *Microwave Theory and Techniques, IEEE Transactions on*, 59(7):1761–1768, 2011.

[50] Derek Hull and David J Bacon. *Introduction to dislocations*, volume 37. Elsevier, 2011.

[51] Thomas H Courtney. *Mechanical behavior of materials*. Waveland Press, 2005.

[52] V Yamakov, D Wolf, SR Phillpot, and H Gleiter. Grain-boundary diffusion creep in nanocrystalline palladium by molecular-dynamics simulation. *Acta Materialia*, 50(1):61–73, 2002.

[53] CL Wang, YH Lai, JC Huang, and TG Nieh. Creep of nanocrystalline nickel: A direct comparison between uniaxial and nanoindentation creep. *Scripta Materialia*, 62(4):175–178, 2010.

[54] ZH Cao, L Wang, K Hu, YL Huang, and XK Meng. Microstructural evolution and its influence on creep and stress relaxation in nanocrystalline ni. *Acta Materialia*, 60(19):6742–6754, 2012.

[55] Deborah J Vickers-Kirby, Randall L Kubena, Frederic P Stratton, Richard J Joyce, David T Chang, and Jinsoo Kim. Anelastic creep phenomena in thin metal plated cantilevers for mems. In *MRS proceedings*, volume 657, pages EE2–5. Cambridge Univ Press, 2000.

[56] K Tuck, A Jungen, A Geisberger, M Ellis, and G Skidmore. A study of creep in polysilicon mems devices. *Journal of engineering materials and technology*, 127(1):90–96, 2005.

[57] Peter M Osterberg and Stephen D Senturia. M-test: a test chip for mems material property measurement using electrostatically actuated test structures. *Journal of Microelectromechanical systems*, 6(2):107–118, 1997.

[58] Xiaohui Guo, Jia Li, Dongbin Xiu, and Alina Alexeenko. Uncertainty quantification models for micro-scale squeeze-film damping. *International Journal for Numerical Methods in Engineering*, 84(10):1257–1272, 2010.

[59] Marisol Koslowski and Alejandro Strachan. Uncertainty propagation in a multiscale model of nanocrystalline plasticity. *Reliability Engineering & System Safety*, 96(9):1161–1170, 2011.

[60] Ayyaswamy Venkattraman and Alina Alexeenko. Simulations of impulsive dynamics in rf mems capacitive switches. In *ASME 2011 International Mechanical Engineering Congress and Exposition*, pages 153–158. American Society of Mechanical Engineers, 2011.

[61] Juan Zeng, Andrew Kovacs, Anurag Garg, Anil K Bajaj, and Dimitrios Peroulis. Residual stress extraction of surface-micromachined fixed-fixed nickel beams using a wafer-scale technique. *Journal of Microelectromechanical Systems*, 24(6):1803–1816, 2015.

[62] Juan Zeng, Anurag Garg, Andrew Kovacs, Anil K Bajaj, and Dimitrios Peroulis. An equation-based nonlinear model for non-flat mems fixed–fixed beams with non-vertical anchoring supports. *Journal of Micromechanics and Microengineering*, 25(5):055018, 2015.

[63] Michael G Snow. *Comprehensive modeling of electrostatically actuated MEMS beams including uncertainty quantification*. PhD thesis, Purdue University, 2010.

[64] Francois M Hemez. Uncertainty quantification and the verification and validation of computational models. *Damage Prognosis for Aerospace, Civil and Mechanical Systems*, pages 201–220, 2005.

[65] Dani Gamerman and Hedibert F Lopes. *Markov chain Monte Carlo: stochastic simulation for Bayesian inference*. CRC Press, 2006.

[66] Jon C Helton and Freddie Joe Davis. Latin hypercube sampling and the propagation of uncertainty in analyses of complex systems. *Reliability Engineering & System Safety*, 81(1):23–69, 2003.

[67] Antonio G Garcia. Orthogonal sampling formulas: a unified approach. *SIAM review*, 42(3):499–512, 2000.

[68] Dongbin Xiu and George Em Karniadakis. Modeling uncertainty in steady state diffusion problems via generalized polynomial chaos. *Computer methods in applied mechanics and engineering*, 191(43):4927–4948, 2002.

[69] S Oladyshkin and W Nowak. Data-driven uncertainty quantification using the arbitrary polynomial chaos expansion. *Reliability Engineering & System Safety*, 106:179–190, 2012.

[70] Mohammad Younis, Eihab M Abdel-Rahman, Ali Nayfeh, et al. A reduced-order model for electrically actuated microbeam-based mems. *Microelectromechanical Systems, Journal of*, 12(5):672–680, 2003.

[71] Xiaohui Guo and Alina Alexeenko. Compact model of squeeze-film damping based on rarefied flow simulations. *Journal of Micromechanics and Microengineering*, 19(4):045026, 2009.

[72] SG Jennings. The mean free path in air. *Journal of Aerosol Science*, 19(2):159–166, 1988.

[73] Romesh C Batra, Maurizio Porfiri, and Davide Spinello. Electromechanical model of electrically actuated narrow microbeams. *Microelectromechanical Systems, Journal of*, 15(5):1175–1189, 2006.

[74] S. Mahadevan, Y. Ling, J. Mullins, and S. Sankararaman. Integration of multi-scale, multi-physics models, data, and uq activities. pages 108–111. Purdue University, PRISM EAB and Mid-Year Review, 2012.

[75] Ansel C Ugural and Saul K Fenster. *Advanced strength and applied elasticity.* Pearson education, 2003.

[76] Lawrence F Shampine and Mark W Reichelt. The matlab ode suite. *SIAM journal on scientific computing*, 18(1):1–22, 1997.

[77] Patrick R Cantwell, Hojin Kim, Matthew M Schneider, Hao-Han Hsu, Dimitrios Peroulis, Eric A Stach, and Alejandro Strachan. Estimating the in-plane young's modulus of polycrystalline films in mems. *Microelectromechanical Systems, Journal of*, 21(4):840–849, 2012.

[78] Martin Hunt, Benjamin Haley, Michael McLennan, Marisol Koslowski, Jayathi Murthy, and Alejandro Strachan. Puq: A code for non-intrusive uncertainty propagation in computer simulations. *Computer Physics Communications*, 194:97–107, 2015.

[79] RP Vedula, Sambit Palit, Muhammad A Alam, and Alejandro Strachan. Role of atomic variability in dielectric charging: A first-principles-based multiscale modeling study. *Physical Review B*, 88(20):205204, 2013.

[80] HS Cho, KJ Hemker, Kun Lian, J Goettert, and G Dirras. Measured mechanical properties of liga ni structures. *Sensors and Actuators A: Physical*, 103(1):59–63, 2003.

[81] RL Coble. A model for boundary diffusion controlled creep in polycrystalline materials. *Journal of Applied Physics (US)*, 34, 1963.

[82] JH Schneibel, RL Coble, and RM Cannon. The role of grain size distributions in diffusional creep. *Acta Metallurgica*, 29(7):1285–1290, 1981.

[83] PM Hazzledine and JH Schneibel. Theory of coble creep for irregular grain structures. *Acta metallurgica et materialia*, 41(4):1253–1262, 1993.

[84] WS Tong, JM Rickman, HM Chan, and MP Harmer. Coble-creep response and variability of grain-boundary properties. *Journal of materials research*, 17(02):348–352, 2002.

[85] LIJC Bergers, JPM Hoefnagels, and MGD Geers. Characterization of time-dependent anelastic microbeam bending mechanics. *Journal of Physics D: Applied Physics*, 47(35):355306, 2014.

[86] Hao-Han Hsu and Dimitrios Peroulis. An experimental investigation on viscoelastic behavior in tunable planar rf-mems resonators. In *Microwave Symposium Digest (MTT), 2010 IEEE MTT-S International*, pages 1150–1153. IEEE, 2010.

[87] J Bai and R Raj. Influence of grain size variability on the strain rate dependence of the stress exponent in mixed-mode power law and diffusional creep. *Metallurgical and Materials Transactions A*, 36(11):2913–2919, 2005.

[88] Jie Bai and Rishi Raj. Inverse problems in stochastic modeling of mixed-mode power-law and diffusional creep for distributed grain size. *Metallurgical and Materials Transactions A*, 41(2):308–317, 2010.

[89] Marc A Meyers, A Mishra, and David J Benson. Mechanical properties of nanocrystalline materials. *Progress in materials science*, 51(4):427–556, 2006.

[90] Shankhadeep Das, Sanjay R Mathur, and Jayathi Y Murthy. An unstructured finite-volume method for structure–electrostatics interactions in mems. *Numerical Heat Transfer, Part B: Fundamentals*, 60(6):425–451, 2011.

[91] B-N Kim, K Hiraga, K Morita, and I-W Chen. Rate of creep due to grain-boundary diffusion in polycrystalline solids with grain-size distribution. *Philosophical Magazine*, 85(20):2281–2292, 2005.

[92] Viviana Mulloni, Giuseppe Resta, Flavio Giacomozzi, and Benno Margesin. Influence of fabrication tolerances on the reliability of rf-mems capacitive switches. In *2015 XVIII AISEM Annual Conference*, pages 1–4. IEEE, 2015.

[93] Anna Persano, Jacopo Iannacci, Pietro Siciliano, and Fabio Quaranta. Out-of-plane deformation and pull-in voltage of cantilevers with residual stress gradient: Experiment and modelling. *Microsystem Technologies*, 25(9):3581–3588, 2019.

[94] Ryan C Tung, Anurag Garg, Andrew Kovacs, Dimitrios Peroulis, and Arvind Raman. Estimating residual stress, curvature and boundary compliance of doubly clamped mems from their vibration response. *Journal of Micromechanics and Microengineering*, 23(4):045009, 2013.

[95] Suresh Babu Krishna Moorthy. *Thin film structures in energy applications*. Springer, 2015.

[96] Krishna Seshan and Dominic Schepis. *Handbook of thin film deposition*. William Andrew, 2018.

[97] Hoa Thanh Le, Io Mizushima, Yasser Nour, Peter Torben Tang, Arnold Knott, Ziwei Ouyang, Flemming Jensen, and Anpan Han. Fabrication of 3d air-core mems inductors for very-high-frequency power conversions. *Microsystems & Nanoengineering*, 4:17082, 2018.

[98] Yasmin Abdul Wahab, Anuar Fadzil, Norhayati Soin, Sharifah Fatmadiana, Zaira Zaman Chowdhury, Nor Aliya Hamizi, Omid Akbarzadeh Pivehzhani, Thennarasan Sabapathy, and Yarub Al-Douri. Uniformity improvement by integrated electrochemical-plating process for cmos logic technologies. *Journal of Manufacturing Processes*, 38:422–431, 2019.

[99] Yuxin Du, Dong Wu, Zhen Song, Miao Liu, Sujie Yang, and Zheyao Wang. 3-d integration of mems and cmos using electroless plated nickel through-mems-vias. *Journal of Microelectromechanical Systems*, 25(4):770–779, 2016.

[100] Quoc-Dinh Cao, Liang Fang, Jiu-Ming Lv, Xin-Ping Zhang, and Nguyen Thuy Dat. Effects of pulse reverse electroforming parameters on the thickness uniformity of electroformed copper foil. *Transactions of the IMF*, 96(2):108–112, 2018.

[101] Jun Tang, Hong Wang, Rui Liu, Shengping Mao, Xiaolin Zhao, and Guifu Ding. Study on non-uniformity of through-mask electroplated ni thin-film. In *2008 International Conference on Electronic Packaging Technology & High Density Packaging*, pages 1–4. IEEE, 2008.

[102] Nurul Huda Shaik. Private communication. 2015.

[103] Inc ANSYS. *Ansys Academic Research Mechanical, Release 19.2, Help System, Coupled-Field Analysis Guide*.

[104] Rahul Mukerjee and CF Jeff Wu. *A modern theory of factorial design*. Springer Science & Business Media, 2007.

[105] Robert D Blevins. *Formulas for Natural Frequency and Mode Shape*. Van Nostrand Reinhold Company, 2007.

[106] Singiresu S Rao. *Vibration of continuous systems*. John Wiley & Sons, 2007.

[107] S Naguleswaran. A direct solution for the transverse vibration of euler-bernoulli wedge and cone beams. *Journal of Sound and Vibration*, 172(3):289–304, 1994.

APPENDICES

## A. 3D FINITE ELEMENT MESH DESCRIPTION

The following figures describe the mesh used in the 3D finite element model of the RF-MEMS switch.

An illustration of the top surface of the film is shown in Figure A.1.
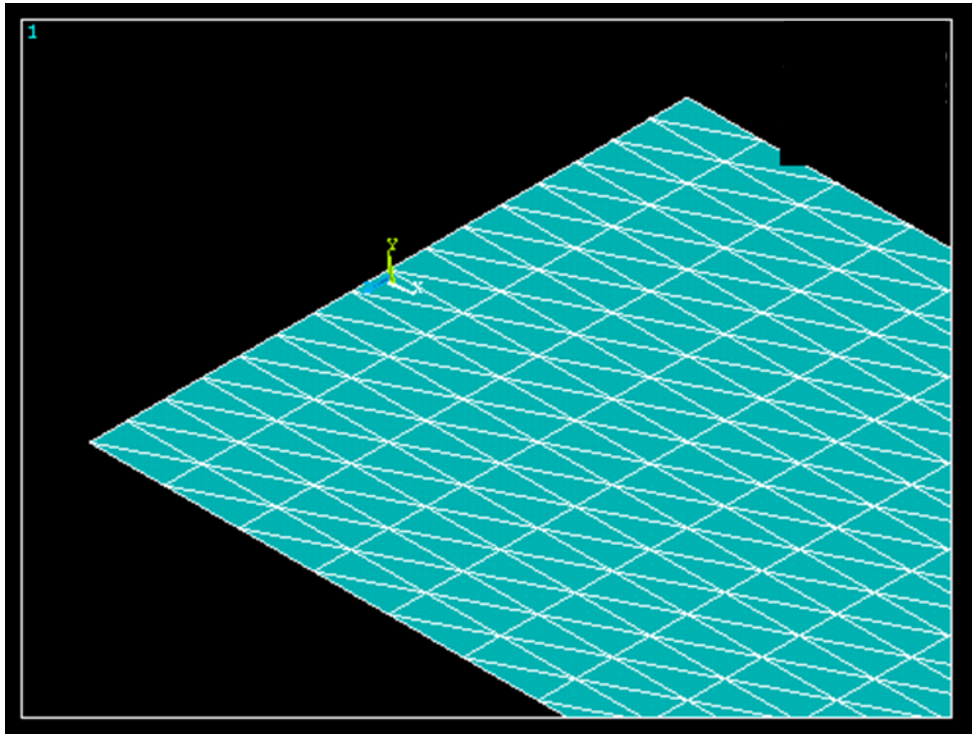


Figure A.1. Illustration of the subdivision of the top surface of the film before meshing.

The triangular subdivisions are evident. These triangles are extruded downward from the top surface, forming triangular prisms, which are used to represent the film and the air gap beneath it. Two of these extruded prisms are shown in FigureA.2.
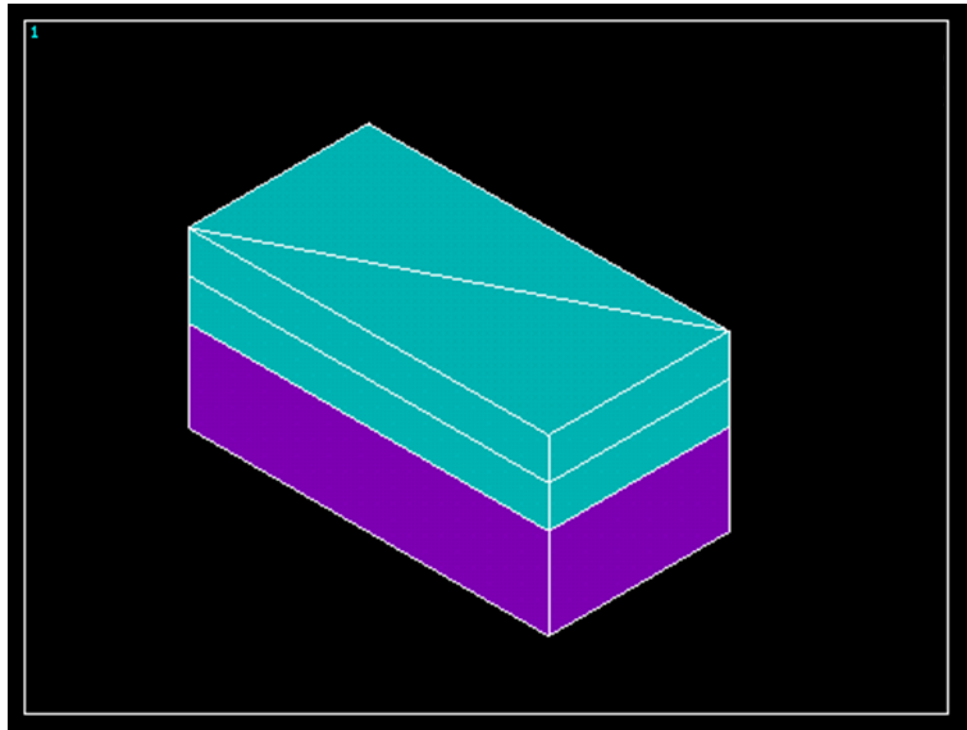


Figure A.2. A pair of vertically-oriented triangular prisms, as used to represent the film (top half) and air gap (bottom half), before meshing.

The bottom half of the volume shown is a portion of the air gap. The top half of the volume shown contains the top and bottom halves of the film. These prisms are then meshed. One representative mesh is shown in Figure A.3.
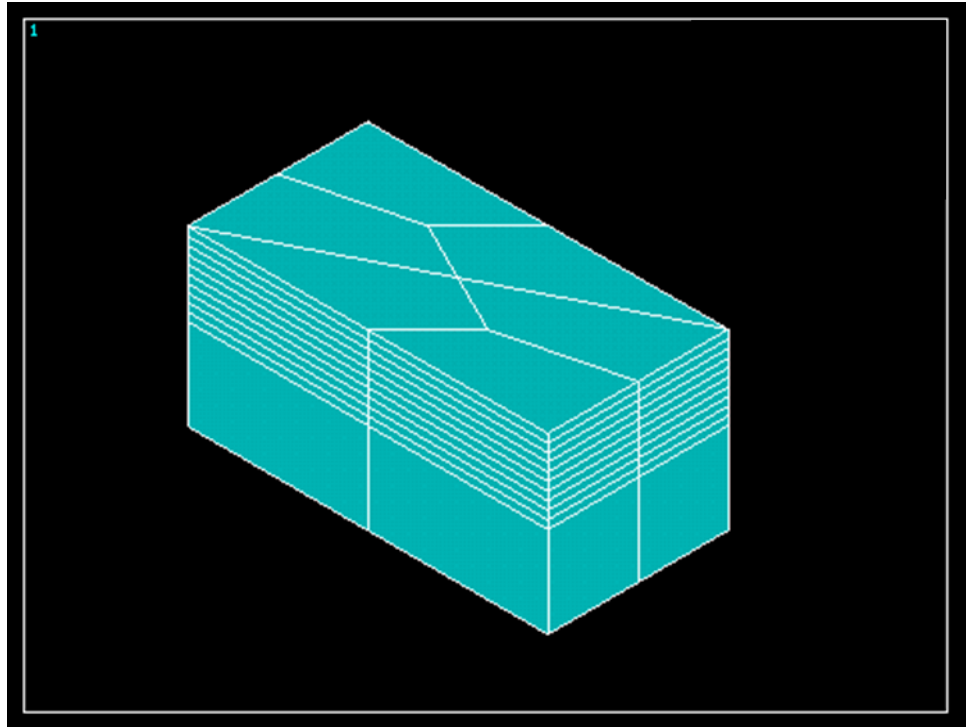


Figure A.3.  A pair of vertically-oriented triangular prisms, as used to represent the film (top half) and air gap (bottom half), after meshing.

Each triangular prism is seen to have been meshed as three vertically-oriented prisms. A single element is used through the thickness of the air gap, but the beam is meshed with eight elements through its thickness.